UNIVERSITÀ DEGLI STUDI DI GENOVA

Scuola di Scienze Matematiche, Fisiche e Naturali

PHD THESIS IN PHYSICS AND NANOSCIENCE
XXXIV CYCLE

Towards a DNA-based biosensor: a multi-technique study for sequence recognition

Supervisor:
Prof.ssa Ornella Cavalleri

Candidate:
Giulia Pinto

Contents

Introduction

Over the past two years, the COVID-19 pandemic has put the spotlight back on the search for new biological detection methods [1–3]. For SARS-CoV-2 detection, the current standard methods are Reverse Transcription-Polymerase Chain Reaction (RT-PCR) and serological tests [4]. Although these tests have helped monitor pandemic trends and are satisfactory, there are still issues related to time and cost. For example, PCR is highly sensitive and reliable, but its widespread use is limited due to the long time required to obtain test results (24-72 hours) and the need for qualified personnel and expensive laboratories, instruments, and consumables. The development of efficient, rapid, and inexpensive devices is of interest not only for the recent pandemic but for the specific detection of different disease-related biomarkers. The long-term goal of our research is the development of a biosensing platform capable of detecting nucleic acid sequences, like viral sequences as a SARS-CoV-2 gene region [5], and pathological analytes, like tumour over-expressed proteins [6]. Biosensors can be broadly divided in immunoassays, that require the presence of antibodies generated by the organism (which may be present both during and after infection), and DNA-based biosensors, that require the presence of the pathogens [7]. Therefore, depending on several factors, such as the stage of an infection and the availability of antibodies or viral/toxin-related DNA sequences, either immunoassays or DNA-based assays can be advantageously employed.

The aim of this thesis was the development and the analysis of the sensing performance of DNA-based biosensors, targeting the detection of disease-related oligonucleotide sequences. The next step will be to extend the approach to the detection of other pathogens through integration with the immuno-sensing scheme. The most novel aspect of our approach is the detection of the receptor/analyte interaction (i.e., the hybridization between probe DNA and target DNA strands) through a distinctive optical fingerprint exploiting in-situ and real-time spectroscopic ellipsometry measurements (Pinto et al. (2022), submitted). This broadband spectroscopic analysis is carried out through non-destructive and extremely rapid experiments, which do not require labelled strands, thick films or high DNA concentration. This novel approach allows also to detect hypochromism at the monolayer level, for the first time to our knowledge.

Concerning the fabrication, we optimized the preparation protocols of the sensing platform, for example by studying the effect of the buffer ionic strength (Pinto et al. (2019) [8], Pinto et al. (2020) [9]) and the incubation time of probe DNA. The best ex-

perimental parameters for detecting analytes were then investigated. To characterize the sensing performance analysis we focused on the re-usability, limit of detection, and specificity of the biosensor (Pinto et al. (2022), submitted). Our methodological approach combined optical (spectroscopic ellipsometry, surface plasmon enhanced ellipsometry) and photoelectron (X-rays photoelectron spectroscopy) spectroscopy and high sensitive mechanical (atomic force microscopy, quartz crystal microbalance) methods in order to give a complete characterization of the biological system.

The thesis consists of four chapters.
Chapter 1 starts with an overview of biosensors, analyzing the structure, the main application fields, and the classification. A brief introduction to self-assembled monolayers is provided, focusing in particular on thiolated films. DNA-based biosensors are presented, showing their main advantages. Finally, nucleic acids are introduced, discussing the main differences between DNA and RNA.
Chapter 2 presents the experimental methods employed for characterizing DNA films and analyzing the transduced signal: spectroscopic ellipsometry, surface plasmon enhanced ellipsometry, atomic force microscopy, X-rays photoelectron spectroscopy, quartz-crystal microbalance with dissipation.
Chapter 3 provides all the experimental protocols, describing the materials employed, the experimental set-up, and the technical data on the instruments.
Chapter 4 presents the results and the data analysis. Starting with the characterization of the optimized system, we then describe how it was optimized (through the analysis of the effect of various parameters involved), and we present the study on the performance of analyte detection. The characterization of the system was performed with a model DNA sequence (FZ24), while the sensor was tested with a synthetic RNA chain, whose sequence belongs to a gene region of SARS-CoV-2.
Finally, the conclusions summarize the results obtained and describe plans to improve the sensor and develop an immunological test on the same platform.

This thesis tests a biological system for the development of a sensitive, inexpensive, rapid and reusable nucleic acid detection sensor. The possible miniaturization of the platform makes this system very interesting for future applications, in particular to realize a device capable of recognizing different types of analytes on the same platform for the parallel screening of different diseases.

Chapter 1

Biosensing and Nucleic Acids

This chapter aims to introduce biosensors, which are a fundamental tool used in various fields. Biosensors often exploit the properties of self-assembled monolayers (SAMs) to obtain well oriented molecules anchored to a surface through covalent bonds (as in the case of thiolated SAMs on gold surfaces). Among all molecules, DNA and RNA-based biosensors are an excellent option to obtain SAMs with re-usability, specificity, and biocompatibility properties. Therefore, an in-depth discussion of DNA and RNA nucleic acids, such as general issues on nucleic acid SAMs, is presented.

1.1 Biosensors

Currently, in the field of biological detection, researchers have developed standardized methods to identify biomarkers such as nucleic acids and proteins. Two examples are the reverse transcriptase-polymerase chain reaction (RT-PCR) and the serological assays, both recently widely used during the COVID-19 pandemic. Nevertheless, the need to improve factors such as the detection sensitivity and the value for money appears to be more than enough reason to continue research on new methods.
A biosensor is an analytical device that selectively recognizes and quantifies one or more analytes among the compounds present in complex samples such as physiological fluids (blood, saliva, urine). The system incorporates a biological sensing element that detects biomolecules and through a transducer converts the physical or chemical signal into a measurable and countable signal. Biosensors are used not only for medical diagnostics [10–12] and monitoring [13], but also in food safety and quality monitoring [14], and environmental monitoring [15], due to their ability to sense a wide range of biomolecules, including proteins (antibodies, antigens), nucleic acids (DNA, RNA), micro-organisms (bacteria, pathogens) and also cells (tumour cells).

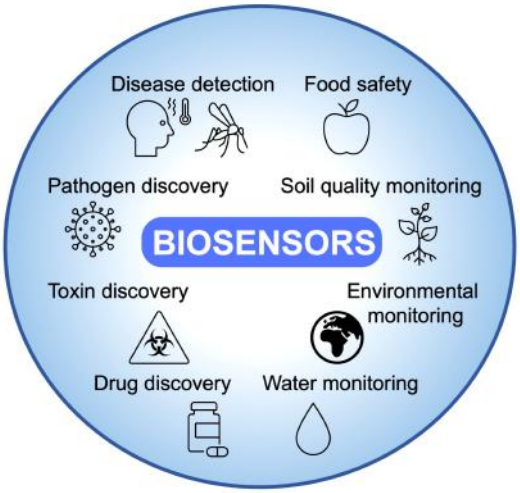

Figure 1.1 – *Main application fields of biosensors.*

According to the World Health Organization (WHO), within the Sexually Transmitted Diseases Diagnostics Initiative, an efficient diagnostic test of any kind must comply with the guidelines of ASSURED [16]: Affordable, Sensitive, Specific, User-friendly, Rapid and robust, Equipment-free, and Deliverable to end-users. Practically, biosensor development must address both manufacturing and evaluation of the sensing performance. Fabrication involves the choice of the substrate and of the receptor, and the functionalization of the substrate with the probe. The validation of the sensing performance is achievable by analyzing the signals generated by the chemical reaction between the receptor and the target analyte.

Biosensors consist of three main parts, as sketched in Figure 1.2:

1. receptors (sensing elements), that allow specific binding of a target analyte and which generally are immobilized on the surface of the transducer;

2. transducer, which produces a distinguishable signal from the binding event between the sensing elements and the analyte. In particular, the physical or chemical change due to the binding of the analyte (e.g., variation in the thickness, weight, refractive index, molecular structure) is converted into a measurable signal (for example, optical);

3. electronic equipment, including signal amplification, signal processing, and interface circuit for data analysis.

It is worth noting that a proper immobilization of receptors on the sensor surface plays a crucial role. Usually, molecules are not directly immobilized on the inorganic surface to prevent denaturation. In addition, a good immobilization allows efficient coverage of the sensor surface ensuring stability for storage, regeneration and preventing non-specific adsorption of analytes.

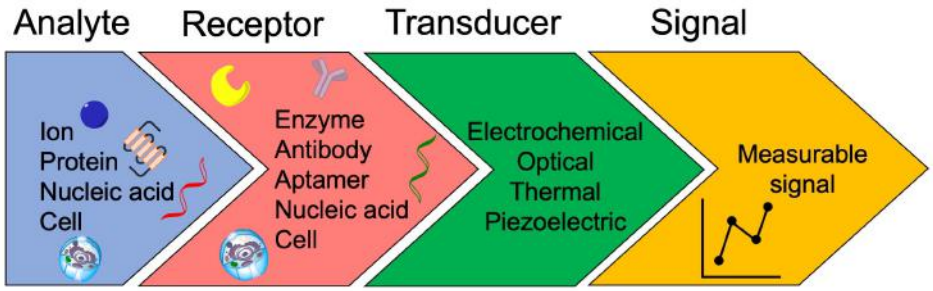

Figure 1.2 – *Diagram of the components and operation of a biosensor. An analyte binds to a receptor; from this binding event, a transducer produces a distinguishable and measurable signal.*

To make a biosensor capable of recognizing different analytes, immobilization of different receptors is required and patterned SAMs must be prepared. In recent years, several methods have been proposed for the fabrication of patterned SAMs, from micro-contact printing [17] to colloidal lithography [18, 19]. These methods typically allow creating structures around $(10 \div 100)\mu$m. An alternative method to reduce the size of the structures is to use atomic force microscopy as a nanolithography tool (section 2.3.3). In this case, the tip of the AFM is used as a shave to remove molecules in selected regions of the film, allowing the deposition of specific functionalized molecule in the shaved areas. The goal is to obtain structures such as those depicted in Figure 1.3, where the platforms are surrounded by an environment refractory to non-specific adsorption of molecules present in the biological sample that could give rise to false positives.

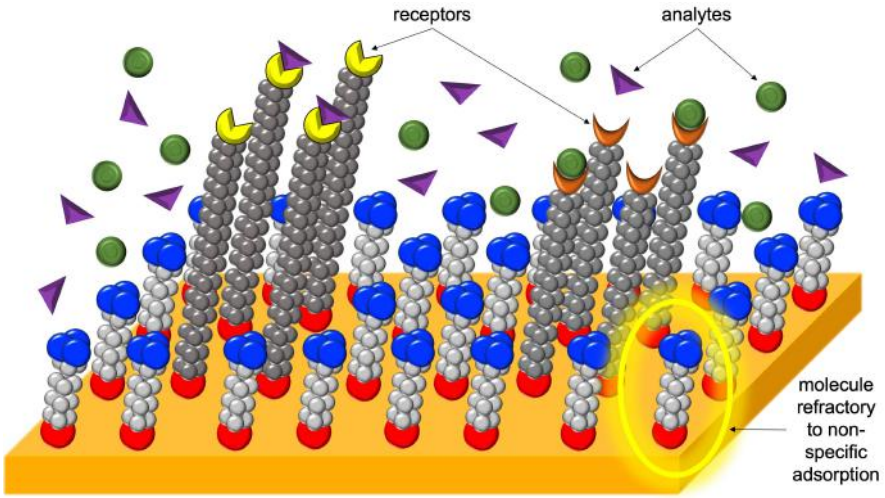

Figure 1.3 – *Sketch of a micro-array able to recognize different analytes. The sensing regions are surrounded by an environment refractory to non-specific adsorption.*

Among all the different types of biosensor, a classification can be made according to three criteria:

- the different receptor types: biocatalytic biosensors (enzyme), immunological biosensors (antibody), nucleic acid biosensors (DNA/RNA);

- the physics of the transduction process: electrochemical biosensors, optical biosensors, thermal (calorimetric) biosensors, piezoelectric (mechanical) biosensors;
- the application fields: medical and clinical biosensors, environmental biosensors, wearable biosensors.

The long-term goal of our research is the development of an immunological and nucleic acid biosensor that can detect, through the same platform, pathological, viral, or toxin-producing nucleic acids and analytes. In particular, in this thesis, we focused on the fabrication and the sensing performance analysis of the nucleic acid detection method, aiming at detecting hybridization between nucleotide chains using a non-destructive, very fast and sensitive technique at the monolayer level. Starting from the choice of the receptors (probe DNA films) and its characterization (through optical and mechanical techniques), we improved and optimized the biological platform (studying the effect of different parameters, like the ionic strength of the buffer and the incubation time). Finally, the receptor/analyte interaction has been unequivocally detected thanks to a spectroscopic fingerprint (260 nm DNA film absorption) that was transduced and analyzed by a spectroscopic ellipsometer (optical method).
The main advantages of employing optical biosensors originate from the high sensitivity, stability, and non-destructiveness (non-ionizing radiation) of the optical techniques used to analyse them [20]. These devices achieve changes in light characteristics when there is binding between receptors and target molecules. Optical devices can detect analytes directly - measuring changes in intensity, wavelength, refractive index, and polarization - or indirectly - detecting labelled probes. We will focus only on label-free biosensors, which overcome the need for fluorescence or radioactive labelling for detection, allowing convenient point-of-care diagnostics.
Higher sensitivity can be achieved with optical plasmonic sensors [21], including surface plasmon resonance (SPR) [22], surface-enhanced Raman scattering (SERS) [23], localized surface plasmon resonance (LSPR) [24, 25] and optical resonator based [26] sensors. In particular, SPR-based biosensors detect biomolecular interactions occurring on the metal surface by measuring the shift in the excitation angle or wavelength of surface plasmon or the optical intensity change [27–29]. Surface plasmon occurs when photons from incident wave interact with electrons in the metal surface.

1.1.1 Self-assembled monolayers

As mentioned above, proper immobilization of receptors on the sensor surface is paramount to prepare efficient biosensing platforms. This immobilization can be direct or indirect introducing an intermediate layer to decouple biosensing molecules from the usually inorganic substrate. This strategy helps to preserve integrity and functionality of the molecules that could denature rapidly due to changes in their surroundings (i.e., the inorganic surface). In this latter case, the sensing elements can be anchored to the surface employing several strategies that exploit specific interactions, e.g., biotin-avidin [30] or nitrilotriacetic acid-histidine [31].

The deposition of the receptors (or of the intermediate organic molecules) on the surface can occur by physisorption (i.e. through weak bonds) or by chemisorption (i.e. through covalent bonds with energy on the order of 200 kJ/mol). Compared to physisorption, chemisorption ensures the formation of films that are more strongly bound to the surface, and therefore more stable. By appropriately choosing the molecule/surface system, it is possible to obtain ordered Self-Assembled Monolayers (SAMs).
The term self-assembled monolayers refers to organic films that spontaneously organize from the liquid or gas phase on a substrate into ordered monolayers. A schematic representation of the molecules that make up a SAM is shown in Figure 1.4. The molecules in a SAM typically consist of: (i) the head group, a surface-active functional group responsible for anchoring the molecule to the surface; (ii) the central group, often an alkyl chain; (iii) the tail group, a terminal functional group that determines the interface properties of the SAM.

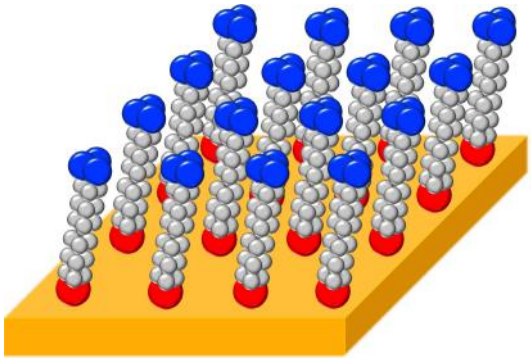

Figure 1.4 – *Sketch of a self-assembled monolayer: head group (red), central group (grey), and tail group (blue).*

Considering the structure of SAM molecules, the organization of the film depends on several interactions: head group/surface interactions, intermolecular chain/chain interactions, intermolecular interactions between the terminal groups. For example, the higher the affinity between the head group and the surface, the more stable and robust the SAM will be. Similarly, as the length of the central chain increases, inter-chain Van der Waals interactions will increase, resulting in more ordered and compact SAMs. Concerning the role of the tail group, it has to be considered that the characteristics of this functional part can interfere with a good packing, such as large steric size (compared to the alkyl chain), non-zero net charge, or non-negligible interaction with the solvent. Therefore, the increasing of functional group complexity can improve the interface properties of the SAM, but can decrease of the molecular organization of the film. A successful strategy, also adopted in this work, is the preparation of mixed SAMs, consisting of both molecules with the functional groups of interest and simpler spacer molecules that aid in film packing.
Self-assembled films have been employed in various fields, to mimic biological systems [32], to protect surfaces from corrosion [33, 34], to confer antimicrobial properties [35], to improve performance in optoelectronic devices [36], to control cell

shapes [37] or cell migration [38].

Thiolated SAMs

Focusing on the head group/surface interactions, various kind of SAMs can be prepared [39]. Between these, the two most studied classes of SAMs are represented by silanes on surfaces of oxides [40–42] and organosulfides on transition metals [43–45]: in both cases, a covalent interaction between the molecule and the surface is established, which allows an extremely effective immobilization of the molecule. In this work, we focused on compounds formed by a thiol $-SH$ group as the head group, an alkyl chain (molecular spacers) as central groups and DNA strands as the tail-probe molecules. Moreover, as described before, we employed an alkanethiol as a molecular spacer, an organic compound derived from alkanes where a hydrogen atom is replaced by a thiol group, $-SH$, with formula $CH_3(CH_2)_{n-1}SH$.
Initially studied by Nuzzo and Allara [46], alkanethiols show a high affinity for transition metals [47], that leads to a high degree of molecular organization and stability of the film [48]. These properties are mainly related to the formation of the strong S-Au bond (head group/surface interaction), with an energy of about 180 kJ/mol [46]. Instead, the intermolecular interactions are dominated by Van der Waals forces established between the alkyl chains, around 5 kJ/mol. Regarding tail groups, they confer specific properties, such as hydrophobicity (-CH_3), hydrophilicity (-COOH or -OH), or allow the indirect anchoring on the surface of the receptors.
Concerning molecular organization, previous studies have shown that alkanethiols on Au(111) form a ($\sqrt{3}$ x $\sqrt{3}$) R30° structure in a hexagonal lattice (i.e., rotated by 30° with respect to the lattice directions of Au(111)) and that the sulphur atoms have a distance between first neighbours of 4.97 $\dot{A}$ [44]. This structure is the result of a well-defined kinetic self-assembly process [49–53], that shows the presence of three main steps:

1. rapid chemisorption, which occurs just after incubation in solution and where molecules interact with the substrate by lying down;

2. slow chemisorption, where the molecules straighten up thanks to the nucleation of the previous step (standing up phase), and the monolayer reaches about 80-90% of the final thickness;

3. ordered domains, where molecules are tightly packed.

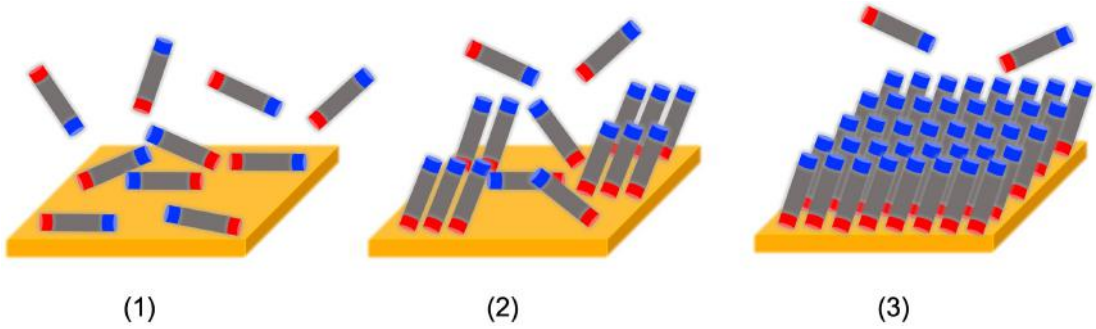

Figure 1.5 – *Representation of the self-assembly process of an alkanethiol film: 1) lying down phase, b) nucleation of the standing up phase, c) completion of the standing up phase and formation of ordered domains.*

1.1.2 DNA-based biosensors

DNA biosensors exploit the highly specific biorecognition property between complementary strands deriving from Watson-Crick base-pairing: the immobilization of a single-stranded DNA (ssDNA) as probe on a surface allows to recognize its complementary sequence by hybridization. DNA-based microarrays are considered as efficient tool for clinical diagnosis since a parallel detection of DNA or RNA hybridization allows the simultaneous multiple detection of biomarkers of various kind [54–56], like oligonucleotides [57], proteins [58] and cells [59]. Indeed, probe DNA (pDNA) strands with different base composition can be immobilized in various micro/nano-regions forming platforms designed for multiple biomarker analysis. Moreover, these sensitive areas can be reused and regenerated through double strand denaturation.

Hybridization can be exploited for biosensing on a two-fold level. The first method is the Direct DNA Immobilization (DDI) that works toward the direct recognition of specific target DNA (tDNA) sequences. In this case, target diseases can be identified from the detection of specific nucleic acid sequences [60] (Fig. 1.6 (a)). For example, Rabti et al. [61] report a DDI biosensor able to recognize f17-related fimbriae sequences, nucleic acids involved in the onset of extra-intestinal infections caused by Enterotoxigenic Escherichia coli released toxins. Another typical employment of DDI sensors is the detection of microRNA (miRNA) strands, small non-coding ssRNA molecules ($\sim$ 22 nucleotides) whose dysregulation can be associated with various diseases [62]. A public database, miR2Disease, documents known relationships between miRNA dysregulation and human disease [63]. A recent and interesting application is the detection of coronavirus-related sequences: in response to the COVID-19 emergency, selective recognition of SARS-CoV-2 sequences based on DNA hybridization has been recently demonstrated using a thermoplasmonic approach [64] and a label-free capacitive method [5].

On the other hand, in DNA-directed molecular anchoring, hybridization is exploited for the immobilization of selective and functional sensing molecules through complementary DNA strands bearing the sensing molecule (Fig. 1.6 (b)). Through this

approach, the receptors exploit an intermediate layer (DNA film) that allows the decoupling from the substrate, and helps to maintain their functionality and selectivity towards specific molecular biomarkers [6, 65, 66].

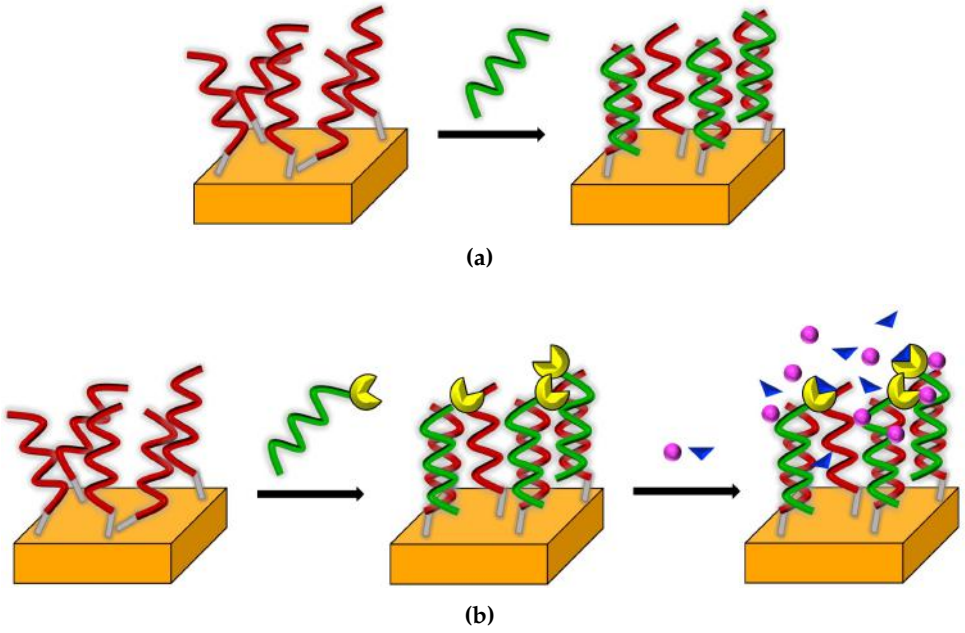

Figure 1.6 – *Sketch of DNA-based biosensors applications. (a) Direct DNA immobilization: recognition of a specific nucleic acid sequence; (b) DNA-directed molecular anchoring: recognition of specific biomarkers through the immobilization of complementary DNAs bearing sensing molecules.*

After hybridization, the biosensor transducer can produce different signals such as electrochemical, optical, or mass-sensitive. Usually, electrochemical devices detect hybridization from modifications of the sensing platform properties (for example, capacitance) or from an intrinsic electrochemical response due to DNA (e.g., oxidation of guanines) [67–69]. Optical sensors can involve the use of fluorescent labels [70, 71], leading to a more complex and expensive preparation procedure for the device fabrication, which could also affect the bioactivity of the target molecule. For this reason, label-free optical devices are often preferred [72–74]. The development of mass-sensitive DNA-based biosensors has been also performed, suggesting interesting applications thanks to the label-free and in-situ procedure [75–77].

1.2 Nucleic Acids

As introduced above, our goal is the fabrication of a label-free DNA-based biosensor. Therefore, the design of a robust and reliable device passes through the careful characterization of the DNA self-assembled monolayer. Moreover, the study of the mechanism of hybridization between complementary strands is crucial since this process is the key to identify pathological nucleic acid strands or to drive the anchoring of sensing molecules on the surface. A focus on nucleic acids will be presented to

better understand the biological system.
Nucleic acids are organic polymers whose monomers, called nucleotides, are composed from a phosphate group (PO^{4-}), a 5-carbon sugar and a nitrogenous base. The two main type of nucleic acids are deoxyribonucleic acid (DNA) and ribonucleic acid (RNA): in DNA the sugar is deoxyribose, while in RNA the sugar is ribose (Fig. 1.7). Nucleic acids transmit information contained in the genetic material inside and outside the cell nucleus. DNA stores and encodes genetic information (i.e., encodes amino acid sequences of proteins responsible for cellular function), while RNA strands, created using DNA strands as a template (transcription), specify the amino acid sequences of proteins (translation) decoding the DNA information.

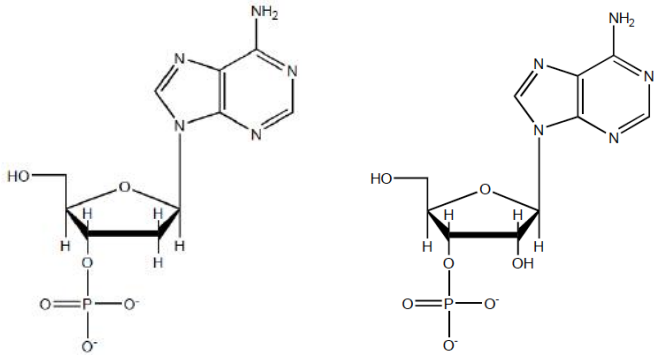

Figure 1.7 – *Comparison between (a) DNA and (b) RNA adenine-nucleotides.*

1.2.1 Bases and interactions

The nitrogenous bases are distinguished into (i) purine: adenine (A) and guanine (G); (ii) pyrimidine: cytosine (C), thymine (T) (only in DNA) and uracil (U) (only in RNA; it is an unmethylated form of thymine) (Fig. 1.8). The bases are bound to the sugar through the N-glycosidic tail, while the nucleotides are joined in a chain by covalent bonds (phospho-diester bonds) established between the sugar of one nucleotide and the phosphate of the next. The resulting strings of nucleotides form a backbone with successively alternate sugar and phosphate, assembled into usually double chains for DNA (double-stranded) and single for RNA (single-stranded). DNA-RNA hybrids are also allowed.

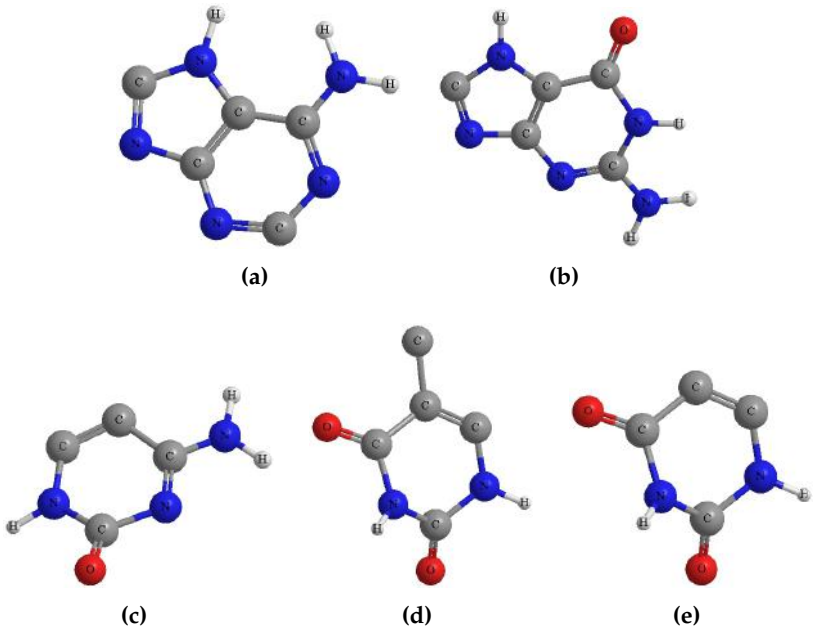

Figure 1.8 – *Sketch of nitrogenous bases: (a) adenine, (b) guanine, (c) cytosine, (d) thymine and (e) uracil.*

The characteristic molecular recognition property of nucleic acids (Watson-Crick base pairing), by which adenine pairs with thymine or uracil, and guanine pairs with cytosine, confers interesting self-assembling properties and provides programmability and predictability to nucleic acid structures. Hybridization between two strands occurs via hydrogen bonds 10.8 $\dot{A}$ long: for steric issues, the complementary bases that pair up must necessarily be a purine and a pyrimidine. Indeed, this distance perfectly fits for a purine/pyrimidine pair, while it is too short for two purines and too long for two pyrimidines.
Adenine and thymine/uracil establish two hydrogen bonds, while three bonds are found between cytosine and guanine. This characteristic aids in forming a cooperative interaction that helps in structure stability. The pairing between bases is further limited by the positions of the hydrogen atoms in the bases: for example, adenine could not pair with cytosine because there would be two H atoms at one binding site and no H atom at the other binding site. The stability of the resultant helix is enforced by weak attractive non-covalent forces caused by the overlapping of π-orbitals, called pi-stacking, of pyrimidine and purine bases, which are parallel to each other [78].
Since hydrogen bonds are non-covalent, they can be broken and reformed fairly easily. Denaturation of the double helix (i.e., splitting the double-strand into two separate chains) can be achieved by mechanical force, high temperature, low ionic strength, or high pH. The stability of dsDNA depends on the GC pair content (pair with multiple hydrogen bonds), the sequence (stacking is sequence specific), and the length of the strands (longer molecules are more stable) [79, 80]. The standard parameter for quantifying DNA stability is the melting temperature, which is the temperature at which 50% of double-stranded molecules are converted to single-stranded molecules. A fundamental nucleic acid feature, deeply exploited in this work, is the UV strong

absorbance. The $\pi \rightarrow \pi^*$ and the $n \rightarrow \pi^*$ transitions of the pyrimidine and purine rings of the nitrogenous bases originate absorptions in the $(200 \div 270)$ nm range (Fig. 1.9) [81–83].

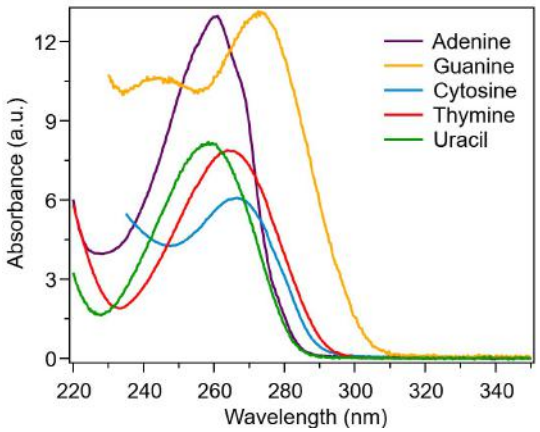

Figure 1.9 – *UV absorptions of nucleic acid bases. From PhotochemCAD database http://photochemcad.com/homepage.php.*

Bonds related electronic transitions associated to σ bonds occur at far UV; similarly, sugars and phosphates contribute to the absorption spectra mainly at wavelengths shorter than 190 nm. Therefore, these bonds have a negligible influence on the spectra recorded in air or water and could contribute only through tails. The amplitude of this absorption can be used to quantify DNA and RNA concentration in a sample.

1.2.2 Nucleotide chains

The deoxyribonucleic acid is the nucleic acid which contains the information for protein biosynthesis. DNA molecules are chemically stable, mechanically rigid, biodegradable, biocompatible and cost effective. These properties lead DNA to play a central role in the development of novel devices, such as in data storage [84, 85], nano-electronic [86, 87], internet of things [88, 89], environment monitoring [90], cellular programming and tissue engineering [91] and pathogen detection [92].
When two complementary strands bind together, DNA organizes itself into an oriented, anti-parallel double chain. The double helix structure of the DNA molecule was first described by J. Watson and F. Crick, in 1953. James Watson, Francis Crick, and Maurice Wilkins were also awarded the 1962 Nobel Prize in Physiology or Medicine "for their discoveries concerning the molecular structure of nucleic acids and its significance for information transfer in living material". Huge contributions to the discovery of the double helix structure were also brought by their colleague Rosalind Franklin.
DNA exists in many possible conformations: double helix, which includes the A-DNA, B-DNA, and Z-DNA forms, or more complex structures such as the G-quadruplex (guanine-rich sequences that help stabilize the ends of chromosomes). Regarding the double helix conformations, the structure adopted by DNA depends

on several parameters such as the level of hydration, the sequence, and the chemical modifications of the bases. The most common structure is the B-DNA (Fig. 1.10), where DNA forms mechanically rigid helical structures with a diameter between 22 and 26 $\dot{A}$ and a helical repeat of 34 $\dot{A}$ (containing 10.5 base pairs). The plane of the bases is perpendicular to the axis of the helix while the plane of the sugars forms an almost right angle with that of the bases. The persistent lengths of duplex and single-stranded DNA are 50 nm [83] and 1-7 nm (depending on the ionic strength) [93, 94], respectively. Oligonucleotide lengths are 3.4 $\dot{A}$/base pair for dsDNA [83] and 4.3 $\dot{A}$/base for ssDNA [93]. Referring to 22-mers, like the ones studied in this thesis work, we expect a length around 7.5 nm for dsDNA helix and of 9.5 nm for ssDNA (excluding thiolated linker).

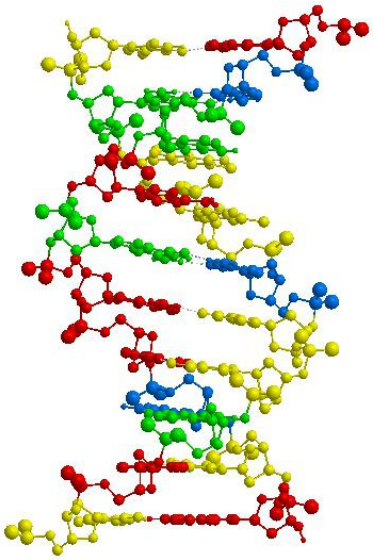

Figure 1.10 – *Sketch of B-DNA. Nitrogenous bases: adenine (red), thymine (yellow), cytosine (blue), guanine (green).*

Also the ribonucleic acid is a nucleic acid which plays fundamental roles for life, for example in the protein synthesis, transmitting information from DNA to ribosome (messenger RNA, mRNA), transferring amino acids to the ribosomes (transfer RNA, tRNA) and linking amino acids together to form coded proteins (ribosomal RNA, rRNA).
Differently from DNA, RNA contains ribose, sugar with a hydroxyl group attached to the pentose ring in the 2' position. These hydroxyl groups make RNA less chemically stable than DNA, since they lower the activation energy of hydrolysis.
RNA is single-stranded and consists of a shorter nucleotide chain. However, some RNAs can contain self-complementary sequences that allow parts of the chain to fold and pair with itself to form highly structured double helices [95]. When RNA is double-stranded, the presence of ribose hydroxyl groups causes the helix to mostly take the A-form structure that consists in alternating a very deep and narrow major groove with a shallow and wide minor groove.
As mentioned before, mixed helices of DNA/RNA are allowed and are important

intermediates in molecular biology [96], leading to a investigation by researchers [97–100].

1.2.3 SAMs

In this work, we decided to exploit the strong S-Au bond to anchor ssDNA on a gold surface, using thiolated DNA (i.e., DNA functionalized with an alkanethiol). Compared to the self-assembly of simpler molecules like alkanethiols, the chemisorption of thiolated DNA strands on gold is a more complex process. In addition to conformation-dependent steric hindrances, the main interactions involved can be summarized as follow:

- head group/surface interaction (S-Au bond);
- interaction between the alkyl chains of the thiolated linkers;
- DNA/linker interaction;
- intermolecular interaction between DNA strands: it depends both on the interaction between nitrogenous bases and on the electrostatic force between the DNA backbones, negatively charged due to the phosphate groups;
- nitrogenous bases/gold interaction: it depends on the affinity degree between the involved base and the metal (T<G<C<A) [101].

Reasonably, the ionic strength of the solution and thus the shielding of charges plays a very important role in the DNA conformation [102, 103], and both of these factors have a strong impact on the self-assembly [104–106]. Moreover, to promote the molecular organization of the DNA strands, spacer molecules can be used [104, 107]. Different experimental approaches have been employed to investigate DNA self-assembly on gold, from electrochemical methods [106, 108, 109], to optical [110–112], infra-red [107, 113, 114] and X-ray [104, 114, 115] spectroscopies.

Chapter 2

Experimental methods for ultra-thin film analysis

This chapter presents the methods employed for the characterization of DNA films. For each technique the theoretical foundations will be given, followed by a description of the instrument. When needed, data analysis method or deeper details about the operational modes will be provided too.
Spectroscopic ellipsometry provides quantitative information about film thickness and optical properties, in addition to chemical-specific information through the detection of molecular absorptions. In the subsections, general issues concerning the investigation of ultra-thin films and their analysis will be discussed. In addition, issues related to the presence of molecular absorptions within films and inter facial effects between film and substrate will be presented.
Surface plasmon enhanced ellipsometry combines the advantages of spectroscopic ellipsometry, performed under total internal reflection conditions, and surface plasmon resonance phenomena. The main advantages of this set-up will be presented.
Atomic force microscopy allows for the monitoring of the morphology of the SAMs and provides, through nanoshaving experiments, estimation of film thickness. In this thesis work, AFM has been employed to perform imaging, nanolithography and force spectroscopy.
X-ray photoelectron spectroscopy is a surface-sensitive method that provides compositional information. It has been used to identify chemical species within the SAM, quantify relative elemental coverages, and obtain information on SAM/substrate interaction.
Quartz-crystal microbalance with dissipation experiments allow for the quantification of the mass coverage on the substrate and studying viscoelastic properties of the film.

2.1 Spectroscopic Ellipsometry

Spectroscopic ellipsometry (SE) is an optical, non destructive and extremely sensitive method which allows for a real-time and in-situ characterization of thin films. SE is based on the analysis, over a wide spectral range, of the change in polarization

of a light beam upon reflection from the sample. Through the comparison between experimental data and simulations obtained from a suitable optical model of the sample, it provides information about optical (refractive index, extinction coefficient, anisotropy), geometrical (thickness, roughness) and material (doping concentration, micro-structure) properties.
This technique is mainly used to characterize multilayer materials [116, 117], patterned films [118] and thin films [119], while we apply SE to the study of ultrathin films (thickness $\leq$ 10 nm) [9, 120, 121].

2.1.1 Optical properties of the materials

Ellipsometry owes its name to elliptical polarization, i.e. the condition where the orthogonal components of the electromagnetic field have different amplitudes and a fixed phase difference. We consider as incident plane the plane defined by the wave propagation direction and the normal to the sample surface, while p(s)-polarization corresponds to electromagnetic waves with their electric field oriented parallel (perpendicular) to the plane of incidence.

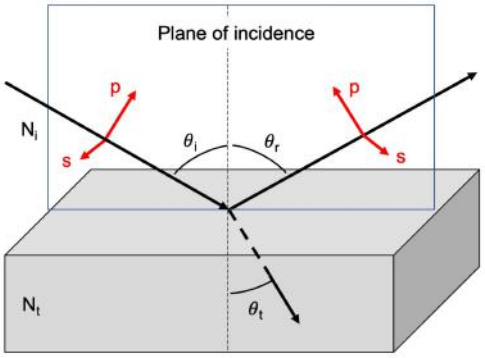

Figure 2.1 – *Sketch of the wave reflection and refraction process, with a focus on the p- and s-component for the incident wave and the reflected wave.*

Various methods can provide direct information on optical properties, such as the absorbance (spectrophotometry) and the reflectance (reflectometry). Both absorbance and reflectance are related to the complex refractive index, defined as

$$\hat{N} = n + ik \tag{2.1}$$

where n is the real refractive index (in the following, we will call it simply "refractive index"), related to the dispersion, and k is the extinction coefficient, related to the absorption. These parameters are related to each other, and, through the Kramers-Kronig equations, it is possible to derive n from k and vice versa.
Both n and k influence the reflectance, which is defined as the ratio between reflected and incident beam intensity (Fresnel law for reflectivity):

$$R = \left|\frac{\hat{N}-1}{\hat{N}+1}\right|^2 = \frac{(n-1)^2+k^2}{(n+1)^2+k^2} \tag{2.2}$$

Instead, the coefficient of absorption α describes the decay of light intensity due to absorption by the material according to the Beer law:

$$I(z) = I_0 e^{-\alpha z} \tag{2.3}$$

where z is the light propagation direction. This coefficient depends on the frequency and is related only to the k coefficient, through the equation

$$\alpha = \frac{4\pi k}{\lambda} \tag{2.4}$$

Therefore a transparent material - material that, by definition, presents zero absorbance - will show an extinction coefficient equal to zero, while in the case of opaque materials k will be positive [122].

The optical properties of materials can be alternatively described in terms of the complex dielectric function (or permittivity) $\hat{\epsilon}$, which quantifies the electric polarizability and is defined as

$$\hat{\epsilon} = \hat{N}^2 = \epsilon_1 + i\epsilon_2 \tag{2.5}$$

The following equations describe in details the relationships between n, k, ϵ_1 and ϵ_2:

$$n = \frac{1}{\sqrt{2}}\sqrt{\epsilon_1 + \sqrt{\epsilon_1^2 + \epsilon_2^2}} \qquad k = \frac{1}{\sqrt{2}}\sqrt{-\epsilon_1 + \sqrt{\epsilon_1^2 + \epsilon_2^2}} \tag{2.6}$$

$$\epsilon_1 = n^2 - k^2 \qquad \epsilon_2 = 2nk \tag{2.7}$$

The complex dielectric function allows to easily discriminate the contribution to a materials response due to the bound electrons and the free electrons:

$$\hat{\epsilon} = \epsilon(\omega) + i\frac{\sigma(\omega)}{\epsilon_0 \omega} \tag{2.8}$$

where ϵ_0 is the vacuum dielectric constant, ω is the angular frequency and, simplifying, $\epsilon(\omega)$ (dielectric function) accounts for the contribution of bound electrons while $\sigma(\omega)$ (electrical conductivity or conductance) accounts for the contribution of free electrons. The dielectric function and the electrical conductivity are proportional factors in the definition of the electric induction ($\vec{D}$) and the current density ($\vec{J}$), respectively.

2.1.2 Working Principles

The optical properties described above can be obtained from the SE experiment through the analysis of Ψ and Δ angles, defined as:

$$\Psi = \arctan\left|\frac{r_p}{r_s}\right| \qquad 0 \leq \Psi \leq 90^\circ \tag{2.9}$$

$$\Delta = \Delta_p - \Delta_s \qquad 0 \leq \Delta \leq 360^\circ \tag{2.10}$$

where r_p and r_s are Fresnel reflection coefficients and $\Delta_{p(s)} = \delta^r_{p(s)} - \delta^i_{p(s)}$ represents the phase difference between reflected and incident wave in the p(s)-component. Δ

allows for the differentiation between different polarization states and, in particular, elliptical polarization defines a state with $\delta_p - \delta_s \neq k\frac{\pi}{2}$ ($k \in \mathbb{Z}$).

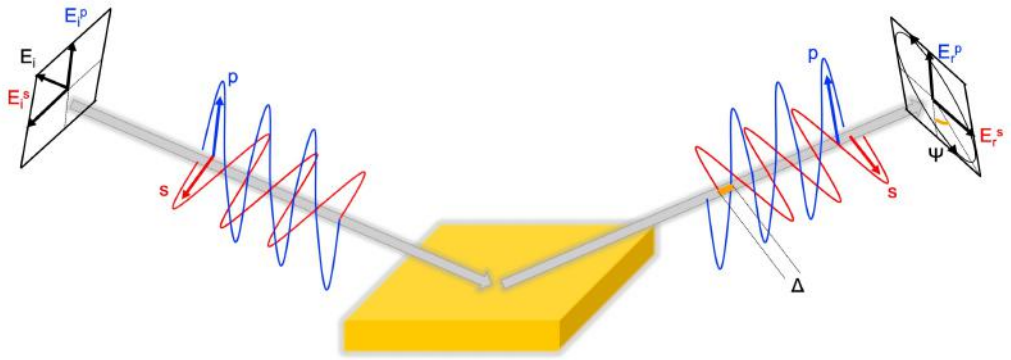

Figure 2.2 – *Measurement principle of ellipsometry. An incident light beam with linear polarization interacts with the sample surface and changes its polarization in elliptical.*

Δ and Ψ angles allow for the measurement of material optical properties thanks to their dependence on Fresnel reflection coefficients. The p(s)-Fresnel reflection coefficient is defined as the ratio between the amplitudes of the reflected and incident p(s)-electric field components, where the complex refractive indexes and the angles of incidence and transmission are involved [123]:

$$r_p = \frac{E_p^r}{E_p^i} = \frac{\hat{N}_2 \cos\theta_i - \hat{N}_1 \cos\theta_t}{\hat{N}_2 \cos\theta_i + \hat{N}_1 \cos\theta_t} \tag{2.11}$$

$$r_s = \frac{E_s^r}{E_s^i} = \frac{\hat{N}_1 \cos\theta_i - \hat{N}_2 \cos\theta_t}{\hat{N}_1 \cos\theta_i + \hat{N}_2 \cos\theta_t} \tag{2.12}$$

From the ratio between Fresnel coefficients, it is also possible to obtain Ψ and Δ bond in a unique variable ρ, which can be directly provided by an ellipsometric experiment [124]:

$$\rho = \frac{r_p}{r_s} = \frac{|r_p|e^{i\Delta_p}}{|r_s|e^{i\Delta_s}} = \tan\Psi e^{i\Delta}. \tag{2.13}$$

2.1.3 Instrument

An ellipsometer is an instrument that measures the change in the polarization state of the light following the reflection from a sample, which acts as an optical element in the experiment. Therefore, the experimental set-up needs to identify the incident beam polarization (through a polarizer or "polarization state generator") and measure the reflected beam polarization (through a second polarizer, often called analyzer or "polarization state detector") before that a detector (a photodiode matrix) collects the light. The accuracy of the experiment improves by employing a well-collimated white light beam.
A compensator can be employed as retarding element, propagating light with different speeds along two polarization axes and shifting the phases. When the compensator is a rotating element, we refer to the instrument as a rotating compensator

ellipsometer (RCE).
Moreover, if the instrument works at multiple wavelengths, it is called a spectroscopic ellipsometer. In this case, a dispersive element that decomposes the reflected beam into different wavelengths is needed.

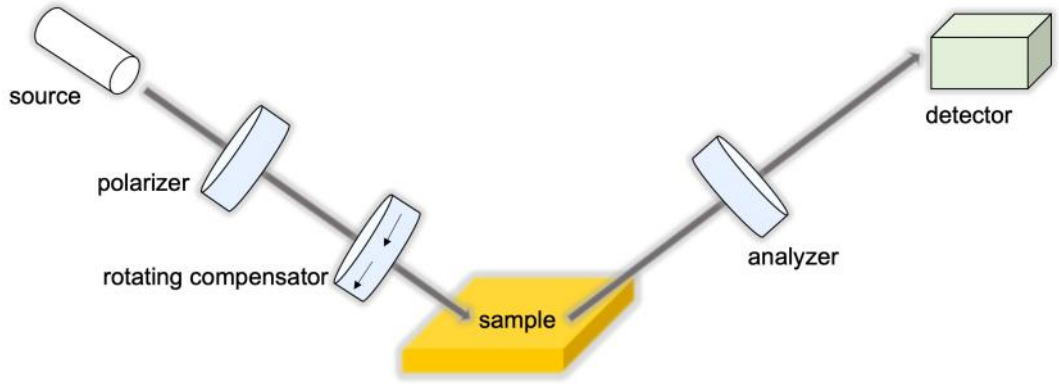

Figure 2.3 – *Scheme of a rotating compensator ellipsometer, as the M2000 Woollam ellipsometer employed in this thesis work.*

2.1.4 Employing difference spectra for data analysis

The presence of an ultrathin film, like a DNA SAM, induces in Δ and Ψ spectra very small changes which can be highlighted using difference ellipsometric spectra, or differential spectra, obtained as the difference between the spectra acquired after (substrate+film+ambient) and before (substrate+ambient) the deposition of molecules on the substrate (Fig. 2.4 (a)).
It is worth noting that the difference spectra, in the case of a thin film on a semi-infinite substrate, reflect both the optical properties of the film and of the substrate. In particular, for example, the difference spectra of the same transparent layer laid on gold (Fig. 2.4 (c)) or on silicon (Fig. 2.4 (e)) will appear definitely different.
For ultrathin films that cause such small variations to SE spectra, a high level of experimental condition reproducibility is required, from the liquid cell mounting to the beam alignment. Moreover, care must be taken not to move the in-situ SE cell (or the elements connected to it, as the tubes) during the entire data acquisition. A repeatable cleaning procedure of the substrates is needed as well in order not to induce morphological changes on the substrate in different experiments, which could hinder measurement reproducibility.

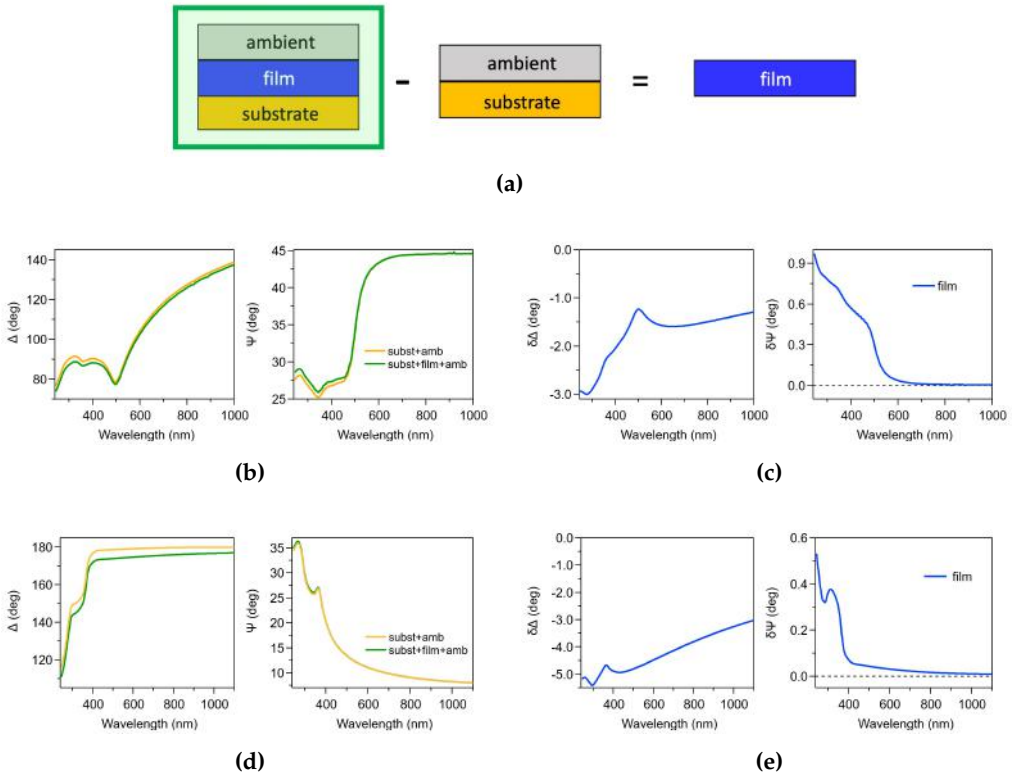

Figure 2.4 – *Difference spectra principle. a) Representation of the difference spectra method. b) Simulated* Δ *and* Ψ *spectra of a gold substrate before (yellow) and after (green) the film deposition. c) Simulated* $\delta\Delta$ *and* $\delta\Psi$ *spectra, referred to b). d) Simulated* Δ *and* Ψ *spectra of a silicon substrate before (yellow) and after (green) the film deposition. e) Simulated* $\delta\Delta$ *and* $\delta\Psi$ *spectra, referred to d).*

2.1.5 Optical models

In order to obtain quantitative information from SE measurements, it is necessary to develop an optical model of the sample. Models are usually constructed as a stack of optical layers, each with its own thickness t and dielectric function $\hat{\epsilon}$, separated by sharp interfaces characterized by Fresnel boundary conditions. Given a model with its associated set of parameters, theoretical Ψ and Δ curves can be generated and fitted to the experimental data by appropriate optimization of the model parameters. The choice of the dielectric function representing each layer depends on the type of material under consideration. For dielectric materials in the region of transparency ($k = 0$), the Cauchy model is widely employed [122, 125]. For samples with absorptions in the UV-Vis region, models with oscillators such as Gauss, Lorentz, and Tauc-Lorentz are suggested.

It is worth noting than, in case of ultrathin films, a certain degree of correlation between the parameters can be found in optical models: in particular, similar simulated curves can be obtained employing different thickness or optical functions for the layers. This issue can be overcome backing SE experiments with independent thickness measurements, as the AFM nanoshaving results, disentangling the contribution of thickness and optical functions to SE spectra. To take into account this correlation,

in SE spectra we will refer to "optical thickness", a quantity depending both on film thickness and film optical properties.

As mentioned above, to model transparent materials (k=0) such as thiols, we can use the Cauchy model defined by the equation:

$$n(\lambda) = A + \frac{B}{\lambda^2} + \frac{C}{\lambda^4} \tag{2.14}$$

where λ is the wavelength and A, B and C are the free parameters of the model (in all the simulations we will assume C=0 μm^4). In this thesis work, also ambient layers are modelled using the Cauchy model. In particular, starting from Krivacic results [126] and taking into account the salt concentration [127], for the TE buffer we used A=1.333, B=0.0028 μm^2, C=0.00005 μm^4 for the 1 M NaCl TE buffer and A=1.322, B=0.003 μm^2, C=0.00003 μm^4 for the 1 mM NaCl TE buffer.

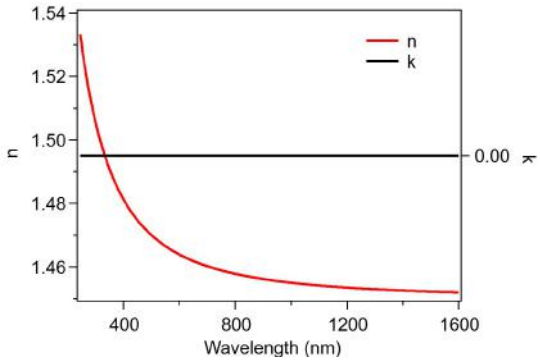

Figure 2.5 – *Refractive index n and extinction coefficient k of a Cauchy layer with A=1.45, B=0.005 μm^2 ($k = 0$ since the Cauchy model represents a transparent layer).*

As mentioned before, the difference spectra highlight the variations in thickness and optical properties of the film deposited on the substrate. In Figure 2.6, simulations based on an ex-situ optical model (i.e., where the ambient is air, with n=1 and k=0) are reported, in order to show the dependence of difference spectra on the various Cauchy parameters (model: substrate | transparent layer | ambient).
We can observe that the thickness of the Cauchy layer definitely affects both parameters: Δ in the whole spectral range, while Ψ only in the UV-Vis region. On the other hand, by varying the refractive index parameters A and B, Δ is mainly modified in the UV-Vis region, while in Ψ only negligible variations are detectable.

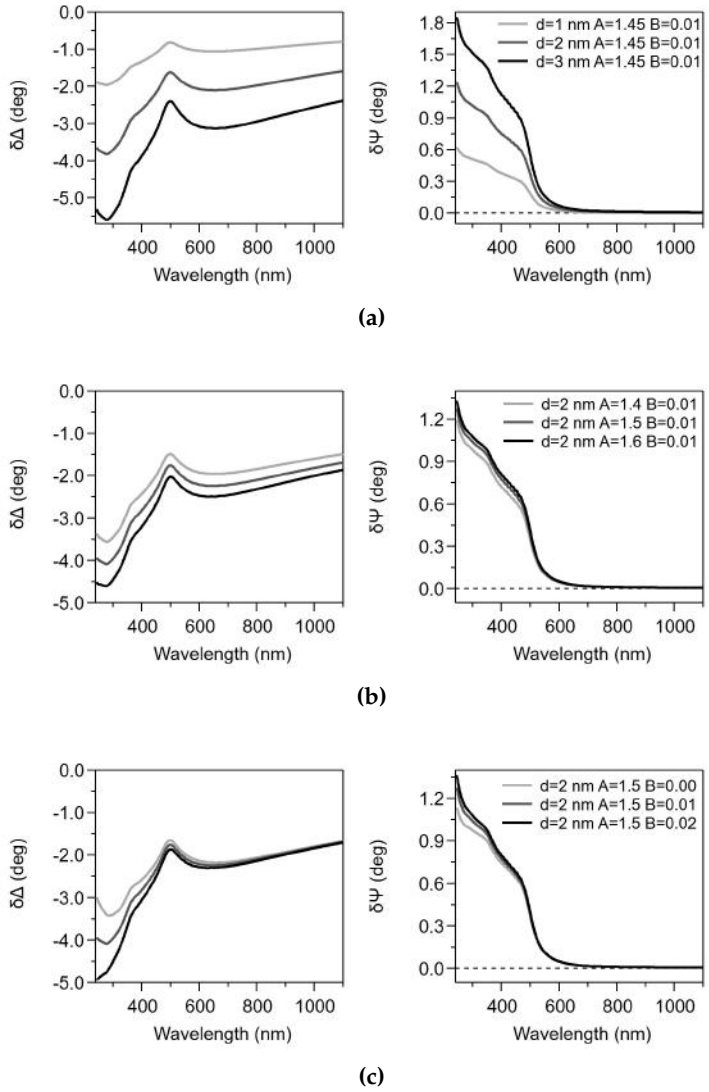

Figure 2.6 – *Difference spectra behaviour of a transparent layer deposited on gold, in air (simulations). (a) Effect of the variation of the Cauchy layer thickness (A=1.45, B=0.01 μm^2). (b) Effect of the variation of the Cauchy A-coefficient (d_{Cauchy}=2 nm, B=0.01 μm^2). (c) Effect of the variation of the Cauchy B-coefficient (d_{Cauchy}=2 nm, A=1.5).*

In contrast, for materials that exhibit optical absorption such as the DNA layer, the dependence of $\hat{N}$ on λ is definitely more complex and there is a large variety of oscillator models and dispersion equations. The General Oscillator Layer (GenOsc) from W-VASE library is an excellent tool that allows to easily combine more oscillators to model the layer dielectric function and to account for absorptions outside the probed spectral range (through $\epsilon_{1\infty}$ and poles) too. The GenOsc model is Kramers-Kronig consistent.

Between the different available oscillator shapes, the Gaussian function is suitable for organic and multi-absorbing film, like DNA SAMs. In a GenOsc layer with Gaussian oscillators, the simulated dielectric function is defined as

$$\hat{\epsilon} = \epsilon_{1\infty} + Pole(A_p, E_p) + Gaussian(A_G, B_G, E_G) \tag{2.15}$$

$\epsilon_{1\infty}$ is an offset parameter which accounts for the cumulative effect of absorptions outside the short-wavelength instrumental limit and it is chosen to give a reasonable n value in the NIR (around 1.45 for organic films). Also the pole function accounts for absorptions that occur outside the measured spectral range and is represented by a Lorentzian oscillator with no broadening, with a complex dielectric function defined as

$$\hat{\epsilon}_{pole} = \frac{A_{Pole}}{E_{Pole}^2 - E^2} \tag{2.16}$$

Finally, the Gaussian function is defined with:

$$\epsilon_{1,G} = \frac{2}{\pi} P \int_{-\infty}^{\infty} \frac{\zeta \epsilon_{2,G}(\zeta)}{\zeta^2 - E^2} d\zeta \tag{2.17}$$

$$\epsilon_{2,G} = A_G * e^{-\left(\frac{E-E_G}{\sigma}\right)^2} - A_G * e^{-\left(\frac{E+E_G}{\sigma}\right)^2}, \qquad \sigma = \frac{B_G}{2\sqrt{ln(2)}} \tag{2.18}$$

In Figure 2.7, ϵ_1/ϵ_2 and n/k referred to an absorbing GenOsc layer with a Gaussian oscillator at 3 eV are reported. In this simulation, $\epsilon_{1\infty}$ was fixed at 2: it is worth noting that this value defines the asymptote to which ϵ_1 curve tends at the ends of the spectral energy range.

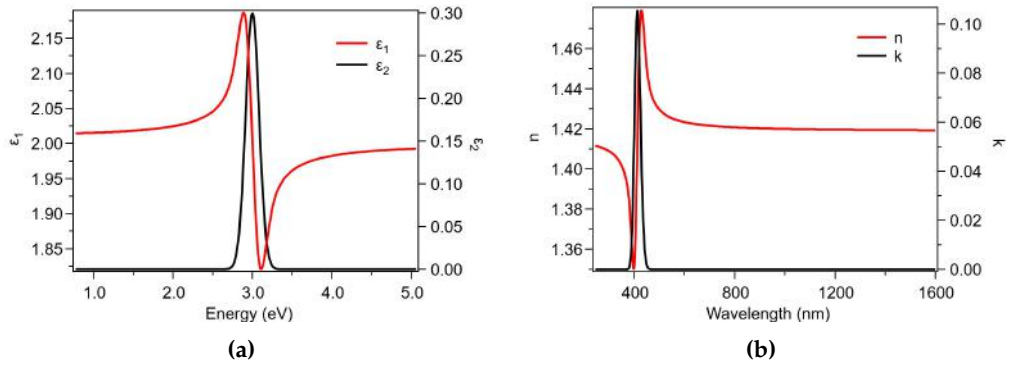

(a) **(b)**

Figure 2.7 – *Optical functions of a Gaussian oscillator centred at 3 eV. (a) ϵ_1 and ϵ_2, versus energy. (b) n and k, versus wavelength.*

The models mentioned so far refer to samples with homogeneous uniform films. Inhomogeneities such as surface roughness, inclusion of a material into another, or non-sharp separation between layers and consequent interface effects, must be considered and included in the model, especially in case of ultrathin films. These effects can be modelled using an effective medium approximation (EMA). So, starting from a situation where two or more materials can coexist within the same layer, an effective dielectric function is constructed to describe the optical behaviour: in particular, it is possible to model the inhomogeneities of a so-called "effective" layer that takes into account the overall optical properties of the sample.
If in the inhomogeneous layer there is no material that prevails, as in the case of interface effects due to the interaction between the layers, the most widely used EMA model is the Bruggeman model [128]. The dielectric function of the effective medium

$< \hat{\epsilon} >$ represents an effective function and not a real one. For a two-material system a and b, with f_a fraction of the a constituent material, we obtain

$$f_a \frac{\hat{\epsilon_a} - < \hat{\epsilon} >}{\hat{\epsilon_a} + 2 < \hat{\epsilon} >} + (1 - f_a) \frac{\hat{\epsilon_b} - < \hat{\epsilon} >}{\hat{\epsilon_b} + 2 < \hat{\epsilon} >} = 0 \tag{2.19}$$

In Figure 2.8, simulations based on an ex-situ model are reported, in order to show the dependence on the EMA parameters (model: substrate | interface | transparent layer | ambient).
We can observe that the thickness of the EMA layer affects both parameters in the whole spectra range; regarding Ψ, larger changes are detected in the Vis-NIR region while only small variations are observed in the UV range. On the other hand, by varying the relative percentages of the media that compose the interface EMA layer, Δ remains almost constant while Ψ shows slight variations in the whole spectral range. In this thesis work the EMA layer has been employed to mix the optical properties of the transparent layer (medium A, Cauchy film) and the substrate (medium B, gold).

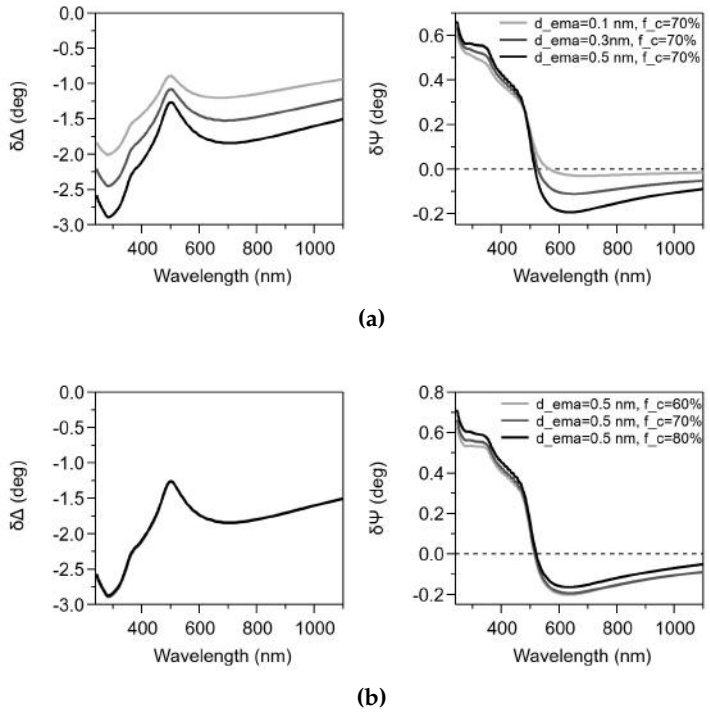

Figure 2.8 – *Difference spectra behaviour for a transparent layer (Cauchy layer: d_{Cauchy}=1 nm, A=1.45, B=0.005 μm^2) which shows interface effects with the gold substrate (simulations). (a) Effect of the variation of the EMA layer thickness ($f_{Cauchy} = 70\%$). (b) Effect of the variation of the percentage of a medium (Cauchy layer) (d_{EMA}=0.5 nm).*

2.2 Surface Plasmon Enhanced Ellipsometry

An increase of the SE experiment sensitivity can be obtained exploiting spectroscopic ellipsometry in total internal reflection condition coupled with surface plasmon resonance (SPR) phenomena. In fact, the use of an ellipsometer in Kretschmann

configuration allows for in-depth monitoring and analysis of the adsorption and desorption of organic layers on thin metal films [3, 129], including the possibility of monitoring surface processes in opaque solutions.
This technique is called Surface Plasmon Enhanced Ellipsometry (SPEE) [130] or, more often, Total Internal Reflection Ellipsometry (TIRE) [27, 73, 131–133].

2.2.1 Working Principles

The SPEE method couples two physical phenomena: (1) the total internal reflection of the light beam at the interface between an optical prism and a metallic layer and (2) the surface plasmon resonance.

Total internal reflection requires two conditions:

- the light has to travel from a medium (incident medium) with a higher refractive index $\hat{N}_1$ to a medium (transmitting medium) with a lower refractive index $\hat{N}_2$;
- the incident angle θ_i has to be larger than the critical angle $\theta_c = \arcsin \frac{\hat{N}_2}{\hat{N}_1}$, angle at which no light is transmitted to the second medium.

Therefore, in a standard experiment, reflectivity shows a strong increase at the critical angle and remains constant for $\theta_i > \theta_c$, avoiding the transmission to the second medium.

SPEE requirements are always satisfied if the set-up is configured to achieve the SPR condition. Surface plasmon resonance sensors are based on the angular measurement of reflectance R_p of p-polarized light at the dielectric/metal interface [134, 135]. Under specific conditions for the wavelength and incidence angle of the incoming beam, the photon energy is transferred to surface electrons and a rapid decrease in R_p is observed (since the decay of the optical field into the metal is exponential) [136]. A surface plasmon wave can be excited at a metal/gas or a metal/liquid interface, with a wave vector k_{spr}. In particular, the term surface plasmon indicates a collective oscillation of surface free electrons parallel to the metal layer surface. For this reason, since the evanescent wave propagates at the interface between the metal and the layer (for example, ambient), only p-polarized incident waves can excite the surface plasmons.
In SPR conditions, reflectivity is high for $\theta_i < \theta_c$ (the metal layer acts as a mirror), while for angles higher than θ_c it shows a strong decrease to zero followed by an equally fast increase, showing a sharp absorption dip feature [137]. The angle of the "zero decay" is defined as θ_{SPR} (note that θ_{SPR} is always larger than θ_c, so SPR conditions satisfy also total internal reflection conditions).

The resonance condition is highly sensitive to the material properties at the metal/dielectric interface. In particular, if any change occurs near the metal surface, e.g. organic molecules are adsorbed onto the metal, the minimum in reflectance is shifted to

different angles of incidence (SPR standard experiment) or wavelengths (SPEE experiment).
In SPEE measurements, which detect Δ and Ψ angles instead of just R_p, Ψ spectra present a dip and Δ spectra present a steep jump. Δ curves are more sensitive to changes at the interface than Ψ spectra [131]. At fixed angle, changes at the interface result in a shift of Δ and Ψ curves to longer wavelengths associated with a change of the SPR feature intensity.

The condition necessary to transfer energy from photons to electrons and to obtain the SPR effect is that the wave momentum of the incident beam k_i equals that of the evanescent wave k_{spr}, defined as

$$k_i = \frac{2\pi}{\lambda_i} n_{prism} \sin\theta_i, \tag{2.20}$$

$$k_{spr} = \frac{2\pi}{\lambda_i} Re\left[\sqrt{\frac{\hat{\epsilon}_{Au}\hat{\epsilon}_{layer}}{\hat{\epsilon}_{Au}+\hat{\epsilon}_{layer}}}\right] \tag{2.21}$$

Therefore, imposing the condition for SPR effect $k_i = k_{spr}$ and considering a non-absorbing layer ($\hat{\epsilon}_{layer} = n_l^2$), we obtain that θ_i should be equal to

$$\theta_{SPR} = arcsin\left(\frac{1}{n_{prism}} Re\left[\sqrt{\frac{n_l^2(\epsilon_{1,Au}+i\epsilon_{2,Au})}{(\epsilon_{1,Au}+i\epsilon_{2,Au})+n_l^2}}\right]\right) \tag{2.22}$$

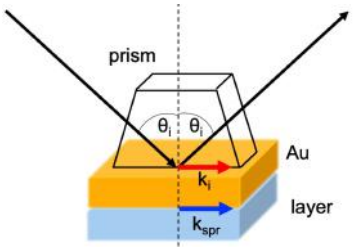

Figure 2.9 – *SPR scheme in Kretschmann configuration. Total internal reflection and equality between the moment of the incoming light and the moment of the plasmon are necessary conditions for SPR phenomena.*

In this thesis work, we performed experiments using gold substrates with $\hat{\epsilon}_{Au} = -13.685 + i1.74$ ($\lambda = 610$ nm) ($n_{Au} = 0.235; k_{Au} = 3.7068$), a BK7 prism with $n_{prism} = 1.5136$ ($\lambda = 610$ nm) and a dielectric layer representing the ambient (air, water) with n_l. For air ($n_l = 1$) and water ($n_l = 1.33$), SPR features can be obtained at

$$\theta_{SPR}^{air} = 43.4^\circ, \quad \theta_{SPR}^{wat} = 70.12^\circ \tag{2.23}$$

Usually, gold and silver are employed for surface plasmon resonance experiments. In particular, gold is inert and does not require particular treatments to avoid oxidation. The thickness of the metal layer is a crucial parameter to obtain sharp and deep SPR features. The best gold thickness is around 50 nm [138].

Figure 2.10 and Figure 2.11 report simulations based on a simple optical model which accounts for the BK7 prism, the Ti primer layer, the Au substrate and the dielectric layer (air, water, and 1 M NaCl TE buffer). The comparison between different environments (dielectric layers) is shown, with examples at fixed incident wavelength and at fixed incident angle. Note that, for the W-Vase software employed for optical simulations, the incident medium (BK7) has to be considered as the ambient. BK7 and dielectric layers have been simulated through the not-absorbing Cauchy model.

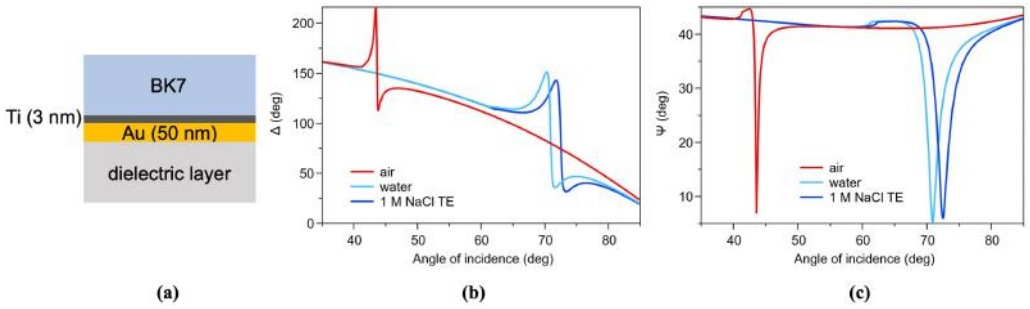

Figure 2.10 – *SPEE simulations. (a) Optical model. (b) Δ and (c) Ψ simulated spectra vs. incident angle θ_i, at λ_i=641 nm. Comparison between air (A=1, B=0 μm^2, C=0 μm^4) (red), water (A=1.3215, B=0.003 μm^2, C=0.00003 μm^4) (light blue) and 1 M NaCl TE buffer (A=1.333, B=0.0028 μm^2, C=0.00005 μm^4) (blue).*

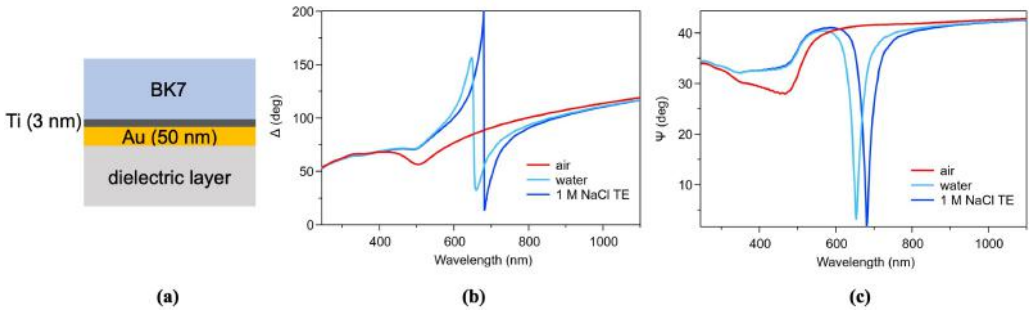

Figure 2.11 – *SPEE simulations. (a) Optical model. (b) Δ and (c) Ψ simulated spectra vs incident light λ_i, at 70°. Comparison between air (A=1, B=0 μm^2, C=0 μm^4) (red), water (A=1.3215, B=0.003 μm^2, C=0.00003 μm^4) (light blue) and 1 M NaCl TE buffer (A=1.333, B=0.0028 μm^2, C=0.00005 μm^4) (blue).*

Figure 2.12 compares SPEE simulations obtained for different θ_i considering as ambient medium 1 M NaCl TE buffer. These simulations show as effectively the angle to which the feature SPR is sharper, for an aqueous solution like 1 M NaCl TE buffer, is around the 70°, as calculated in Eq. 2.23.

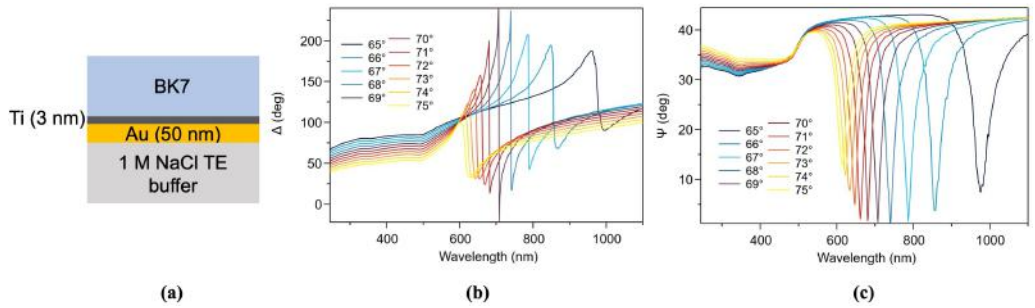

Figure 2.12 – *SPEE simulations. (a) Optical model. (b) Δ and (c) Ψ SPEE simulations obtained for different θ_i in 1 M NaCl TE buffer (A=1.333, B=0.0028 μm^2, C=0.00005 μm^4).*

2.2.2 Instrument

Surface plasmon resonance requires the use of an optical prism. In particular, SPEE configuration requires that the incident light beam penetrates into the prism with an incident angle θ_i equal to θ_{SPR}. This angle depends on many parameters, for example the ambient (and its refractive index): an ex-situ measurement requires $\theta_{SPR}^{air} = 43.4°$ while an in-situ experiment needs $\theta_{SPR}^{wat} = 70.12°$ (Eq. 2.23). For this reason, a goniometer (in our case, already included in the SE instrument) is necessary. In this thesis work, we exploit the Kretschmann configuration where the metallic film is evaporated directly on the prism; the alternative Otto configuration requires a little distance between the metal and the prism. Actually, considering that the direct evaporation of the metal on the prism would complicate the cleaning procedure and the maintenance of the set-up, we used a BK7 substrate with an evaporated thin gold layer coupled with the BK7 prism through a index matching liquid.

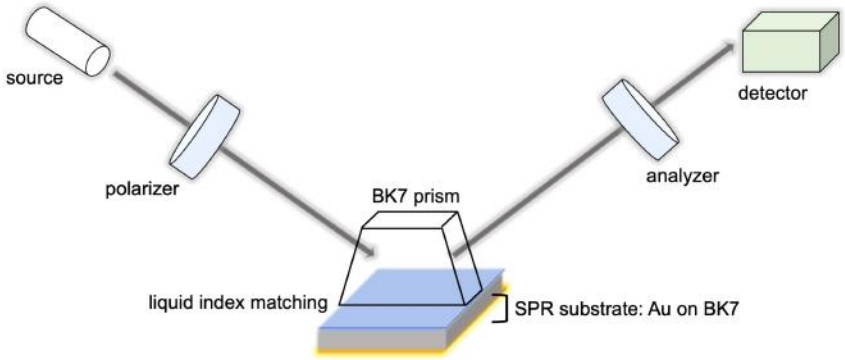

Figure 2.13 – *Scheme of a typical SPEE configuration: a spectroscopic ellipsometer is configured so that a SPR is detected at the interface between the substrate and an appropriate optical prism in Kretschmann configuration.*

2.3 Atomic Force Microscopy

The Atomic Force Microscope (AFM) was invented in 1986 by G. Binnig, C. Quate and C. Gerber [139], and quickly became one of the most important tools for nano-scale

study. AFM belongs to the scanning probe microscopies, that provide high-resolution point by point information, exploiting different interactions between a sharp tip (probe) and the sample, like the tunnel effect (scanning tunnelling microscope) or the optical density (scanning near-field optical microscopy). In the case of atomic force microscopy, the tip-sample interaction forces are exploited. AFM allows for the characterization of samples through imaging, spectroscopy and nanolithography with molecular resolution. In particular, lateral resolution is around 1 nm, vertical resolution is 0.1 nm while force resolution can reach pN values. Moreover, atomic force microscopy is strongly recommended for the study of biological samples, because it does not require conductive samples and allows in-situ work in a liquid environment.

2.3.1 Working Principles

As mentioned above, scanning probe microscopies exploit the various interactions that occur between a surface and a probe recording the probe-sample interaction while the tip scans over the surface and using it to reconstruct the topography of the sample. In the case of AFM, the probe used to image the surface is a tip with a curvature radius in the order of 10 nm and placed at the apex of a flexible cantilever. The interaction forces established between the tip and the sample cause a deflection of the lever whose analysis allows to derive information about the surface. In particular, both short-range (r $<$ 1 nm) and long-range forces may be involved. Short-range forces (contact-mode) are predominantly repulsive forces due to the Pauli exclusion principle involved when the distance between tip and surface atoms is so short that electron clouds partially overlap. Long-range forces (non-contact mode), with an interaction range up to 100 nm, are typically attractive, being dominated by the Van der Waals forces with possible additional electrostatic, magnetic and adhesion contributions. In particular, Van der Waals forces, with an intensity of the order of $(10^{-8} \div 10^{-11})$ N, are due to various dipole-dipole interaction terms resulting into an interaction energy that can be represented through the Lennard-Jones potential:

$$V(r) = 4\epsilon \left[\frac{A}{r^{12}} - \frac{B}{r^6} \right] \tag{2.24}$$

where r is the inter-atomic distance and $-\epsilon$ is the value of the energy at the equilibrium position (i.e., the depth of the hole).

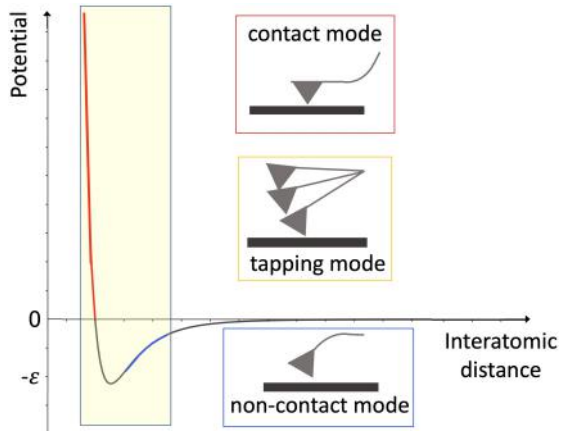

Figure 2.14 – *The Lennard-Jones potential and the potential ranges of AFM operation modes: contact mode (red) - repulsive forces; non-contact mode (blue) - attractive forces; tapping mode (yellow) - oscillation between attractive and repulsive forces.*

The interaction force between tip and sample can be expressed through the Hooke law

$$F = k\Delta z \tag{2.25}$$

where k is the spring constant and Δz the deflection of the lever. The spring constant can be calculated from the geometric characteristics of the lever [140, 141] and experimentally evaluated by the thermal tune method [142, 143]. In particular, the interaction force between tip and sample can be investigated by acquiring force-distance curves. Figure 2.15 reports a scheme of an AFM force-distance curve, where the following steps can be distinguished:

a) *approach*: the tip approaches the sample;

b) *jump to contact*: the gradient of the attractive forces exceeds the elastic constant of the lever, the lever deflects downward and the tip and sample come into contact;

c) *contact*: the tip is in contact with the sample; the repulsive force causes an upward deflection of the lever;

d) *adhesion*: the tip is retracted; because of adhesion (attractive) forces, it deflects in the opposite direction;

e) *pull-off*: tip is released from the sample.

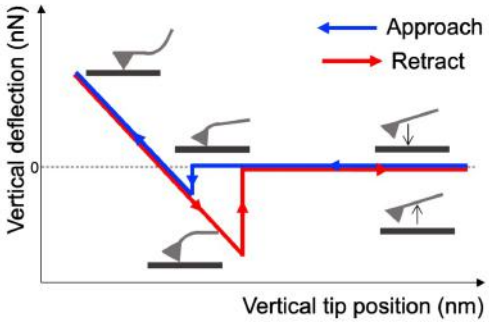

Figure 2.15 – *Force-distance AFM curve scheme: (a-b) following the approach of the AFM tip to the sample, the lever deflects downward and the tip and sample come into contact; (c) when the tip is in contact with the sample, an upward deflection of the lever is detected; (d-e) finally, when the tip is retracted, the lever deflects in the opposite direction until the release from the sample.*

2.3.2 Instrument

Atomic force microscopy studies the interaction between a tip, fixed at the apex of a flexible cantilever, and the surface, analyzing the deflection/torsion of the cantilever. One of the most used methods to detect the deflection of the lever is the optical lever method, where a laser beam is reflected from the back surface of the cantilever onto a four-segmented photo-diode: having set the reflected beam in the center of the diode, it is possible to detect any variation of the cantilever deflection by checking the laser signal intensity on the four segments.
The scanning and relative motion between surface and tip is achieved using a piezoelectric scanner, able to control the position of the lever in the x-y plane and in z with sub-nanometre precision exploiting a complex feedback system which tunes the polarization of the piezoelectric.

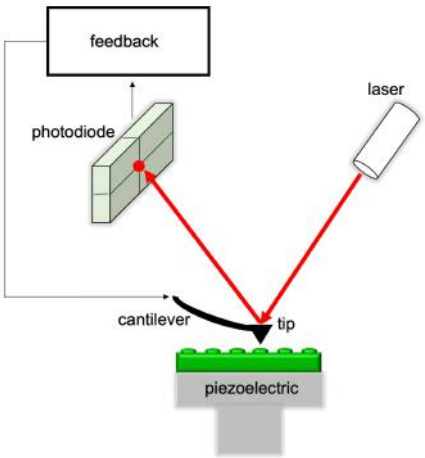

Figure 2.16 – *AFM scheme: a tip scans a sample through a piezoelectric scanner. Morphological and tribological information are obtained thanks to the analysis of the cantilever deflection (in this scheme, deflection is detected with the optical lever method).*

A key parameter in determining the lateral resolution of the instrument is the radius of curvature of the tip, typically a few nanometres. The finite size of the tip results in a broadening of the lateral dimensions of the structures, since the acquired image profile is a convolution of the sample profile with the tip profile (Fig. 2.17).

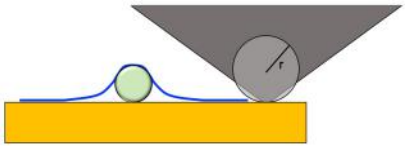

Figure 2.17 – *Importance of the curvature radius of the tip: convolution effect of the sample profile with the tip profile.*

As concerns the probe, another important parameter is the elastic constant of the lever which has to be chosen according to the AFM operation mode. In particular, in contact mode softer levers are needed to avoid damaging the sample, generally with $k \leq 1$ N/m, while in tapping mode the value oscillates between 20 and 100 N/m.

2.3.3 Operation modes

In this thesis work the AFM has been used as an imaging, spectroscopy, and nano-lithography tool. The different uses will be explained individually in detail in the following section.

Figure 2.18 – *AFM operation modes employed in this thesis work: QI mode, contact mode, and hard-tapping mode. These operation modes can provide different types of information.*

Force spectroscopy: quantitative imaging mode

Quantitative imaging (QI) is a force-distance curve-based microscopy mode that provides, simultaneously, a height image and a map of different sample properties with nanometre resolution. In fact, through the acquisition of a large set of force-distance curves, QI allows for the reconstruction of the sample topography from the z position of the tip at a specific force load. Since the tip is withdrawn from the surface between each pixel, there are almost no lateral forces, and dragging is avoided. The combination of imaging and force spectroscopy provides simultaneously quantitative data on local mechanical properties, such as the stiffness and the Young modulus, and morphological information.
In QI mode, the stiffness of the analyzed region can be inferred from slope maps obtained by calculating, for each acquired force-distance curve, the slope of a linear fit of the contact region close to the sample surface. In particular, the fit is adapted to

the extending curve. Figure 2.19 reports a typical experimental force-distance curve acquired in QI mode on a biological soft sample.

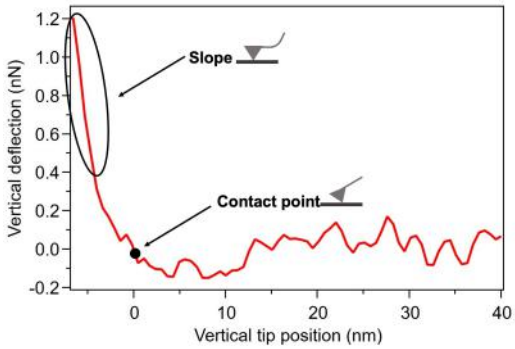

Figure 2.19 – *Example of the extending trace in a force-distance curve acquired in QI mode.*

Instead, the Young modulus of the sample can be calculated applying the Hertz model [144] to the contact region of the extending curve starting from the contact point. The original Hertz model was developed to describe the contact between two spheres, but nowadays the term is usually used to refer to a family of different models that have been adapted for simple indentation geometries [145, 146]. For example, in our experiment, a parabolic shape for the tip (radius: 10 nm) was considered.

Nanoshaving: contact mode and hard tapping mode

The AFM can be used as a lithography tool to structure SAMs at the nano/micrometer scale by nanoshaving and nanografting. The first work was presented in 1997 by Song Xu and Gang-Yu Liu who grafted octadecanethiol in a decanethiol film fabricating nanometric structures [147].
Nanoshaving employs the AFM tip as a shaver: applying an high load during the scan the tip removes, in defined regions, molecules from the SAM. The depth of the shaved areas provide an accurate estimate of the film thickness in solution.

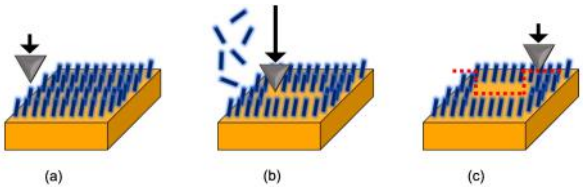

Figure 2.20 – *Scheme of the nanoshaving process: (a) first preliminary scan: larger size, low tip load; (b) second scan: removal of molecules applying a high tip load; (c) third scan: acquisition of an image with larger size to estimate the film height.*

The term nanografting refers to a technique derived from shaving by which, working in a solutions of molecules B, the molecules previously adsorbed on the substrate (molecules A) are removed and replaced by molecules B [148, 149]. In this way it is possible to immobilize molecules in defined nano-micro regions and estimate film thickness difference between SAM A and SAM B [150, 151].

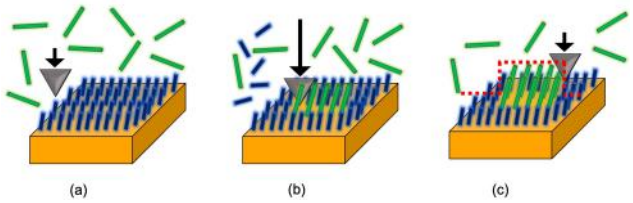

Figure 2.21 – *Scheme of the nanografting process. The SAM of molecules A (blue) is exposed to a solution of molecules B (green): (a) first preliminary scan: larger size, low tip load; (b) second scan: removal of molecules A and simultaneous adsorbing of molecules B, applying a high tip load; (c) third scan: acquisition of an image with larger size to estimate the film height difference between molecules B and molecules A.*

These experiments can be performed with two approaches: contact mode, most used, and hard tapping mode. Through the contact mode, tip loads around 100 nN are applied in order to remove the molecules. To reach these force values, a cantilever with k $\sim$ 20 N/m is needed. The contact modality will be presented in detail in the following subsection 2.3.3.
Tapping mode is an AFM modality where the cantilever oscillates near its resonance frequency while scanning, so the tip-sample interaction is temporary and results in a dumping of the cantilever oscillation. As concerns the hard tapping mode, a very small oscillating amplitude, typically 0.01 nm, has to be set with a free oscillation amplitude of $(70 \div 80)$ nm to selectively displace molecules and obtain an exposed gold region. In this case, soft cantilevers with a spring constant as low as 0.06 N/m can be employed.

Imaging: contact mode and QI mode

In contact mode imaging either the z position of the back of the cantilever is kept constant and its deflection is measured (constant height) or the deflection of the lever is kept fixed and the z position needed to keep the deflection constant is measured (constant force). It allows for the study of short-range forces ($\sim (10^{-8} \div 10^{-9})$ N) - intermolecular forces and frictional forces - with high resolution. It is a potentially disruptive technique, especially in the case of easily deformable samples, since drag forces also come into play.
Working at constant force, both the z-polarization signal of the piezoelectric (height image) and the output signal of the photodiode (deflection image) can be acquired. Through the analysis of the z-profiles of height images it is possible to obtain quantitative morphological information on the corrugations of the sample. It is also possible to acquire lateral force images, where the fast scanning axis is orthogonal to the axis of the lever and by analyzing the torsion of the latter it is possible to obtain information on the local tribological properties of the sample surface.
In contact mode, the continuous tip-sample interaction can result in drag forces that can perturb the monolayer, leading to a height underestimation. Therefore, it is important to minimize as much as possible the tip load (around few nN).

In QI mode, introduced above (subsection 2.3.3), the intermittent tip-sample interaction avoids drag effects and results in a less disruptive operation mode. Therefore, a comparative analysis in soft contact and QI modes can increase the reliability of the SAM height estimation.

2.4 X-rays Photoelectron Spectroscopy

X-ray photoelectron spectroscopy (XPS), an electron spectroscopy for chemical analysis (ESCA), is a widely used technique which provides quantitative information on the chemical composition (elements, bonds, quantification) of solid sample surfaces. This method is based on the photoelectric effect, theorized by A. Einstein (Physics Nobel Prize in 1913, "for contributions to theoretical physics, in particular for the discovery of the law of the photoelectric effect") but whose application, through the XPS instrument, was developed by K. M. B. Siegbahn (Physics Nobel Prize in 1981, "for his contribution to the development of high-resolution electron spectroscopy").

2.4.1 Working Principles

When a photon of energy $h\nu$ is absorbed by an atom, an electron can be ejected through several processes, like direct excitations of core electrons, inelastic processes (secondary electrons), Auger electron emissions and direct excitations of valence electrons. The kinetic energy (KE) of the ejected photoelectron depends upon the photon energy ($h\nu$), the binding energy (BE) of the electron (the energy required to remove the electron from the surface) and the work function (Φ).
Focusing on the direct excitation of a core electron, we consider it as a three-step process: (i) the X-ray photon absorption and the atom ionization, (ii) the propagation of the electron in the sample and (iii) the emission of the electron outside the sample. A schematic view of the process is presented in Fig. 2.22.

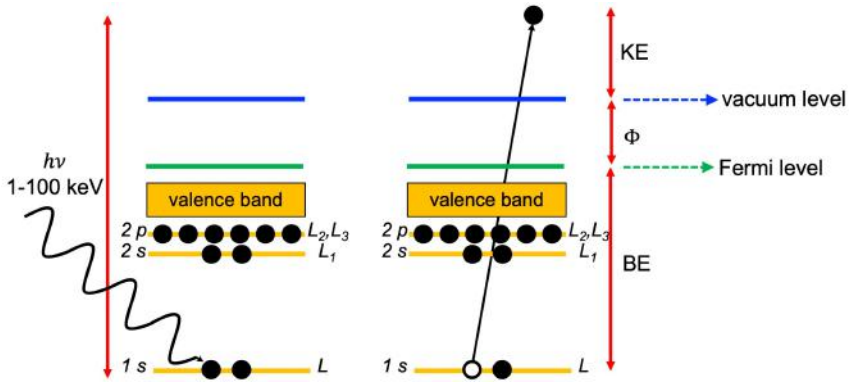

Figure 2.22 – *Representation of the photoemission process: when an atom is irradiated with X-rays, an electron from a core level is ejected with energy $h\nu$.*

By measuring the kinetic energy of the emitted electrons, the binding energy can be obtained through the following equation, since all the other parameters are known

(Φ, $h\nu$):

$$BE = h\nu - KE - \Phi \tag{2.26}$$

A typical XPS spectrum shows the number of photoelectrons versus the binding energy. The energies and intensities of the photoelectron peaks enable identification and quantification of all surface elements (except hydrogen). In fact, the photoelectron binding energy depends on many parameters, like the element from which the electron is emitted (BE), the orbital from which the electron is ejected (BE and peak components) and the chemical environment of the atom from which the electron was emitted (BE shift and peak shape). Therefore, it is possible to determine which elements are present on the material surface and their chemical state.
As mentioned above, an electron can be ejected through processes other than direct interaction with the incident photon, and, therefore, different types of peaks can appear in an XPS spectrum. One of the most important processes to consider is Auger electron emission, which is characterized by lines with complex patterns. When a photoelectron is emitted and a hole is created, the relaxation of the atom (i.e., the decay of a more energetic electron toward the vacant hole) can give rise to another electron emission and photon emission (fluorescence process). For example, the "*O KLL*" peaks represent the electrons ejected from the atom after the filling of the O 1s state (K shell) by an L shell electron coupled to the ejection of an L shell electron. Unlike the photoemission peaks, the kinetic energy of the Auger peaks is independent of the X-ray photon energy $h\nu$: changing the photon energy and plotting the number of photoelectrons versus KE, Auger lines are fixed while photoemission lines move, and it is possible to discriminate between these kinds of peaks.
Secondary electrons are another source of peaks in XPS spectra. These particles are caused by the formation of electron-hole pairs around the Fermi level and/or by plasmonic losses. Secondary electron emission can give an asymmetric shape to the photoemission peaks, while the sharpness of secondary plasmonic peaks depends on the material. Other satellite X-ray peaks may appear using a non-monochromatic source: these secondary structures are within $(30 \div 60)$ eV from the main line and are due to additional X-ray sources than the anode.
Finally, all peaks are immersed in an inelastic background due to energy loss from photoelectrons.

2.4.2 Instrument

As mentioned above, XPS spectra are obtained by irradiating a sample with a beam of soft X-rays while simultaneously measuring the kinetic energy of electrons that are emitted from the surface of the material under investigation.
Firstly, a photoemission experiment has to be carried out in Ultra High Vacuum (UHV) in order to reduce the possible collisions of photoelectrons with particles on their path to the detector. Usually, a rotary pump, a turbo-molecular pump and an ionic pump are employed to reach a final pressure value around $(10^{-9} \div 10^{-11})$ mbar.
X-rays are generated by bombarding an anode material (typically Al or Mg) with

high-energy electrons (15 kV), emitted from a thermal source. The impact of electrons on the anode makes them transfer their energy to the atoms of the material, whose electrons go into an excited state: when de-excitation occurs, there is the emission of photons with specific hν.
To remove satellite peaks and to improve the intrinsic resolution of the X-ray beam, a monochromator is required.
Then X-rays are sent on the sample surface where they induce the emission of photoelectrons. Electrons are collected by electrostatic and/or magnetic lens units, transferred through the apertures and focused onto the analyzer entrance slit. Electrostatic fields within the hemispherical analyzer (HDA) are established to only allow electrons of a given energy (the so called Pass Energy (PE)) to arrive at the exit slits and onto a multichannel electron detector system.

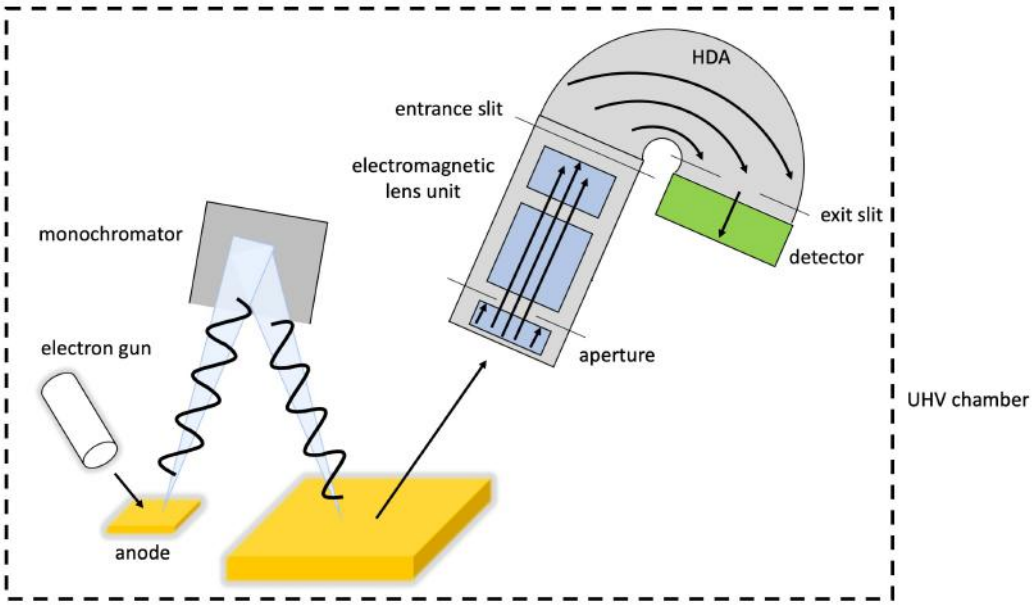

Figure 2.23 – *Scheme of an XPS set-up.*

The energy resolution of the instrument depends on the diameter of the analyser, the pass energy, the spread of energies in the X-ray source and sample-dependent factors. Moreover, in order to obtain a good signal-to-noise ratio, it is often necessary to perform the measurement on the same energy range many times (performing sweeps and cycles), risking damage to the sample due to the prolonged exposure to radiation.

2.4.3 Spectra analysis

In XPS, the nomenclature employed for core levels is nl_j, where n is the principal quantum number, l is the angular momentum quantum number and j is the sum of l and s, where s is the spin angular momentum number and can take as values $\pm\frac{1}{2}$. All orbital levels, except the s levels ($l = 0$), give rise to a doublet with the two possible states having different energies (with a fixed spin orbit splitting, different for each

element).
Another paramount feature of peaks is the intensity (number of counts in the XPS spectra). Considering a single peak, the more intense is the signal, the larger is the number of atoms which emitted those electrons.

Spectra types

In general, at the beginning of the XPS experiment, a survey spectrum is acquired over a broad energy region (around $(1000 \div 1200)$ eV wide), allowing for the identification of the major chemical species present on the sample surface. In fact the detected signal is characterized by different peaks, corresponding to different atom core levels. Survey spectrum is usually followed by the acquisition of high-resolution spectra ($(10 \div 20)$ eV wide), centred on the element peaks of interest. The pass energy, the acquisition time and the energy steps are the main parameters that affect the spectral energy resolution. The chemical bonds and the effect of the environment are detected through the analysis of these spectra.

Chemical quantification: peak intensity

For the quantification of the XPS signal intensity it is necessary to consider that each element (and also each orbital) has a specific atomic cross section for photoionization, called Relative Sensitivity Factor (RSF) or Scofield coefficient [152, 153]. The quantitative evaluation of the intensity of the i-th peak can be obtained through the following equation

$$I_i = N_i \sigma_i \lambda_i D_i \tag{2.27}$$

where I is the intensity, N is the average atomic concentration, σ is the RSF and λ is the inelastic mean free path of a photoelectron and D contains all other factors related to quantitative detection of a signal (for example the detector sensitivity at the specified electron energy).

Chemical identification: peak deconvolution

XPS spectra, especially high-resolution ones, usually need a fitting to perform the peaks deconvolution and correctly assign the components. During the fit procedure, the number of components, their shape, their width and the shape of the background are some of the parameters that should be considered for the peak analysis. Usually, the line shape of a core level can be described by a Lorentzian (L) function:

$$L(x;\gamma) = \frac{1}{\pi} \frac{\gamma}{x^2 + \gamma^2} \tag{2.28}$$

Sometimes more complicated shapes are needed, for example when a broadening due to the instrumental apparatus is observed: in these cases, a Gaussian/Lorentzian shape can be used to better reproduce experimental data. The Gaussian/Lorentzian function is called Voigt [154] and is reported in equation 2.29

$$V(x,\sigma,\gamma) = \int_{-\infty}^{\infty} G(x',\sigma), L(x-x',\sigma) dx' \tag{2.29}$$

where $G(x;\sigma) = \frac{1}{\sigma\sqrt{2\pi}} e^{-\frac{x^2}{2\sigma^2}}$ is the Gaussian contribute and $L(x;\gamma)$ is the Lorentzian one (Eq. 2.28). Depending on the acquisition system, the ratio of Gaussian to Lorentzian contributions can be modified but in any case the shape of the Voigt function maintains its symmetry.
Metal spectra exhibit a natural asymmetry extending to the high-binding-energy side, therefore the simple Voigt profile is not satisfying. In order to account for the asymmetric metal photoemission, the Doniach-Sunjic peak shape [155] can be employed.
Finally, in a XPS spectrum it is crucial to consider the background signal due to photoelectron and Auger electrons which have undergone several inelastic loss processes during their way through the material. In particular, for an accurate analysis it is very important to evaluate the background intensity and subtract it from the total intensity. In general, background signal analysis is limited to the energy range of the considered peaks. The linear background is the most simple background shape used when there is a relatively small change in the background over the peak energy range and can be expressed by the following equation

$$L(E) = I_1 \frac{E_2 - E}{E_2 - E_1} + I_2 \frac{E - E_1}{E_2 - E_1}. \tag{2.30}$$

2.5 Quartz Crystal Microbalance with Dissipation

The quartz crystal microbalance (QCM) is a surface sensitive, real-time method that detect mass changes at the sensor surface with nano-scale resolution. In particular, the quartz crystal microbalance with dissipation monitoring (QCM-D) technology is able to measure, in addition to the frequency (related to the mass), the dissipation of a freely oscillating quartz crystal after excitation. Therefore, the applications of QCM-D are various and particularly efficient for biosensing [156], since this method can provide information about mass variation per unit area, kinetic, conformational changes and viscoelastic properties, allowing for the study the adsorption/desorption of small molecules on the surface of the piezoelectric crystal.
QCM-D experiments can be performed in vacuum, in gas phase and in liquid, allowing for mass sensitivity down to $(0.1 \div 1)\mu g/cm^2$ and quick measurements.

2.5.1 Working Principles

The working principle of a QCM is quite simple. Through electrodes deposited on each side, a voltage is applied and can excite a piezoelectric material (a thin quartz crystal disk), which relates electrical deformations to mechanical changes and vice versa. The crystal resonance frequency is related to the thickness (mass) of the disk: if the thickness changes, so will the resonance frequency. Therefore, by monitoring changes of the resonance frequency Δf, it is possible to detect nano-scale changes of the crystal mass/thickness.

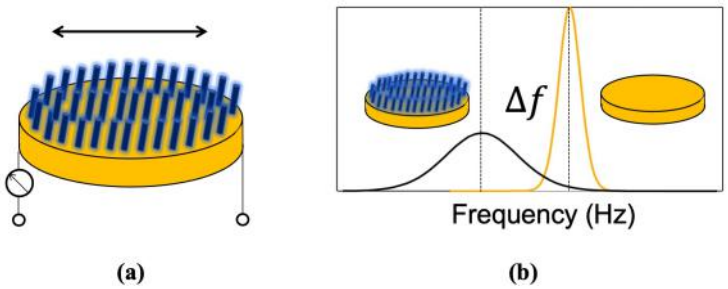

Figure 2.24 – *Representation of the QCM working principle: a change of the resonator thickness/mass cause a shift of the frequency oscillation.*

A QCM is a harmonic oscillator, therefore if it is not forced to oscillate by an external force it will gradually oscillate with lower and lower amplitude (damping) due to frictional losses, such as internal friction in the oscillator itself or frictional losses in the surrounding medium (air, water, etc.). Energy loss due to friction manifests itself as heat dissipation. In the case of QCM, the energy losses are mainly induced by the materials in contact with the oscillating sensor surface.
During the oscillation, liquids and soft or thick films which are in contact with the surface will be deformed and will cause energy losses while, when the sensor surface is in contact with air or vacuum or with thin and rigid layers, the induced energy losses are comparatively smaller. Consequently, high dissipation indicates the presence of a soft or viscous material while low dissipation indicates that the material on the surface is quite rigid. The capability of a molecular deposited film to cause high or low energy losses depends also on the water content of the film. Therefore, dissipation can provide also structural information related to conformational changes within the film.
QCM measures the dissipation value D as the sum of all energy losses in the system per oscillation cycle:

$$D = \frac{1}{Q} = \frac{1}{2\pi} \frac{energy\ lost\ per\ cycle}{energy\ stored} \tag{2.31}$$

Dissipation is the inverse of the quality factor Q, a dimensionless parameter that describes the damping of the oscillation at resonance, by relating the amount of energy stored to the amount of energy lost. The higher the Q factor the lower the damping and the longer the oscillation will keep on going. The Q factor, which is the ratio of frequency and bandwidth, can be as high as 10^6: such a narrow resonance leads to highly stable oscillators and a high accuracy in the determination of the resonance frequency.

Measuring dissipation allows to determine whether the Sauerbrey model, applicable only for rigid film, is valid. The Sauerbrey equation [157, 158] can be used for the quantification of the adsorbed mass, which is calculated as a function of sensor properties as follows:

$$\frac{\Delta m}{A} = -C\frac{\Delta f}{n} \tag{2.32}$$

where $\frac{\Delta m}{A}$ is the adsorbed mass per unit area on the sensor, C is the coefficient that describes the sensitivity of the instrument, Δf is the shift in frequency and n is the overtone number. Common equipment allows for a resolution down to 1 Hz on crystals with a fundamental resonant frequency in the $(4 \div 6)$ MHz range.

2.5.2 Instrument

The core of a QCM set-up is the quartz crystal resonator. The resonance frequency of acoustic resonators depends on temperature, pressure, and bending stress, therefore a careful control of temperature is essential in the operation of the QCM.
Resonators can be operated at a number of overtones, typically indexed by the number of nodal planes parallel to the crystal surfaces. Just the odd harmonics are excited since they are the only ones that induce charges of opposite sign at the two surfaces of the crystal. The lowest resonance frequency, n=1, is called the fundamental while n=3, 5, 7 etc. are overtones to the fundamental (e.g., when the fundamental frequency is 5 MHz, the overtone resonances would be 15 MHz, 25 MHz, 35 MHz etc).
A typical set-up for the QCM contains also the oscillation source (electronic controller) and a measuring and recording device (electronic analyzer).

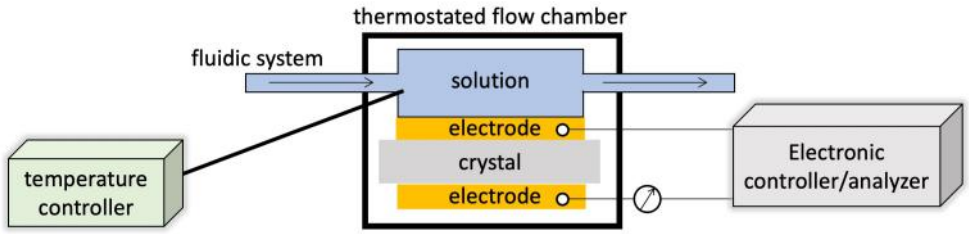

Figure 2.25 – *Scheme of a QCM-D set-up.*

Chapter 3

Materials and methods

In this chapter materials and experimental protocols employed for sample preparation and characterization will be presented.
After a comparison between the different substrates used for the experiments, SAM preparation protocols will be presented as well as molecules employed.
As concerns the methods, experimental set-up and measurement protocols will be described in detail.

3.1 Materials

3.1.1 Substrates

Different experimental techniques have required different substrates, due to specific requirements like geometric issues (SE), low roughness (AFM), method-specific requirements (QCM-D) or gold layer thickness (SPEE).

Figure 3.1 – *Substrates employed in this thesis. From left to right, substrates for experiments: (1) SE/XPS: Au (250 nm) on borosilicate glass slides (with a Cr primer layer), RMS (2 μm^2)=1.7 nm; (2) AFM: Au (100-200 nm) on silicon wafer, RMS (2 μm^2)=0.3 nm; (3) QCM-D: Au on quartz sensor, RMS (2 μm^2)=1.1 nm; (4) SPEE: Au (50 nm) on borosilicate glass slides (with a Ti primer layer), RMS (2 μm^2)=1.5 nm.*

SE and XPS substrates

Flat gold substrates purchased from *Arrandee* were used for SE and XPS measurements. Arrandee substrates are prepared by evaporation of (250±50) nm gold on borosilicate glass slides previously covered with a $(1 \div 4)$ nm Cr primer layer. These samples show a RMS roughness (Sq) of 1.7 nm on a 2 μm^2 area (Fig. 3.3 (a)).
Arrandee substrates were cleaned with acid piranha solution (4:1 H_2SO_4, 30% H_2O_2)

for 3 minutes, thoroughly rinsed with Milli-Q water and dried under a nitrogen stream. The piranha process can be repeated at least until five times.

AFM substrates

Ultra-flat gold substrates, prepared according to Gupta et al. [159] (often called Ulman-type gold), were used for AFM measurements. A low roughness substrate is required to study organic films with a thickness of few nanometres. These samples show a RMS roughness (Sq) of 0.3 nm on a 2 μm^2 area (Fig. 3.3 (b)).
To prepare Ulman-type gold, Si (100) polished wafers of 279 μm thickness were washed in ultrasonic bath in acetone (15 min) and then ethanol (15 min). Then, 100-200 nm of gold was evaporated on the Si substrate, with an evaporation rate around 0.5 nm/s (Fig. 3.2 (a)). Finally, about 1 cm^2 Si pieces (previously cleaned with the procedure reported above) (Fig. 3.2 (b)) were glued on the gold layer with a drop of SU8-2025 resist (*MicroChem*) applying a slight manual pressure (Fig. 3.2 (c)) and annealed according to the following protocol:

- 2 h, 60°C;
- 3 h, 90°C;
- overnight, 120°C.

Before use, the capping silicon wafer is removed by a cutter and a clean gold surface is obtained (Fig. 3.2 (d)). Therefore, no cleaning procedure is necessary for ultra-flat gold substrates since the Si slide is removed from the gold surface immediately prior to use.

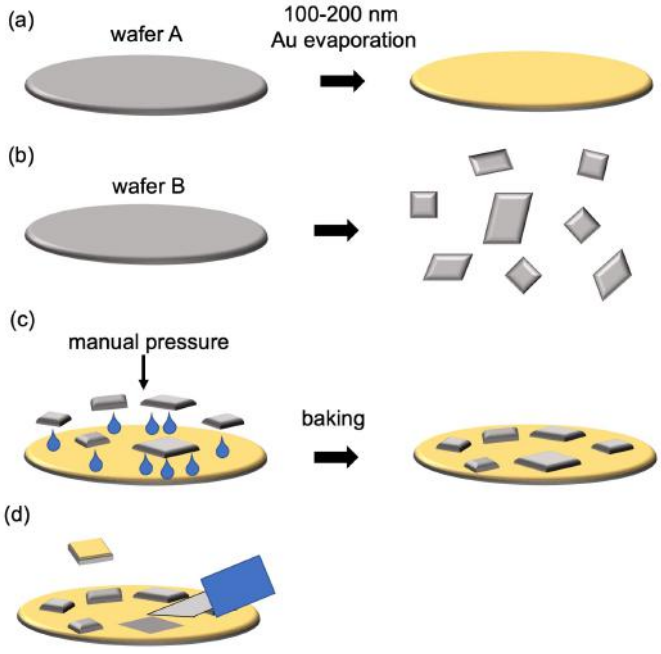

Figure 3.2 – *Scheme of Ulman-type gold substrates preparation.*

QCM-D sensors

Gold-coated quartz sensors (*Biolin Scientific*) with a resonance frequency of 5 MHz were used for QCM-D measurements. These samples show a RMS roughness (Sq) of 1.1 nm on a 2 μm^2 area (Fig. 3.3 (c)).
QCM-D sensors were cleaned with basic piranha solution (1:1:5 30% ammonia solution, 30% H_2O_2, Milli-Q water) for 5 minutes at 75°C, thoroughly rinsed with Milli-Q water and dried under a nitrogen stream.

SPEE substrates

Gold coated borosilicate glass slides, with a 3 nm titanium adhesion layer, purchased from *Phasis* were used for SPEE experiments. SPEE substrates have been chosen with a gold layer thickness of 50 nm to fulfil the SPR requirements, allowing for the propagation of the evanescent wave through the metal layer. These samples show a RMS roughness (Sq) of 1.5 nm on a 2 μm^2 area (Fig. 3.3 (d)).
SPEE substrates were cleaned with acid piranha solution (4:1 H_2SO_4, 30% H_2O_2) for 3 minutes, thoroughly rinsed with Milli-Q water and dried under a nitrogen stream.

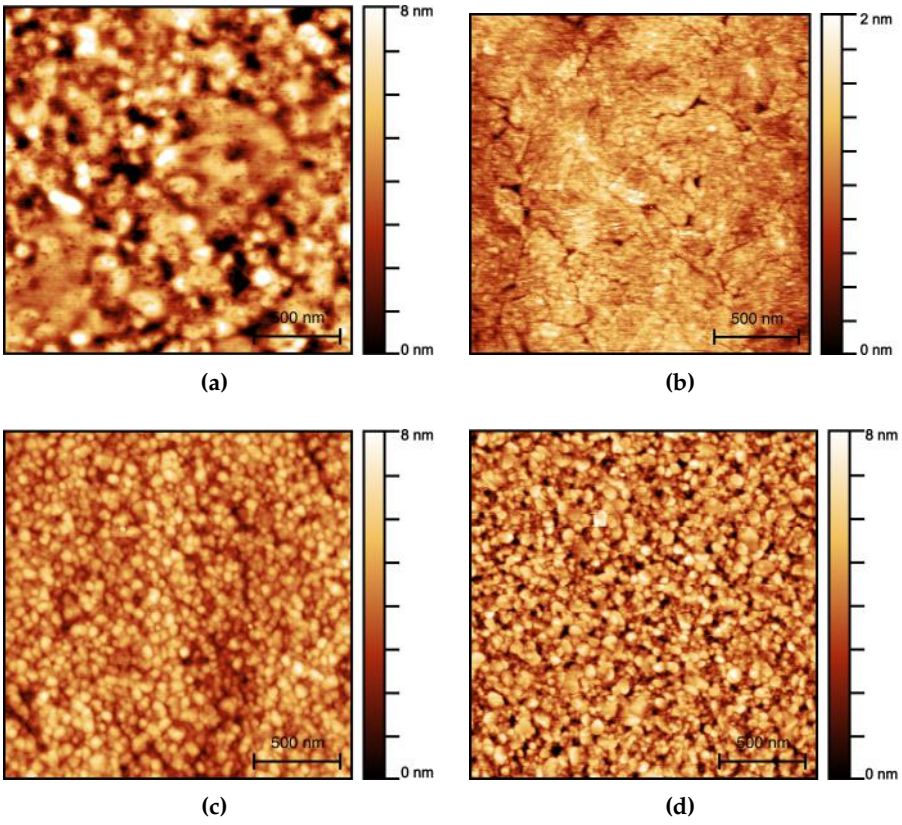

Figure 3.3 – *AFM images of the gold substrates used in this thesis work. a) SE, XPS substrates, b) AFM substrates, c) QCM sensors, d) SPEE substrates.*

3.1.2 Reagents

Tris[hydroxymethyl]amino-methane (Tris base) (>99.9%), ethylenediamine-tetraacetic acid (EDTA) (99.7%), 30% ammonia solution (28.0 ÷ 30.0%) and sodium hydroxide (NaOH) (≥97%) were purchased from Sigma Aldrich. Sodium chloride (NaCl) (≥99.5%) was purchased from Merck. Hydrochloric acid (HCl) (≥32%) was purchased from Fluka. Sulphuric acid (H_2SO_4) (96.1%) and 30% hydrogen peroxide (H_2O_2) (29.0 ÷ 31.0%) were purchased from Carlo Erba. Aqueous solutions were prepared with ultra-pure deionized water (resistivity ≥ 18 MΩ·cm) from a Millipore Milli-Q system.
Experiments were performed using TE buffer (10 mM Tris, 1 mM EDTA and NaCl, pH adjusted at 7.2 using HCl). Two NaCl concentrations were used, 1 mM NaCl (1 mM NaCl TE) and 1 M NaCl (1 M NaCl TE). The two salt concentrations (1 mM and 1 M) were chosen as extreme values to evaluate the effect of salt on the preparation of the DNA SAMs.

3.1.3 Self-Assembled Monolayers

Oligonucleotides and alkylthiols

HPLC purified oligonucleotides were purchased from *biomers.net* (Germany) and used as received. Labelled oligonucleotides were coupled with the Atto590 dye, a rhodamine dye with $\lambda_{abs} = 593$ nm and $\lambda_{fl} = 622$ nm.
FZ24 sequence (22-mer) has been used as "training" sequence to understand the behaviour of DNA SAMs and optimize the experimental protocols (Fig. 3.4 (a)).
RNA-dependent RNA polymerase (RdRp) Helicase sequence (28-mer) belongs to a SARS-CoV-2 gene region [160, 161] (Fig. 3.4 (b)). This DNA sequence has been chosen to prove the efficacy of our experimental approach to detect nucleic acid strands for biosensing applications.

It is useful to define a common nomenclature for all the sequences. The term "probe" DNA (pDNA) refers to the thiolated strand, immobilized on the gold substrate, whose sequence is complementary to the "target" chain (tDNA or tRNA), i.e. the sequence to be detected. Instead, we refer to "single-strand" DNA (ssDNA) or "double-strand" DNA (dsDNA) when we want to highlight the conformation of the DNA rather than its sequence.

6-Mercapto-1-hexanol (HS-$(CH_2)_6$-OH, MCH) was purchased from Sigma Aldrich.

HS-pFZ24	HS-$(CH_2)_6$-5′-TAATCGGCTCATACTCTGACTG-3′
tFZ24	5′-CAGTCAGAGTATGAGCCGATTA-3′
tFZ24*	5′-CAGTCAGAGTATGAGCCGATTA-3′-Atto590
$(dA)_{22}$	5′-AAAAAAAAAAAAAAAAAAAAAA-3′
$(dA)_{22}$*	5′-AAAAAAAAAAAAAAAAAAAAAA-3′-Atto590
HS-pRdRp	HS-$(CH_2)_6$-5′-AATTCTACACCACGAACGTATGCATCTG-3′
tRdRp DNA	5′-CAGATGCATACGTTCGTGGTGTAGAATT-3′
tRdRp RNA	5′-CAGAUGCAUACGUUCGUGGUGUAGAAUU-3′

Table 3.1 – *Nucleic acid sequences.*

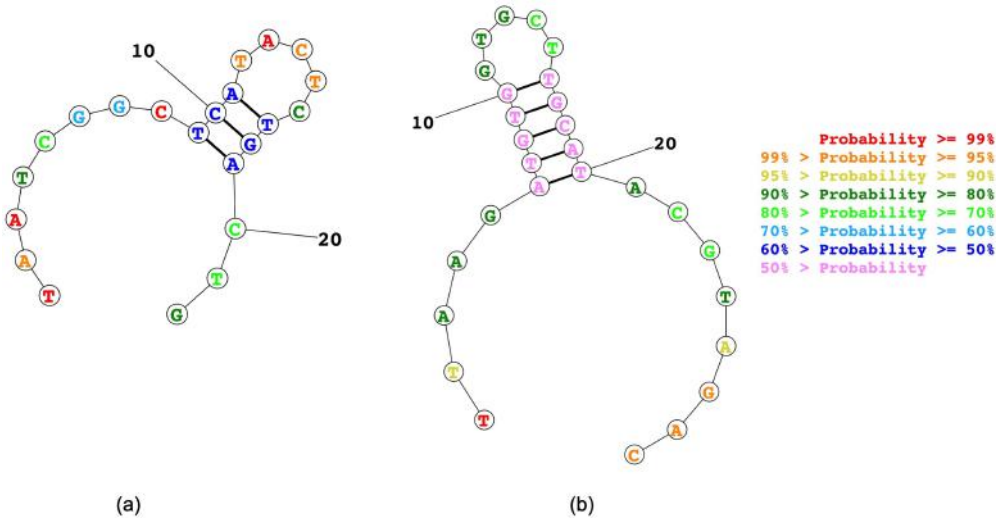

Figure 3.4 – *Secondary structures of DNA/RNA sequences employed in this thesis work, calculated through http://rna.urmc.rochester.edu/RNAstructureWeb/Servers/Predict1/Predict1.html and confirmed also by Nupack software http://nupack.org/partition/new. (a) FZ24 (pDNA, HS-pFZ24) and (b) RdRp-Helicase (pDNA, HS-pRdRp).*

SAMs preparation

DNA films were prepared following a 3-step preparation protocol.
pDNA self-assembly was carried out by keeping the clean gold substrates in 1 μM probe DNA solution in TE buffer at ambient temperature (Fig. 3.5 (a)). Two pDNA incubation times were used, 3 hours and 24 hours, in order to evaluate how the thiolated strand film density influences the hybridization process.
To improve film organization, samples were then immersed in 5 μM MCH solution in TE buffer (ambient temperature, 1 hour) [104, 111, 162–164] (Fig. 3.5 (b)). The incubation time of 1 hour was chosen starting from literature (Gong et al., [165]), where different 11-Mercapto-1-undecanol (MCU) incubation times were studied in order to improve hybridization efficiency. It is worth noting that the linker of pDNA has the same chain length of the spacer MCH molecule.

Hybridization was performed by exposing the mixed SAMs to the target sequence (1 μM tDNA or tRNA in TE buffer) for at least 20 minutes at ambient temperature (Fig. 3.5 (c)). This process was tested employing also labelled target strands (1 μM tDNA*) for the validation of the process, not-target strands (1 μM n-tDNA or n-tDNA*; in particular, we employed $(dA)_{22}$ and $(dA)_{22}$*) for the selectivity test and through denaturation/hybridization cycles to test the recovery of the platforms. Chemical denaturation was performed exposing the dsDNA/MCH film to a 1 M NaOH solution for $(5 \div 10)$ minutes and then thoroughly rinsing with TE buffer. NaOH, by increasing the pH, makes OH- groups predominant: by removing the hydrogen-bonds-contributing protons from guanine and thymine, OH- groups break the hydrogen bonds between the two oligonucleotides [80].

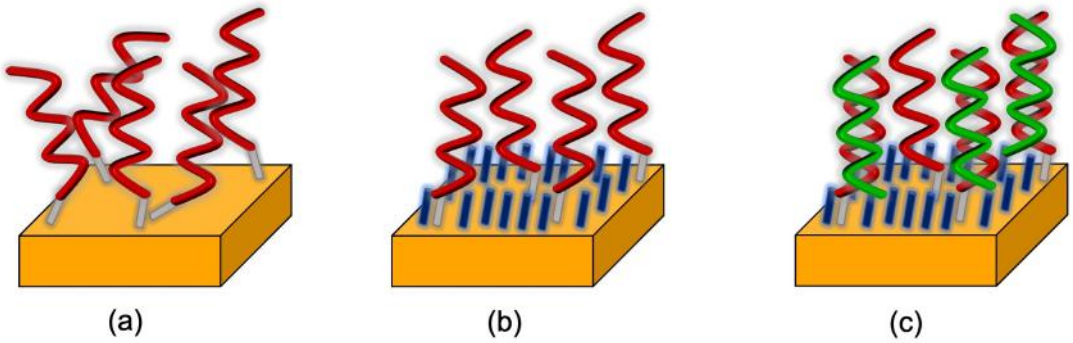

Figure 3.5 – *Scheme of the 3-step protocol for DNA SAMs preparation: (a) pDNA film; (b) pDNA/MCH (mixed) film; (c) dsDNA/MCH film.*

3.2 Methods

3.2.1 Atomic force microscopy

AFM experiments were carried out using a JPK NanoWizard IV microscope (*Bruker*) (Fig. 3.6). Gold-coated Si cantilevers (DNP-S10, *Bruker*) (Fig. 3.7 (a)) with a spring constant of 0.24 N/m and a nominal tip radius of curvature of 10 nm were used for imaging in QI and contact mode and for hard tapping shaving operation mode. Contact shaving and air tapping imaging experiments were conducted using aluminium-coated Si cantilevers (OMCL-AC160TS-R3,*Olympus*) (Fig. 3.7 (b)) with a spring constant of 26 N/m and a nominal tip radius of curvature of 7 nm.

Figure 3.6 – *JPK NanoWizard IV AFM (Bruker)*

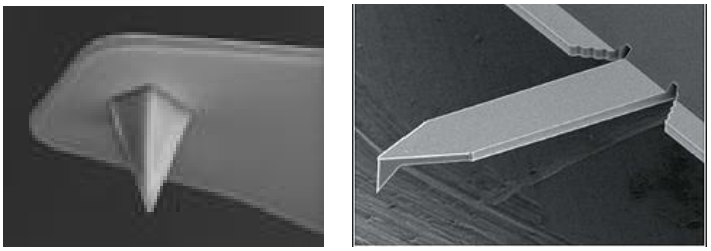

(a) **(b)**

Figure 3.7 – *AFM tips: (a) DNP-S10, Bruker; (b) OMCL-AC160TS-R3,Olympus.*

Nanoshaving experiments were performed by scanning a selected area (typically a few μm wide) in hard tapping mode (setting a very small oscillating amplitude, typically 0.01 nm, with a free oscillation amplitude of $(70 \div 80)$ nm) or in hard contact mode (applying a load force of hundreds of nN) to selectively displace molecules and obtain an exposed gold region. The frequency scan rate was set to $(1 \div 2)$ Hz. After shaving, an image with larger scan size was acquired in soft contact (few nN) or QI mode. The frequency scan rate was set to 0.5 Hz.
Data have been analyzed with Gwyddion (v2.55) and JPKSPM Data Processing software.
DNA films were analyzed in situ in TE buffer, while bare gold substrates were analyzed in air.

3.2.2 Spectroscopic ellipsometry

SE measurements were performed with M-2000 ellipsometer, *J.A. Woollam Co.*, $(245\ div1700)$ nm, equipped with a 75 W Xe lamp.
The M-2000 ellipsometer is a rotating compensator ellipsometer (RCE), with a fixed analyser and a compensator as rotating optical element, which converts a linear polarization in a circular polarization (Fig. 2.3). The RCE configuration assures

accurate measurement of Ψ and Δ on the whole measured range [166]. In the M2000 ellipsometer the reflected light impinges on a fixed grating into a CCD array: in this way, each channel of the array collects one wavelength and it is possible to acquire all the wavelengths together.

In situ measurements and liquid cells

In situ experiments were conducted using a commercial liquid cell (J.A. Woollam Co., 0.5 mL).

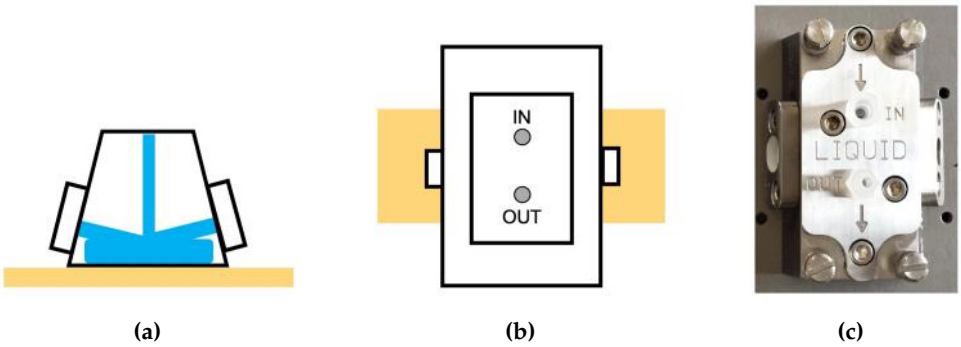

Figure 3.8 – *Woollam liquid cell for SE in situ measurements. (a) Sketch of front side cell. (b) Sketch of top side cell. (c) Top view of the cell.*

The required volume to fill the cell is around 0.5 mL but, in order to completely replace the inner solution, a volume of $\sim (2 \div 2.5) mL$ is used. How can be seen from Figure 3.9, the solution passes through a 0.22 μm filter, employed at the inlet tubing entrance, in order to avoid micro-bubble formation. Moreover, a stabilizing system is added to mechanically decouple the filter and the cell.
The cleaning of the Woollam cell requires to disassemble the cell. Steel pieces and Viton o-rings were washed in ultrasonic bath 3 times in Milli-Q water and 1 time in ethanol, while UV-grade fuse silica windows were firstly immersed in NoChromix solution (*SigmaAldrich*) for 15 minutes and then washed in ultrasonic bath 3 times in Milli-Q water.

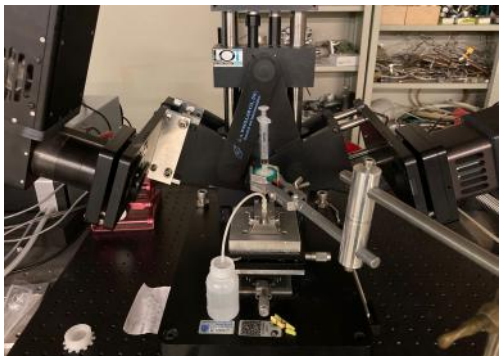

Figure 3.9 – *Set-up for in situ SE experiments using Woollam liquid cell.*

Dynamic measurements

The M2000 ellipsometer allows for the real-time following of the molecular deposition, through dynamic measurements acquired over the whole probed spectral range with user-defined time steps. In our experiments, dynamic measurements were collected in order to monitor the effects of exposing the sample to the different solutions (pDNA, MCH and tDNA solutions). During these measurements, the signal has been sampled every 7 s for pDNA (50 revolutions) and every 3.5 s (15 revolutions) for MCH and tDNA solution.

Difference spectra

As already described in section 2.1.4, in order to emphasize the contribution of the ultrathin organic layer we analyzed static difference spectra, obtained as the difference between the spectra acquired after the film deposition (Ψ_i,Δ_i) and the spectra measured on the bare substrate just prior to molecular deposition (Ψ_0,Δ_0) [8, 18, 121]. Difference spectra related to the different deposition steps are referred to as follows:

1. after pDNA deposition: $\delta_{1/0}(\Psi,\Delta) = (\Psi_1,\Delta_1) - (\Psi_0,\Delta_0)$;
2. after addition of MCH: $\delta_{2/0}(\Psi,\Delta) = (\Psi_2,\Delta_2) - (\Psi_0,\Delta_0)$;
3. after hybridization with tDNA: $\delta_{3t/0}(\Psi,\Delta) = (\Psi_{3t},\Delta_{3t}) - (\Psi_0,\Delta_0)$;
4. after incubation in n-tDNA: $\delta_{3n/0}(\Psi,\Delta) = (\Psi_{3n},\Delta_{3n}) - (\Psi_0,\Delta_0)$.

In this thesis work we also consider difference spectra between two subsequent steps, for example between mixed (pDNA + MCH) and hybridized films (pDNA + MCH + tDNA): $\delta_{3t/2}(\Psi,\Delta) = (\Psi_{3t},\Delta_{3t}) - (\Psi_2,\Delta_2)$.

SE measurement protocol

The measurement SE protocol was the following:

1. static reference ex situ: characterization of gold substrate in air (100 revolutions);
2. static reference in situ: characterization of gold substrate in TE buffer (average of 10 measurements) (250 revolutions);
3. dynamic characterization of film formation in the molecular solution (either pDNA, MCH or tDNA solution);
4. static characterization of the film in situ: substitution of incubation solution with TE buffer and characterization of SAM (this spectrum is used to calculate difference spectra with the static reference acquired in step I) (average of 10 measurements) (250 revolutions);
5. repetition of steps III and IV for each following molecular deposition;

6. sample dried under air flux ("Ultra Pure Duster", *Techspray*) and static characterization of the film at the final stage ex situ (100 revolutions).

3.2.3 Surface plasmon enhanced ellipsometry

SPEE experiments were performed using the W-VASE, *J.A. Woollam Co.* ellipsometer (spectral range: $(190 \div 1700)$ nm).
The W-VASE ellipsometer is a wide spectral range (UV-Vis-NIR) variable angle spectroscopic ellipsometer, which exploits the rotating analyzer configuration (rotating analyzer ellipsometer, RAE). In particular, the ellipsometer contains an input linear polarizer and a rotating output analyzer, which allows for the change of the unknown polarized light coming from the sample in a linear polarized light. Furthermore, a monochromator allows for the selection of the wavelength of the input light source, in order to perform a spectroscopic analysis where only one wavelength at a time passes impinges on the sample. Another interesting characteristic is the small size of the light beam, which is of the order of some tenths of millimetre (definitely smaller than M2000 beam size), avoiding depolarization effects due to non homogeneity.
The scheme of the experimental set-up is represented in Figure 3.10.

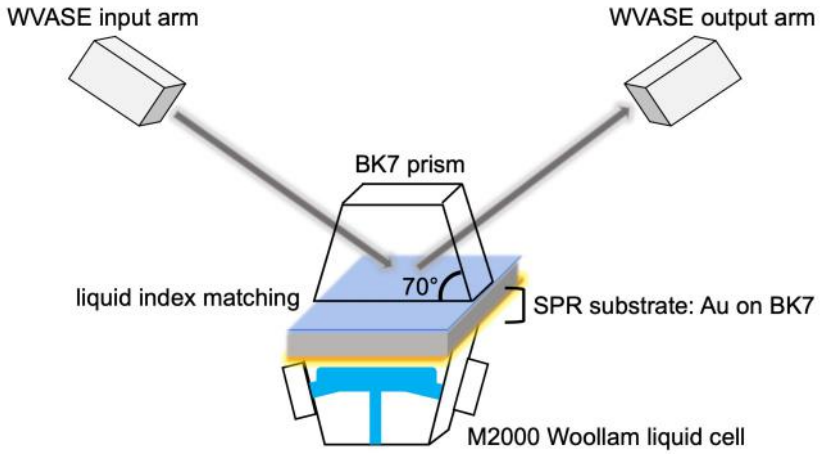

Figure 3.10 – *Scheme of the set-up for in situ SPEE experiments using the Woollam liquid cell.*

The experimental set-up was home-made with the kind help of Dr. Francesco Bisio. In Figure 3.11, a detail of the sample-prism coupling system is reported, while in Figure 3.12 the complete SPEE set-up, mounted on the W-VASE ellipsometer, is reported.

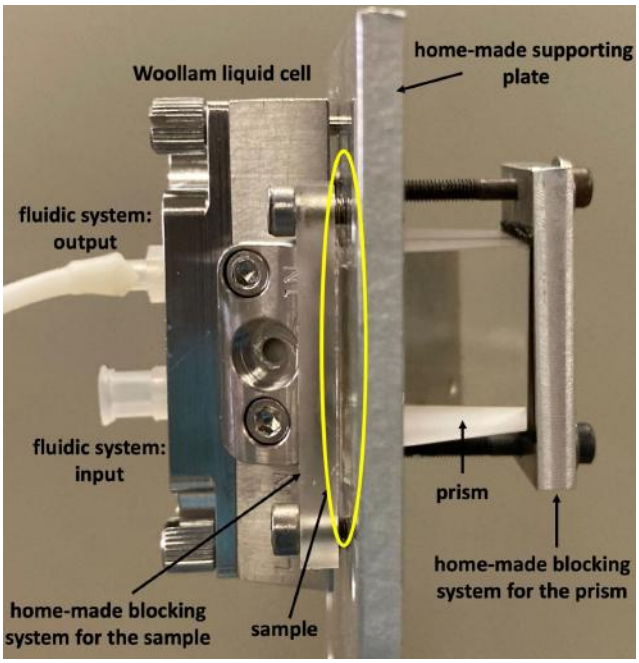

Figure 3.11 – *SPEE set-up: focus on the blocking system of the sample.*

(a) **(b)**

Figure 3.12 – *Set-up for in situ SPEE experiments using the Woollam liquid cell and the W-VASE ellipsometer.*

3.2.4 X-rays Photoelectron Spectroscopy

After SE measurements, samples were characterized by using a PHI 5600 Multi-Technique apparatus, with an X-ray Al-monochromatized source ($h\nu$=1486.6 eV). The photoelectron take-off angle was set to 45 degrees. Survey spectra were acquired using a pass-energy of 187.85 eV, while high resolution spectra were acquired with a pass-energy of 23.5 eV. For each sample, at least three regions were analyzed to check for sample uniformity.
XPS spectra were analysed with Casa-XPS software. A linear background was subtracted from raw data. For the $Au4f_{7/2}$ signal, a Gaussian-Lorentzian asymmetric line shape was used to model the asymmetric metallic behaviour. For the other elements, Voigt functions (30% Gaussian) were used for signal deconvolution. Spin-orbit split-

ting values used for deconvolution were: 3.7 eV for Au4f, 0.86 eV for P2p and 1.16 eV for S2p. The binding energy scale was calibrated by setting the $Au4f_{7/2}$ peak at 84.0 eV.

(a) **(b)**

Figure 3.13 – *XPS experimental set-up.*

3.2.5 Quartz-Crystal Microbalance with Dissipation

QCM-D measurements were performed with a QCM-Z500 (*KSV*) microbalance equipped with a thermostated flow chamber.
TE buffer (or molecular solution) was injected into the thermostated pre-chamber (2 ml) and let to equilibrate at 22° C for at least 10 minutes. When fundamental and overtone (3, 5, 7, 9, 11) signals were stable, the solution (about 0.5 ml) was injected into the chamber carefully avoiding micro-bubble formation (for this reason, buffer was degassed before use and a 0.22 μm filter was employed at the inlet tubing entrance). The responses at fundamental and higher overtones were simultaneously monitored during molecular self-assembly and recorded every 1 s during all experiments. In this work, only mass/area and dissipation changes calculated from the 7th normalized frequency are presented.

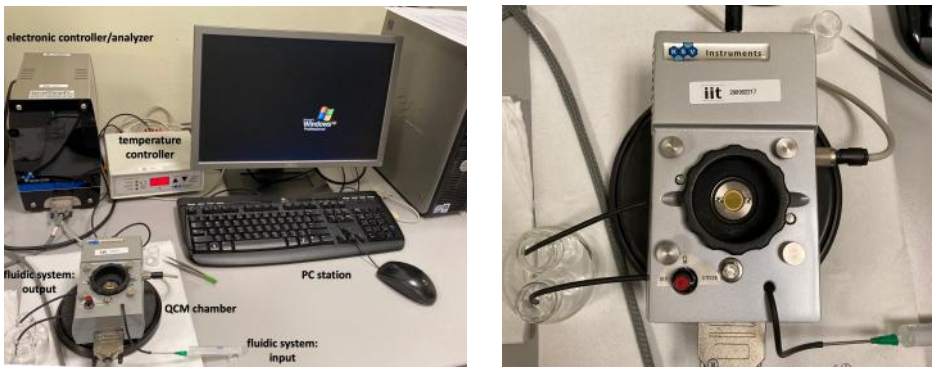

(a) **(b)**

Figure 3.14 – *Set-up for QCM experiment: (a) the whole set-up; (b) focus on the QCM chamber.*

Chapter 4

Results

This chapter will focus on the investigation of the self-assembly of the DNA single-strand films and their hybridization with complementary strands.
We investigated the self-assembly of thiolated single-strand DNA filaments (probe strands) on flat gold analyzing the influence of different parameters, like the ionic strength of the buffer solution and the immobilization time of the single-strand DNA. The optimization of the film deposition protocol continued by analyzing the effect of adding a molecular spacer on the single-strand DNA film; we firstly investigated the deposition of the spacer molecule (mercaptohexanol, MCH) on gold and then we analysed mixed MCH/DNA films studying the effect of the spacer molecule concentration on the pre-formed DNA film.
Finally, a detailed study on the hybridization process was conducted. By monitoring the DNA absorption at 260 nm and the increase of the optical thickness, we could monitor the hybridization process with complementary target DNA strands (tDNA). SE results on DNA films before and after hybridization were supported by the detection of variations in film coverage (QCM-D, XPS) and thickness (AFM nanolithography).
In addition, we studied the sensitivity of the experimental method to detect tDNA (by performing measurements with different tDNA concentrations), the selectivity of the recognition process (using non-complementary strands) and the reversibility of hybridization through cycles of denaturation/hybridization. This analysis is mainly based on the results reported in a paper in submission.
After the complete characterization of the self-assembly of a model single-strand DNA sequence and its hybridization, we focused on the study of SARS-CoV-2 RdRp-Helicase strands, an interesting system for the development of a biosensing platform for the detection of SARS-CoV-2. Developing sensitive devices capable of detecting specific nucleic acid sequences is indeed critical in many different fields, such as life sciences, environmental monitoring, biotechnology and, perhaps most importantly, healthcare. DNA-based biosensors are an excellent option in biosensing due to the high specificity of the binding between complementary DNA strands and to the denaturation property which allows the design of reusable sensing platforms. Considering that an accurate optical SE model allows for the optical characterization

of ssDNA and dsDNA films, we exploit SE as a new sensitive and cheap tool for nucleic acid sequence recognition.
For an easier understanding of the results, I will first give an overall description of the whole system, presenting the complete experiment (pDNA + MCH + tDNA) conducted with the optimized experimental protocols. Then, all the preliminary studies related to the optimization of the experimental protocols and the sensor properties (sensitivity, selectivity, re-usability) will be described.
The study has been conducted mainly through SE, a powerful method which provides information about optical and geometrical properties of the system through an in-situ and real-time analysis [8, 120]. SE detects changes in the optical thickness, quantity depending on both film thickness and film refractive index. SE experiments have been complemented by QCM-D, to obtain information about mass coverage and kinetics and to obtain a valuable liaison to those research works which use mass change detection as the primary method to detect recognition [167–171]. We also performed AFM in-situ measurements to estimate film thickness [9, 18] through the nanoshaving method. Following previous works [172–174], the spectroscopic analysis was extended through ex-situ XPS experiments, dedicated to adding chemical-specific information regarding the DNA-gold bond and the related MCH- and tDNA-induced modifications. Finally, SPEE preliminary experiments have been conducted to increase the sensitivity of the SE detection method.

4.1 dsDNA films

In this section, results related to DNA films prepared through the optimized protocol will be presented. The protocol includes:

- high ionic strength conditions (1 M NaCl TE buffer);
- 3 hour pDNA immobilization time;
- solution concentration: 1 μM for pDNA and tDNA, 5 μM for MCH.

4.1.1 Mass coverage and dissipation: QCM-D

As a first step to study the self-assembly of the thiolated pDNA, the adsorption of MCH molecules and the hybridization with the target sequence, we monitored the process in real-time by QCM-D experiments. In Figure 4.1 we report the time evolution of dissipation (a) and frequency (b) following each molecular deposition step.

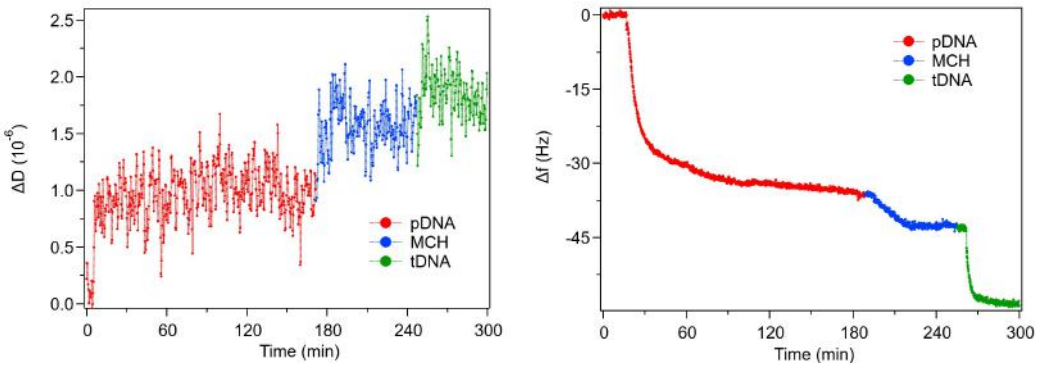

(a) **(b)**

Figure 4.1 – *dsDNA/MCH film self-assembly: pDNA + MCH + tDNA. QCM-D experiment: (a) dissipation and (b) frequency variation versus time.*

Changes in dissipation can be detected at each deposition step (Fig. 4.1 (a)): these variations are quite small, as typically observed for ultra thin organic layers [175]. Dissipation increases after each incubation step, as expected due to the deposition of the molecular layer. The increase of dissipation following MCH exposure can be ascribed to a reorientation of the probe DNA strands which likely result more exposed to the solution when MCH fills the empty binding sites on the gold surface. After hybridization, the increase of dissipation is quite small possibly due to the competing effects of increased layer thickness and higher rigidity of dsDNA compared to ssDNA. The overall dissipation values are however quite small and therefore justify the use of the Sauerbrey equation [157] to convert resonance frequency changes into adsorbed mass (Fig. 4.2).

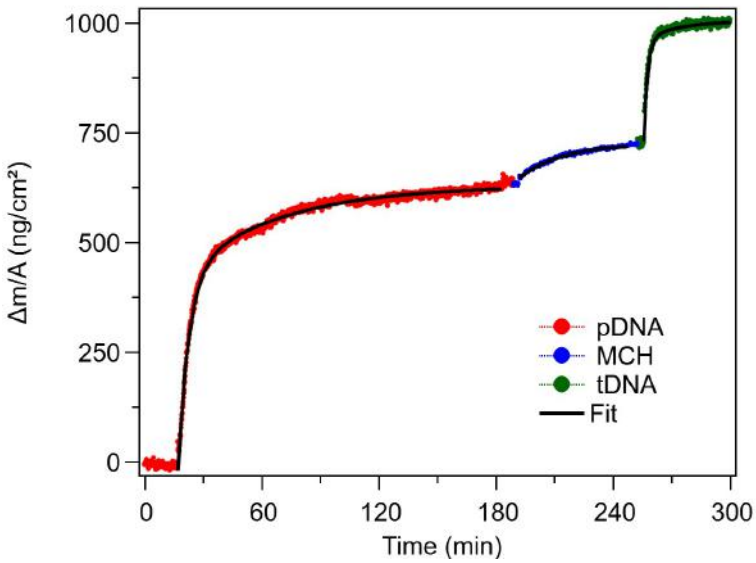

Figure 4.2 – *dsDNA/MCH film self-assembly: pDNA + MCH + tDNA. QCM-D experiment: mass/area ratio variation versus time.*

Focusing on the self-assembly of probe DNA, an average mass increase of 600 ng/cm^2

is detected. Taking into account the molecular mass of pDNA, a molecular density of $5.3 \cdot 10^{13}$ molec/cm^2 is obtained, in agreement with surface coverages reported in previous electrochemical [106, 176, 177], optical [165] and XPS [172, 173, 178] studies (Table 4.1). The resulting area per molecule is 1.9 nm^2.
Modelling the SAM as a closely packed hexagonal layer, the area per molecule A_{mol} can be calculated as the unit cell area:

$$A_{mol} = \frac{\sqrt{3}}{2} a^2 \tag{4.1}$$

where a is the nearest-neighbour distance. The average nearest-neighbour distance can therefore be estimated from the average area per molecule as follows:

$$a = \sqrt{\frac{2A_{mol}}{\sqrt{3}}} \tag{4.2}$$

Therefore, with an area per molecule of 1.9 nm^2, an average nearest-neighbour distance a of 1.5 nm is obtained, value in good agreement with previously proposed models [179] and definitely larger than the 0.5 nm nearest-neighbour distance of compact alkanethiol SAMs [44].

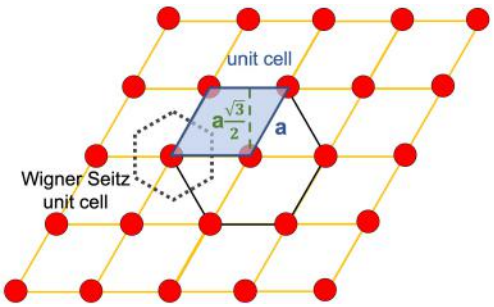

Figure 4.3 – *Sketch of the pDNA film organization, considering QCM-D results. Red circles: pDNA molecules. Hexagonal structure of pDNA SAMs is highlighted.*

After the exposure to the molecular spacer, an increase in adsorbed mass around 80 ng/cm^2 is detected. Given the molecular mass of the spacer, a molecular density of $4.1 \cdot 10^{14}$ molec/cm^2 is obtained for the mixed pDNA/MCH SAMs. The average nearest-neighbour distance in the mixed SAM is estimated around 0.53 nm, in good agreement with a high-density SAM (0.5 nm, [44]). This finding suggests that MCH fills the empty binding sites in the low coverage pDNA SAM.
Finally, the incubation in the tDNA solution leads to an increase of mass/area ratio of about 260 ng/cm^2, corresponding to a tDNA molecular density of $2.3 \cdot 10^{13}$ molec/cm^2, in agreement with previous reports [104, 106, 165, 177, 178] (Table 4.1), with a resulting area per molecule of 4.35 nm^2. The molecular density of target DNA is roughly the half of the molecular density of probe DNA ($5.3 \cdot 10^{13}$ molec/cm^2), indicating that one over two single-strand DNA filaments are hybridized by target DNA. The nearest-neighbour distance between target DNA strands calculated from the measured molecular density turns out to be 2.2 nm, a value that matches well

with the expected 2 nm diameter of a DNA double helix [180].
This finding suggests that hybridization leads to the formation of a rather dense layer of DNA double helixes, oriented almost perpendicular to the surface. In fact, molecular footprints referred to a 22-mer double helix are 15.08 nm^2/molec for a lying-down molecule and 3.14 nm^2/molec for a standing-up helix (values calculated considering a molecular length of 7.54 nm for the extended dsDNA molecule - 0.34 nm/base plus 0.6 nm for thiolated pDNA linker) and a helix diameter of 2 nm [83, 108]). Therefore, we can conclude that hybridized films are formed by quite dense and almost up-right double helixes.

4.1.2 Kinetics: QCM-D, SE and SPEE

Real-time experiments can provide information about kinetics. While the interpretation of QCM-D models is relatively straightforward as the technique measures an extensive quantity (mass/area), a detailed interpretation of SE and SPEE dynamic models is complex since these methods detect optical thickness, a quantity depending on both film thickness and film refractive index. For this reason the analysis of QCM-D data can be a helpful guide for the interpretation of the optical data. The valuable cross-fertilization between SE and QCM measurements was already demonstrated years ago [182] and will show its broad potential also in our experiments.
Figure 4.2 reports the increase of the mass adsorbed on a gold-coated QCM-D quartz. The injection of each molecular solution produces a rapid increase in the mass-to-area ratio, which remains stable after rinsing with TE buffer, indicating that the deposited molecules are strongly bound to the surface.
In order to evaluate the DNA self-assembly and the hybridization kinetics, a fit of the dynamic QCM-D data has been performed. Data referred to the self-assembly of thiolated pDNA were fitted according to a double exponential function

$$\frac{\Delta m}{A}(t) = y_0 + A_1 * e^{-(t-t_0)/\tau_1} + A_2 * e^{-(t-t_0)/\tau_2} \tag{4.3}$$

providing time constants $\tau_1 = (3.57 \pm 0.09)$ min and $\tau_2 = (17.4 \pm 0.2)$ min (with $A_1 = (-297.2 \pm 0.8)$ ng/cm^2 and $A_2 = (-332 \pm 6)$ ng/cm^2). An initial fast process (time constant of a few minutes) is followed by a slower process, suggesting a rapid initial adsorption through the thiolated linker and a successive reorganization of the pDNA strands on the gold substrate. The τ_1 value obtained is in excellent agreement with other reports in literature ($\tau = 3.3$ min in Carrascosa et al. [183]).
MCH deposition kinetics is characterized by a long time constant, $\tau = (24.2 \pm 0.5)$ min ($A = (-135.4 \pm 0.9)$ ng/cm^2), suggesting a slow MCH deposition and reorganization of the mixed film. For comparison, the kinetics of MCH deposition on a free gold surface is reported in section 4.4.2.
As concerns the tDNA adsorption, a single exponential function (Langmuir isotherm) was employed for the fit of dynamic curves [184, 185]. The resulting short time constant, $\tau = (2.73 \pm 0.06)$ min ($A = (-247 \pm 3)$ ng/cm^2), suggests a quite fast hybridization process.

Table 4.1 – *Molecular density of DNA films: comparison between experimental data presented in this thesis work and the literature. We report results obtained through different preparation protocols: although surface density may be affected by chain length, incubation time and DNA solution concentration, our results show compatibility with other reports.*

	sequence	pDNA incubation time	pDNA/tDNA concentration	pDNA (molec/cm^2)	tDNA (molec/cm^2)
Experimental data	hetero - 22 bp	3 h	1 μM	$5.3 \cdot 10^{13}$	$2.3 \cdot 10^{13}$
Khan 2014 [178]	A_{25}	40 h	3 μM	$6.6 \cdot 10^{13}$	
Li 2014 [177]	hetero - 15 bp	24 h	10 μM	$3.1 \cdot 10^{13}$	$9.0 \cdot 10^{12}$
Li 2012 [106]	hetero - 15 bp	24 h	10 μM	$3.0 \cdot 10^{13}$	$1.1 \cdot 10^{13}$
Martinez 2010 [181]	hetero - 12 bp	5 min	1 μM	$9.9 \cdot 10^{13}$	
Opdahl 2007 [173]	T_{25}	20 h	1 μM	$6.2 \cdot 10^{13}$	
Gong 2006 [165]	hetero - 20 bp	5 h	1 μM	$4.4 \cdot 10^{13}$	$(7 \div 9) \cdot 10^{12}$
Petrovykh 2004 [172]	T_{25}	2 h	1 μM	$2.9 \cdot 10^{13}$	
Steel 2000 [176]	hetero - 22 bp	20 h	1 μM	$(3 \div 4) \cdot 10^{13}$	

As mentioned above, the interpretation of dynamic ellipsometric data (both in SE and SPEE configuration) is complicated because of their dependence on two correlated quantities, the thickness and the refractive index of the film. In addition, it is worth considering that at each step of the experiment the structure of the overlayer changes, with increasing complexity: the film can be modelled as a stack of ultra thin layers with refractive index unfortunately not so different from the ambient and possibly with a lesser-defined outer interface between film and ambient. Therefore, at the angle of incidence set by the cell geometry (70°), the "visibility" of the overlayer generally changes during the measurement considering the interplay between the refractive index of the substrate, the constituting layers, and the ambient. In the case of brush-like biofilms in an aqueous environment, under particularly unfavourable conditions, it could be difficult to observe the outer part of the film, especially if hydration effects come into play [18]. Despite these possible complications, Δ transitions match mass variations as can be observed from Figure 4.4, where the time evolution of Δ following exposure to pDNA, MCH and tDNA was followed through SE and SPEE experiments.

Concerning SE dynamic analysis, as discussed in other reports [121, 186], for transparent layers Δ values in the near infra-red region (NIR) can be used as a marker of the film thickness to monitor the deposition of ultrathin layers. More rigorously, a decrease of Δ corresponds to an increase in the film optical thickness. About SPEE experiments, thin film deposition is monitored through a spectroscopic ellipsometry measurement performed in total internal reflection condition coupled with surface plasmon resonance phenomena, a method that increases the sensitivity of SE standard measurements.

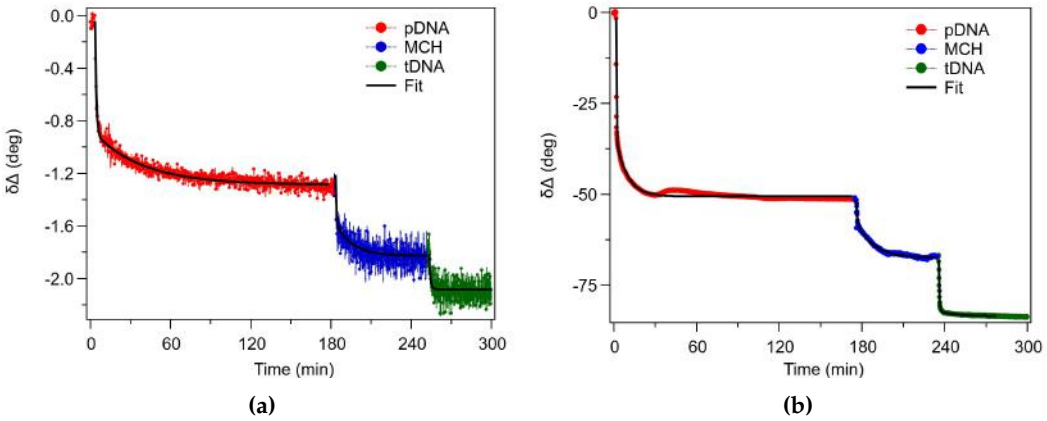

Figure 4.4 – *dsDNA/MCH film self-assembly: pDNA + MCH + tDNA. (a) SE experiment: Δ variation versus time, at λ=800 nm. (b) Δ variation versus time at λ=676 nm.*

After the injection of each molecular solution, a rapid decrease in Δ is observed, which parallels the increase of the mass/area ratio detected from QCM-D (Fig. 4.2), allowing to distinguish the 3-step deposition process. Quick examination shows that

the magnitude of the Δ jumps, induced by both MCH and tDNA deposition, are not "proportional" to those observed in QCM-D. The increase of mass (and molecular density) detected by QCM-D, in particular for the hybridization stage, seems not matched by a jump of the "equivalent" entity of optical thickness. This observation implies that optical dynamics data can not be interpreted by simple changes in film density or thickness. The optical data changes most likely reflect the morphological and structural evolution of the overlayer. In particular, this behaviour could suggest that the increase in adsorbed mass due to hybridization (as measured by QCM-D), that would lead to a "proportional" decrease in Δ under the assumption of a constant refractive index, occurs simultaneously with a lowering of the refractive index. These competing events (thickness increase and refractive index decrease) would therefore lead to smaller changes in optical experiments than in QCM-D. As it will be discussed in detail in the 4.1.5 section, this observation can be related to hypochromism, a phenomenon observed for DNA in solution, which implies a lower absorbance for double-stranded DNA than for single-stranded one.

Focusing on the comparison of Δ spectra acquired in standard SE (Fig. 4.4 (a)) and in SPEE (Fig. 4.4 (b)) configuration, we can observe that Δ changes measured by SPEE are definitely larger than those measured by SE. Because of its higher sensitivity in detecting surface modifications, SPEE is therefore a promising method to investigate molecular layer deposition.

To compare the two optical methods in a more quantitative way, a fit of SE and SPEE data was performed too. It is worth noting that the aim of this fit procedure is not to derive the time constants of the SAM deposition since, as previously discussed, the physical quantity analyzed (optical thickness) is not a direct measure of molecular deposition, being influenced by both film thickness and refractive index. For this reason, the results obtained by QCM-D must be considered for a rigorous kinetic analysis. It is however interesting to compare the results of the two optical methods. The time constants obtained from SE and SPEE are in excellent agreement (Table 4.2) at each step deposition, considering the experimental uncertainties of the two sets of measurements and remembering that SPEE experiments are preliminary. Therefore, backed by QCM-D, SE and SPEE dynamic measurements contributed to define the reaching of stationary conditions, when static, broadband optical measurements can be safely performed.

	SE (*min*)		SPEE (*min*)	
pDNA	(1.11 ± 0.04)	(44.9 ± 1.2)	(1.28 ± 0.02)	(30.7 ± 0.3)
MCH	(0.45 ± 0.11)	(12.6 ± 1.3)	(0.67 ± 0.07)	(12.0 ± 0.3)
tDNA	(1.02 ± 0.18)	/	(0.684 ± 0.015)	/

Table 4.2 – *Time constants resulting from the fitting procedure of SE and SPEE dynamic data of FZ24 SAMs deposition, performed for a quantitative comparison between the methods. Reported errors result from the fitting procedures and not consider the sample-to-sample variability. For a rigorous kinetic analysis, consider time constant resulting from QCM-D data fitting.*

4.1.3 Thickness: AFM

The effect of exposure of the pDNA films to MCH and tDNA has been monitored through AFM nanoshaving experiments. By this method, it is possible to remove molecules from selected regions by scanning the sample under high tip load. Subsequent imaging, at low applied force, allows the estimation of the film thickness as the height difference between SAM-covered and molecular-depleted regions. In this way it is possible to monitor the increase in film thickness following each step of molecular deposition.
We report an example of a nanoshaving experiment in Figure 4.5. The AFM images in Figure 4.5 (a-c) refer to pDNA, pDNA/MCH and dsDNA/MCH films, respectively. The height histograms of the images are characterized by two bell-shaped peaks: the peak at 0 nm refers to the gold surface (darker areas in AFM images), the one at higher height refers to the film (brighter areas in AFM images). The distance between the peaks, fitted by Gaussian profiles, provides an estimation of the film thickness.

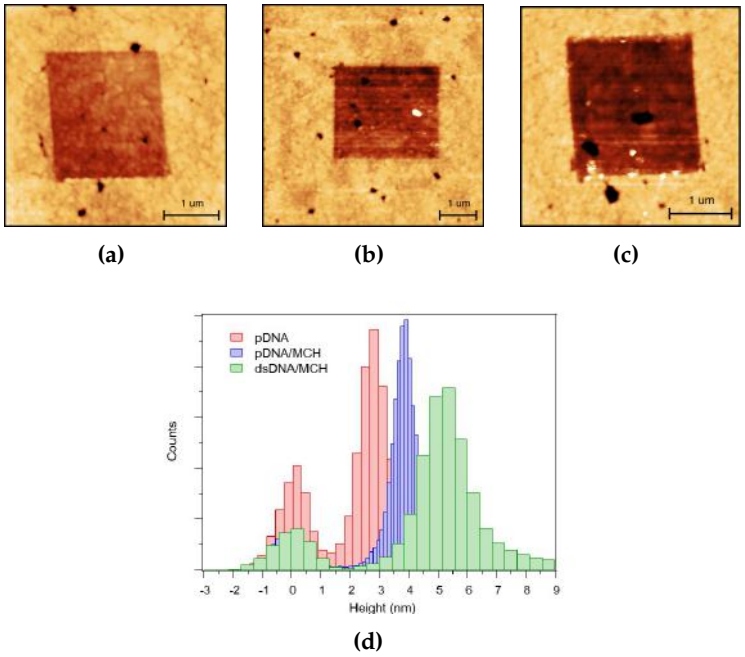

Figure 4.5 – *Example of AFM nanoshaving experiment. AFM height images of shaved patches acquired in contact mode (data scale: 8 nm) on (a) pDNA, (b) pDNA/MCH and (c) dsDNA/MCH films. (d) Height histogram of (a), (b) and (c).*

In Table 4.3 we report average film thickness estimations for each step of molecular film deposition (pDNA, pDNA/MCH, dsDNA/MCH). The thickness of pDNA SAM, definitely lower than the length of the molecule in its extended configuration (0.43 nm/base plus 0.6 nm for the pDNA linker = 10.06 nm), suggests a disordered arrangement of pDNA on the gold surface. The increase of the SAM thickness upon exposure to MCH indicates a reorganization of pDNA SAM thanks to the introduction of the spacer molecule, while the further thickness increase upon incubation in tDNA suggests the success of the hybridization process.

In particular, modelling DNA double helixes as rigid rods 2 nm in diameter and 8.08 nm in length (0.34 nm/base plus 0.6 nm for the thiolated pDNA linker), a nearest-neighbouring distance of 2.2 nm would require a tilt of the molecular axis of about 25°, with respect to the normal to the surface, to optimize inter-helix interactions. With such a tilt, a SAM thickness of 7.3 nm would be expected. The thickness of the dsDNA film measured by the AFM ((5.0 ± 0.5) nm) is in reasonable agreement with the expected thickness of the film (7.3 nm), considering the high coarseness of the model and the experimental uncertainties in the thickness estimation of such ultrathin films. To summarize, AFM nanoshaving experiments suggest a film evolution from a low density, very disordered pDNA film to a rather compact and ordered film of double helixes after hybridization with tDNA.

	Thickness (nm)
pDNA	2.4 ± 0.7
pDNA/MCH	3.5 ± 0.5
dsDNA/MCH	5.0 ± 0.5

Table 4.3 – *dsDNA/MCH film self-assembly: pDNA + MCH + tDNA. AFM nanoshaving experiment results.*

In addition to the film thickness, AFM contact experiments allow to obtain information on the film mechanical properties. In particular, the measurement of the cantilever lateral deflection gives information on the local friction between the tip and the sample surface. Figure 4.6 reports lateral deflection maps referred to the same shaving experiments analyzed in Figure 4.5.

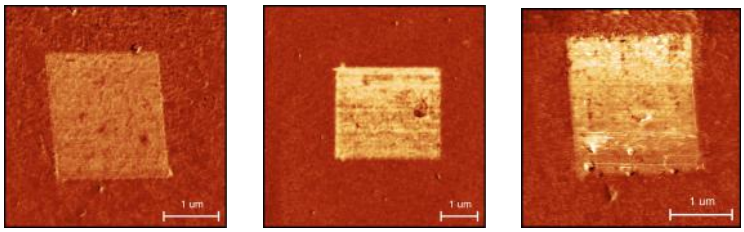

(a) **(b)** **(c)**

Figure 4.6 – *Example of AFM nanoshaving experiment. (a), (b), (c) AFM lateral deflection images of shaved patches acquired in contact mode (data scale: 0.08 V) on pDNA, pDNA/MCH and dsDNA/MCH films, respectively.*

The lateral deflection images show a difference in contrast when the tip scans over the DNA SAM or the gold substrate. This difference is low in the case of pDNA SAMs (Fig. 4.6 (a)) while it is definitely higher for mixed and hybridized SAMs (Fig. 4.6 (b) and (c)): this suggests that the presence of MCH, with a hydrophilic -OH tail-group, leads to higher friction. Taking into account previous results of QCM-D experiments and AFM height estimations, we could also reasonably assume that pDNA molecules form a low density, poorly organized layer, where the difference of

tribological properties between the organic film and the substrate is minimal. On the other hand, since the organization gets better after incubation in the molecular spacer, the differentiation between the SAM and the metal increases in the mixed films.

4.1.4 Optical thickness: SE

The analysis conducted so far has provided several insights about the formation and organization of DNA films. However, to get spectroscopic evidence of the DNA deposition we performed a detailed study of the different steps of molecular deposition through spectroscopic ellipsometry.
Difference SE spectra of pDNA ($\delta(\Delta,\Psi)_{1/0}$), pDNA/MCH ($\delta(\Delta,\Psi)_{2/0}$) and dsDNA/MCH ($\delta(\Delta,\Psi)_{3t/0}$) SAMs are reported in Figure 4.7.

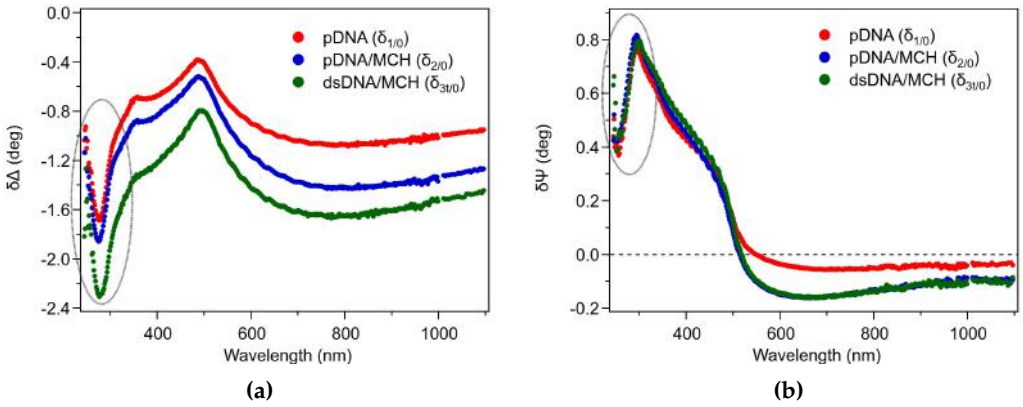

Figure 4.7 – *dsDNA/MCH film formation: SE experiment. (a) $\delta\Delta$ and (b) $\delta\Psi$ spectra of pDNA (red), pDNA/MCH (blue) and dsDNA/MCH (green) SAMs. The dashed circles indicate the UV DNA absorption fingerprint.*

Each phase of the experiment leads to quasi-rigid decrease of $\delta\Delta$ broad-band spectral values ($\delta\Delta_{3t/0} < \delta\Delta_{2/0} < \delta\Delta_{1/0}$). Decrease of $\delta\Delta$ in the NIR limit is consistent with a sequential increase of the optical thickness [186]. The values, comparable with those obtained for other in-situ investigations on biomolecules [121] are altogether very small over the whole spectral range, indicating a limited optical contrast between film and ambient. Nevertheless, one can appreciate general trends typical of difference spectra of SAMs on gold [186], which we can observe for example for a MCH film (Fig. 4.8).

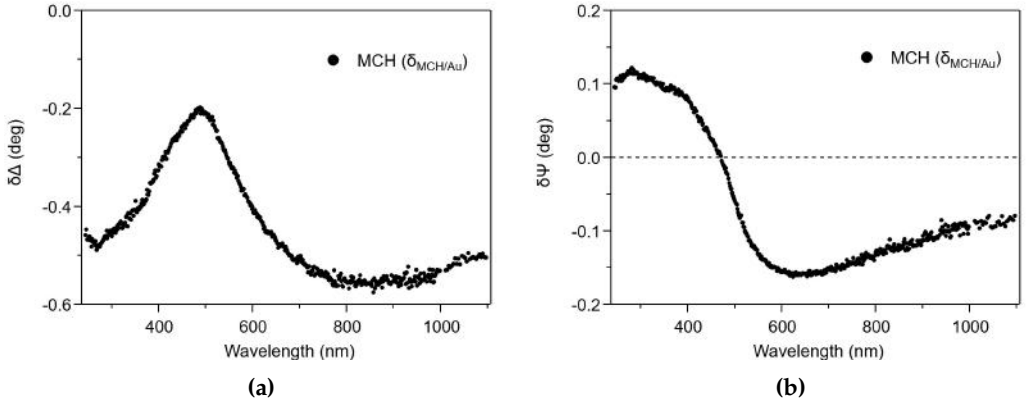

Figure 4.8 – *MCH films on gold: SE experiment. (a) $\delta\Delta$ and (b) $\delta\Psi$ spectra obtained after 1 hour deposition in 5 μM MCH solution in 1 M NaCl TE buffer.*

Around 500 nm, at the high reflectivity threshold of gold, the curves show a relative maximum in $\delta\Delta$ spectra (Fig. 4.8 (a) and Fig. 4.7 (a)) and a well-defined transition to lower values in $\delta\Psi$ spectra (Fig. 4.8 (b) and Fig. 4.7 (b)) with a minimum around 600 nm [187, 188]. In particular, the $\delta\Psi$ curve becomes negative in the NIR region. This spectral feature is related to the formation of films strongly interacting with the substrate, as in the case of alkanethiol [120] (here, we can observe this feature for MCH films (Fig. 4.8 (b)) or selenide [187] SAMs on gold, where covalent coupling between sulphur or selenium and gold occurs.
Regarding DNA SAMs, we can observe that in the NIR region the $\delta\Psi_{2/0}$ curve is lower than $\delta\Psi_{1/0}$ one: this finding suggests a modification of the interface due to the formation of new S-Au bonds [120] when the pDNA SAMs are exposed to MCH. The incubation in tDNA, as expected, does not lead to further interface changes since tDNA interacts with its complementary immobilized DNA probe and not directly with the gold surface.
A second observation regarding the comparison of SE spectra in Figure 4.7 (a) is related to the decrease of $\delta\Delta$ values in the NIR region (far from molecular resonances) at each step of molecular deposition. As already discussed in Chapter 2, an increase in $|\delta\Delta|$ values in the NIR region (far from molecular resonances) is associated with an increase of film optical thickness, implying an increase of film thickness and/or refractive index (Fig. 2.6). Indeed, for ultrathin films, like the monolayers analyzed in this study, refractive index and thickness are correlated parameters; we therefore refer to the optical thickness to account for such a correlation. SE data confirm the AFM and QCM-D observations of an increase of film coverage and thickness upon each deposition step.
Unlike MCH transparent films, DNA samples show a deep minimum around 270 nm in $\delta\Delta$ and a corresponding dip around 290 nm in $\delta\Psi$. As it will be clear from the discussion of the optical model presented in the following section, these spectral features are related to the UV-Vis absorption of DNA that can be observed in solution (transmission measurements) at 260 nm [9].

Molecular-related UV-Vis absorptions were previously identified in difference SE spectra of biomolecular layers, like Yeast Cytochrome *c* films [121]. Recent papers focused on the optical properties of DNA thin solid films [189–191], but to the best of our knowledge this is the first experimental observation of DNA molecular absorption in SE difference spectra of DNA monolayers chemisorbed on gold.

4.1.5 SE model: quantitative analysis

Ellipsometric spectra can provide valuable information on the optical properties and thickness of deposited films, through the comparison with calculated curves based on an accurate optical model of the system under investigation. These parameters are closely related to each other: disentangling the complex refractive index $\hat{N}$ and the thickness t is a hard task for an ultrathin and complex system like DNA SAMs. In this section, we will compare experimental data with simulated curves obtained by modelling the molecular film both as a transparent and an absorbing film. Some simplifying assumptions are used in the model: optical anisotropy normal to the surface has been ignored, given the small film thickness suggested by AFM, and the film has been considered as an in-plane optically uniform film since the probed area largely exceeds the molecular scale.

We started the analysis from pDNA/MCH SAMs: since the aim is to study the changes of the film during incubation in the target DNA, the analysis of the film at the previous stage was necessary.
Firstly, following the approach described in Pinto et al. [8], we modelled the DNA SAM as a transparent film (Cauchy layer) and built a 4-layer model (substrate | interface | layer | ambient) (Fig. 4.9) (for details about optical models, see section 2.1.5) as follows:

- The gold substrate is modelled using the optical constants obtained through inversion of the bare substrate spectra, which showed good agreement with the literature values.
- The interface layer is necessary to account for the negative values of $\delta\Psi$ observed above 600 nm, which are typical of strongly interacting films. Here the interface layer, which accounts for the strong interaction between gold and sulphur atoms, is modelled via a Bruggeman effective layer (effective medium approximation, EMA) [120]. An EMA layer with a thickness t_{EMA}=0.4 nm and f_{Cauchy}=80% was employed to reproduce the $\delta\Psi$ negative values in the NIR.
- The DNA layer is modelled as a transparent layer using the Cauchy model. Simulations were built fixing the film thickness $t_{tot}=t_{Cauchy}+t_{EMA}*f_{Cauchy}$)=3.5 nm, the value obtained by AFM nanoshaving measurements.
- The ambient (1 M NaCl TE buffer) was modelled as a transparent layer using the Cauchy model (A=1.33; B=0.0028 μm^2; C=0.00005 μm^4).

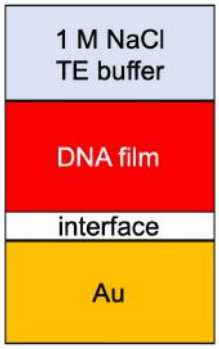

Figure 4.9 – *Scheme of the 4-layer model employed to reproduce SE experiments on DNA films (not scaled thickness).*

The comparison between experimental data and calculated spectra is shown in Figure 4.10.

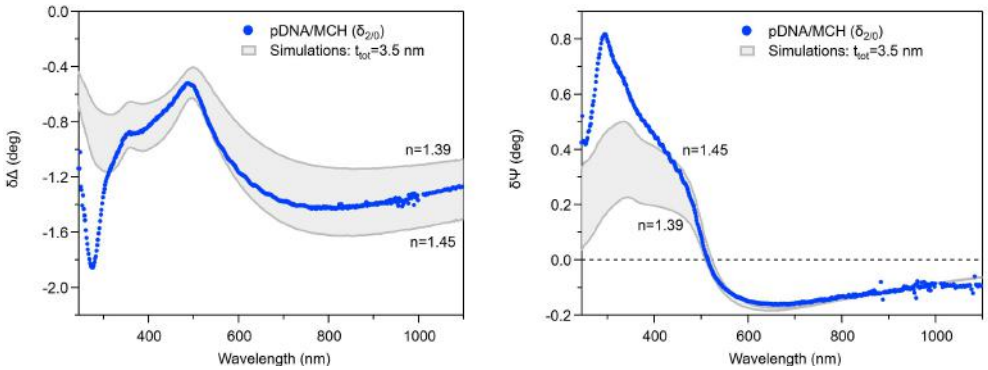

Figure 4.10 – *Comparison between SE $\delta\Delta$ pDNA/MCH data (blue circles) and calculated spectra (grey region) in NIR region. The simulations were built considering t_{tot}=3.5 nm. Reference values for refractive index at 1300 nm were reported.*

Concerning $\delta\Delta$ (Fig. 4.10 (a)), we can observe that the calculated spectra overlap well with experimental results in the NIR region (above 650 nm), while this model results inappropriate to reproduce data in the UV range. This finding is a first indication that SE is sensitive enough to detect DNA absorption even at the monolayer level. In fact DNA is an absorbing molecule in the UV region, and the minimum around 270 nm, related to DNA absorption, is not reproduced by the transparent model. Focusing on the biofilm range of transparency (NIR), after fixing the pDNA/MCH thickness to the AFM value, an A-Cauchy coefficient around 1.42 has to be chosen to reproduce the data. Such a refractive index is a reasonable result for an ultrathin organic film [120]. Similarly, the 4-layer transparent model reproduces very well $\delta\Psi$ data in the NIR region while failing in the UV region (Fig. 4.10 (b)).
Simulating DNA as a transparent molecule, therefore, allowed us to obtain important information about the optical properties of the film in the NIR region, whereas the agreement with the experimental data faded at wavelengths shorter than 600 nm.

To account for the DNA molecular absorption, starting from the above results, we developed a 5-layer optical model (substrate | interface | linker/spacer | absorbing layer | ambient) (Fig. 4.11) that considers the entire probed wavelength region and simulates DNA absorption features through an oscillator layer [121]. In the 5-layer model, the substrate, the interface and the ambient are parametrised in the same way as done in the 4-layer model. At variance with the 4-layer model, in the 5-layer model the molecular layer is modelled as a stack of two layers, a transparent Cauchy layer (to represent the spacer layer) and an absorbing layer (to represent the absorbing DNA strands). In particular:

- The spacer layer (representing the alkyl linker of pDNAs and the MCH molecules) has been modelled as a transparent layer using the Cauchy model. To fix the thickness of the spacer layer, we have chosen to set the sum of the spacer layer thickness and the spacer-bound fraction of the interface layer to the estimated length of a C6 alkyl chain, i.e., $d_{Cauchy} + d_{EMA} * f_{Chaucy} = d_{C6}$, assuming d_{C6}=0.6 nm [120]. We thus obtain $d_{Cauchy} = d_{C6} - d_{EMA} * f_{Cauchy}$=0.3 nm.

- DNA strands were simulated as an absorbing layer through a GenOsc model (subsection 2.1.5) containing two Gaussian oscillators and a pole: this last accounts for the UV DNA absorbance out of the probed spectral region (around $(190 \div 200)$ nm) [82, 192, 193]. Based on a total SAM thickness of 3.5 nm as inferred from AFM, the absorbing layer thickness was set to 2.9 nm.

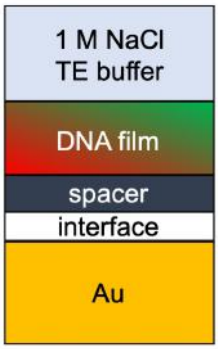

Figure 4.11 – *Scheme of the 5-layer model employed to reproduce SE experiments on DNA films (not scaled thickness).*

Table 4.4 reports the parameters used to build the 5-layer simulations for pDNA/MCH and dsDNA/MCH SAMs.

	pDNA/MCH	dsDNA/MCH
EMA	t_{EMA}=0.4 nm	t_{EMA}=0.4 nm
	f_{Cauchy}=80%	f_{Cauchy}=80%
Cauchy layer	t_{Cauchy}=0.3 nm	t_{Cauchy}=0.3 nm
	A_{Cauchy}=1.45	A_{Cauchy}=1.45
	B_{Cauchy}=0 μm^2	B_{Cauchy}=0 μm^2
	C_{Cauchy}=0 μm^4	C_{Cauchy}=0 μm^4
GenOsc layer	t_{GenOsc}=2.9 nm	t_{GenOsc}=4.4 nm
	$\varepsilon_{1\infty}$=1.75	$\varepsilon_{1\infty}$=1.78
	E_{pole}=6.29 eV (197 nm)	E_{pole}=6.29 eV (197 nm)
	A_{pole}=9.5	A_{pole}=9.5
	E_{G1}=4.80 eV (258 nm)	E_{G1}=4.75 eV (261 nm)
	A_{G1}=0.15	A_{G1}=0.15
	B_{G1}=0.5 eV	B_{G1}=0.5 eV
	E_{G2}=4.51 eV (275 nm)	E_{G2}=4.42 eV (281 nm)
	A_{G2}=0.1	A_{G2}=0.1
	B_{G2}=0.4 eV	B_{G2}=0.5 eV
$t_{tot}=t_{EMA}*f_{Cauchy}+t_{Cauchy}+t_{GenOsc}$	3.5 nm	5.0 nm

Table 4.4 – *SE analysis on FZ24 DNA SAMs: list of parameters employed in the 5-layer models (values referred to reference simulations with, respectively,* $n(1300\ nm) \sim 1.42$ *and* $n(1300\ nm) \sim 1.40$ *for pDNA/MCH and dsDNA/MCH films).*

Figure 4.12 (a-b) shows the comparison between 5-layer simulations and experimental data. It is worth noting that the calculated curves reproduce the behaviour of difference spectra, which are highly sensitive to the DNA spectral features and which emphasise the film contribution to the system optical response, hardly discernible in Ψ and Δ curves (section 2.1.4).

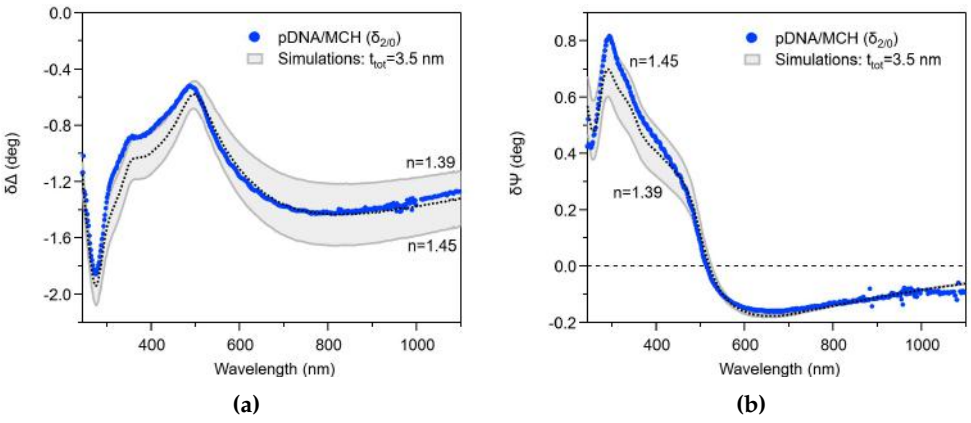

Figure 4.12 – *Comparison between SE experiments and simulations for pDNA/MCH films. (a)* $\delta\Delta_{2/0}$ *experimental data (circles) vs calculated curves (grey region). (b)* $\delta\Psi_{2/0}$ *experimental data (circles) vs calculated curves (grey region). For reference, calculated curves for n(1300 nm)=1.42 are reported too (black dashed lines).*

The 5-layer model simulations reproduced the shape of the difference spectra quite well in the whole probed spectral range. The dashed curves have been selected by looking at reproducing data above 500 nm, enabling a reliable estimate for the refractive index of the absorbing layer in the NIR. Figure 4.13 shows the corresponding real and imaginary part of refractive index.

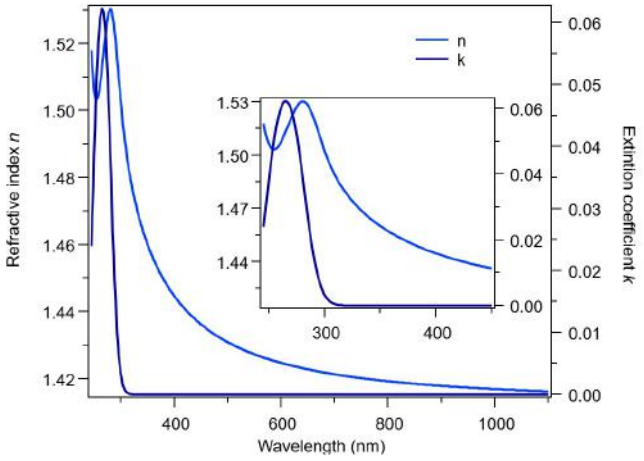

Figure 4.13 – *Refractive index and extinction coefficient related to the GenOsc layer representing FZ24 pDNA/MCH SAMs (n(1300 nm)=1.42) (dashed lines in Figure 4.12).*

In panel (a) and (b) of Figure 4.12, two more simulations (continuous curves), that differ from the dashed curve only in the value of $\varepsilon_{1\infty}$, graphically identify a region (shading) that "bounds" the experimental curves below 500 nm. The NIR refractive index corresponding to these curves is shown directly in the figure. The $\varepsilon_{1\infty}$ offset essentially determines the (real) value of refractive index in the NIR limit, with much less influence from the pole and Gaussian oscillators. Since we deal with ultrathin and relatively low-index films, $\varepsilon_{1\infty}$ exhibited a marked degree of correlation with film thickness. For this reason, as already mentioned, to mitigate index-thickness correlation issues, we resorted to AFM-nanolithography measurements to get independent film thickness data.

After successfully simulating pDNA/MCH films, we adapted the 5-layer model to double-strand DNA films. In this case, considering AFM nanoshaving results the total film thickness was fixed to 5.0 nm. The parameters used to build the 5-layer simulations for dsDNA/MCH SAMs are reported in Table 4.4.
As can be observed in Figure 4.14 (a) and (b), where the comparison between experimental data and calculated curves is reported for dsDNA/MCH SAMs, the agreement is very good also for double-strand films. As for pDNA/MCH SAMs, the dashed curves have been selected to reproduce data above 500 nm, in order to obtain a reliable estimate for the refractive index the dsDNA layer in the NIR. Figure 4.15 shows the corresponding real and imaginary part of the refractive index.

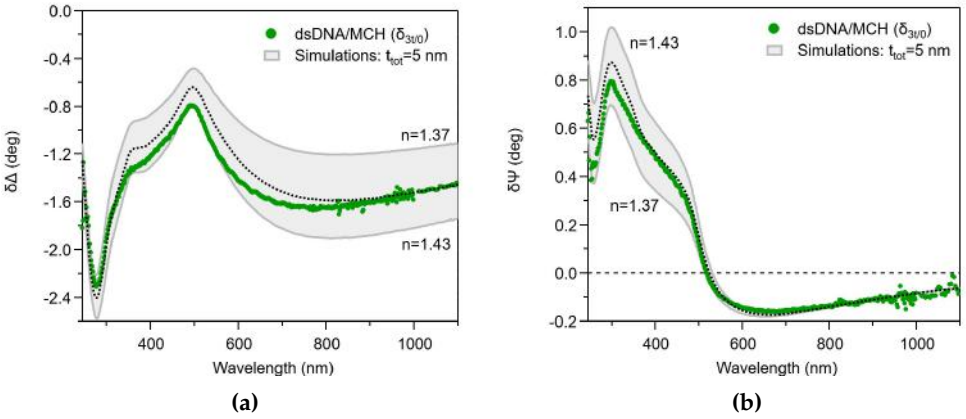

Figure 4.14 – *Comparison between SE experiments and simulations for FZ24 dsDNA/MCH films. (a) $\delta\Delta_{3t/0}$ experimental data (circles) vs calculated curves (grey region). (b) $\delta\Psi_{3t/0}$ experimental data (circles) vs calculated curves (grey region). For reference, calculated curves for n(1300 nm)=1.40 are reported too (black dashed lines).*

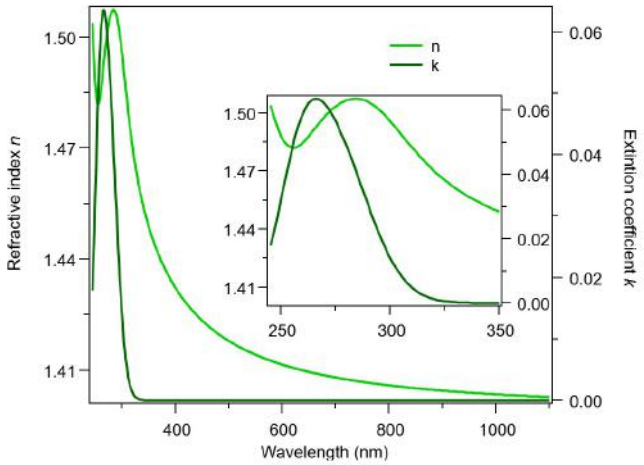

Figure 4.15 – *Refractive index and extinction coefficient related to the GenOsc layer representing FZ24 dsDNA/MCH SAMs (n(1300 nm)=1.40) (dashed lines in Figure 4.14).*

Similarly to Figure 4.12, also in panel (a) and (b) of Figure 4.14 two simulations (continuous curves) have been added, that differ from the dashed curve only in the value of $\varepsilon_{1\infty}$ and allow to graphically identify a region (shading) that "bounds" the experimental curves below 500 nm. The NIR refractive index corresponding to these curves is shown directly in the figure.

Regarding the DNA absorption, for both pDNA/MCH and dsDNA/MCH SAMs, two relatively broad Gaussian oscillators proved sufficient to account for the narrow UV dips. The position of the two oscillators is in general agreement with the literature [190, 194]; the lowest energy state likely represents the $\pi - \pi^*$ transition [195]. It should be noted that the model shows some lack of precision in the UV region. The

inaccuracy is likely connected to the general level of approximation that is inherent to the simple, isotropic stacking model, versus the actual complexity of the system. The Pole is probably too rough a model to account for the influence of oscillators out of the measurement window. In addition, the scheme adopted for the interface layer, which is effective in reproducing $\delta\Psi$ NIR data could probably introduce undesirable effects in the UV [187]. Notwithstanding the limitations of the model in describing the behaviour of a complex system like DNA SAMs, where issues like the molecular conformation or dipole interactions between nucleotide bases can play a role, a satisfactory agreement between simulation and experiment was obtained. Therefore, the overlap between simulations and experimental data provided us information about DNA absorption (from the UV region) and its organization on the surface regarding both the SAM/gold interface ($\delta\Psi$) and film refractive index ($\delta\Delta$) (from the Vis-NIR region).

Further considerations can be done on hybridization based on the inspection of raw data in the UV region (Fig 4.16). The absorption features show little change after the hybridization process, aside from a small broadening, or even a small red-shift. This measurable change between the not-hybridized (pDNA/MCH) and hybridized (dsDNA/MCH) states is worth of further investigations since it could be an additional spectroscopic feature to recognize the hybridization process. In our simulations, small shifts of the Gaussian peak positions were applied to reproduce the red-shift of the absorption feature upon hybridization. As discussed in the following, we can assign these findings to a manifestation of so-called DNA hypochromism.

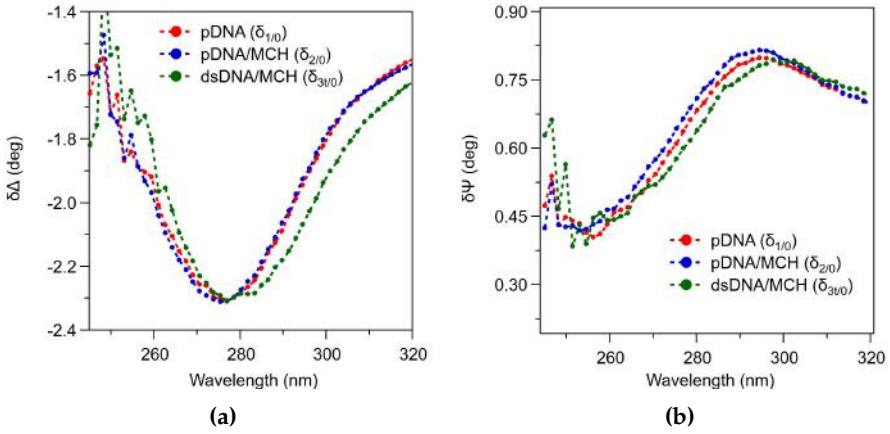

Figure 4.16 – *dsDNA/MCH film: SE experiment, focus on the UV region. (a) $\delta\Delta$ and (b) $\delta\Psi$ spectra of pDNA (red), pDNA/MCH (blue) and dsDNA/MCH (green) SAMs. pDNA and pDNA/MCH curves were shifted in the spectra in order to be aligned on the minima of the dsDNA/MCH data, for comparing the intensity of absorption features with the naked eye.*

Hypochromism, and the reverse hyperchromism in response to dehybridization, are phenomena well known from many studies of DNA in solution. A sharp increase in optical absorption efficiency, up to 30% or even more, is commonly observed after

DNA denaturation [196–199]. The origin of the phenomenon is still debated and many models have been devised to explain it [199]. Several state-of-the-art quantum chemistry calculations have examined various factors related to base stacking [200], intra- and inter-strand delocalization of excitonic states [201], or long-range interactions between nucleobases [199]. We could not find studies in literature addressing explicitly this topic for DNA SAMs. We can mention a SE study of ss-DNA immobilized on a silicon surface [194]. The spectral limitation of the experiment on the UV side prevented direct observation of DNA resonances. The authors interpreted their data with basic models and found an increase (5%) of refractive index after hybridization they judge too small, invoking a decrease in polarizability per nucleotide after hybridization.

Note that in denaturation experiments in solution the "total" number of chains is conserved, while the number of ss-chains doubles. Hybridization experiments on immobilized ss-DNA precursors differs because the "total" number of chains increases considerably in the hybridization step. In the absence of hybridization, optical experiments should therefore register a large increase in UV absorptions, and refractive index, which is not our case. In contrast, our results indicate that with hybridization, the loss of optical absorption efficiency (hypochromism) tends to offset the increase of chains (mass increase estimated about 50 % by QCM). In particular, if we assumed a starting absorption for pDNA films (and, therefore, pDNA/MCH films) $A_{ss} = n_{ss} * A_0$, after the hybridization of the half of the single-strand molecules (as measured from QCM-D experiments), in the absence of hypochromism we would expect a final absorption

$$A_{ds} = \tfrac{1}{2} n_{ss} * A_0 + \tfrac{1}{2} n_{ss} * 2A_0 = 1.5 * A_0$$

(not hybridized single-strand molecules + hybridized double-strand (*2) molecules), which is not the case in our experiments. Instead, considering hypochromism and therefore a reduction around 30% of the absorption after hybridization, a lower final intensity should be expected, around

$$A_{ds} = \tfrac{1}{2} n_{ss} * A_0 + \tfrac{1}{2} n_{ss} * 2A_0 * 0.7 = 1.2 * A_0.$$

Whereas the number of assumptions made in the model, and the overall experimental and model uncertainties, clearly dictate caution on this issue, it seems safe to rule out an increase in the NIR refractive index after hybridization, and certainly not with the magnitude that could be inferred from the increase in mass in the QMC data. Actually, we note that the comparison of Figure 4.13 and Figure 4.15 would suggest a small decrease in the refractive index after hybridization. Therefore, the observation that the dsDNA/MCH absorption intensity does not increase until $1.5 * A_0$ in SE difference spectra, and that QCM-D measurements after hybridization detect a larger increase in mass/area than the corresponding increase in optical thickness (detected by NIR-SE), can be explained by the occurrence of hypochromism. To the best of our knowledge, this is the first observation of hypochromism in ultrathin DNA films deposited on a surface.

4.1.6 Surface modifications: SPEE

As observed in dynamic experiments, SPEE configuration allows to increase SE experiment sensitivity, since the changes in Δ and Ψ associated to surface modifications are larger in SPEE than in SE standard measurements. In particular, in Table 4.5 we report the comparison between the changes due to molecular deposition detected by SPEE and SE standard experiments and plotted in Fig. 4.4. It is evident how an ellipsometric measurement carried out in SPEE configuration allows to associate, at each step of deposition, variations from 25 to 60 times greater than those detected by a SE standard experiment.

	SPEE $\delta\Delta$ (deg)	SE $\delta\Delta$ (deg)
pDNA	51.1	1.3
pDNA/MCH	15.6	0.6
dsDNA/MCH	17.3	0.3

Table 4.5 – *dsDNA/MCH film self-assembly: pDNA + MCH + tDNA. Comparison between Δ variations detected in (a) SPEE (Fig. 4.4 (b)) and in (b) SE dynamic experiments (Fig. 4.4 (a)).*

Figure 4.17 shows static Δ and Ψ SPEE spectra for the different steps of molecular deposition. Firstly, we can observe that each deposition step produces a shift of SPR features to longer wavelengths and/or to a change of their intensity. It is worth noting that, for SPEE experiment analysis, difference spectra are not necessary: in fact, surface modifications (like a film deposition) cause spectra variations that are sufficiently large to allow for the discrimination between different deposition steps. Moreover, we can observe that the SPR features (jump in Δ and minimum in Ψ spectra) are located at similar wavelengths (Ψ dip is red-shifted of 1 nm) (we recall that the feature in Δ appears as a jump due to its definition and range of visualization (Equation 2.10)).

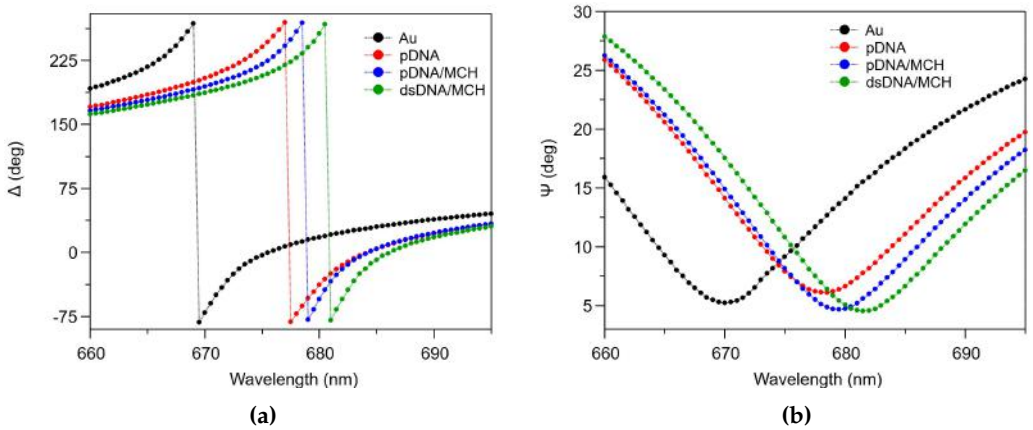

Figure 4.17 – *dsDNA/MCH film formation: SPEE experiment. (a) Δ and (b) Ψ spectra of Au substrate (black), pDNA (red), pDNA/MCH (blue) and dsDNA/MCH (green) SAMs.*

Like any SE measurement, simulations based on optical models are required to quantify SPEE static data. A sketch of the optical model is presented in Figure 4.18. Simulations have been performed with the same parameters employed for reproducing SE data (Table 4.4).

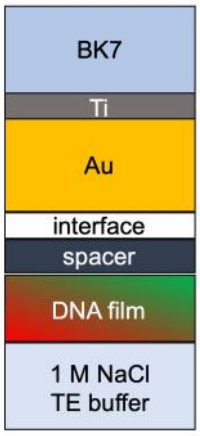

Figure 4.18 – *Scheme of the 5-layer model employed to reproduce SPEE experiments on DNA films.*

In Figure 4.19 Δ and Ψ SPEE spectra are compared with calculated curves. It is worth noting that the main spectral features, namely the red-shift and the increase of intensity of Ψ dip after hybridization, are reproduced by simulations. However, some discrepancies are observed between experimental data and simulations, expecially for the Δ curve of dsDNA/MCH and for the width of Ψ dips. Different reasons can account for the mismatch. Firstly, only a few SPEE experiments were performed and therefore data are not well-averaged as done for SE measurements. Secondly, the model used was built based on SE data that are less sensitive than SPEE data to changes in the surface layer. SPEE studies will therefore deserve further efforts, both on the experimental and modelling level, since they could improve our comprehension of the structural and optical properties of DNA films and hybridization related phenomena.

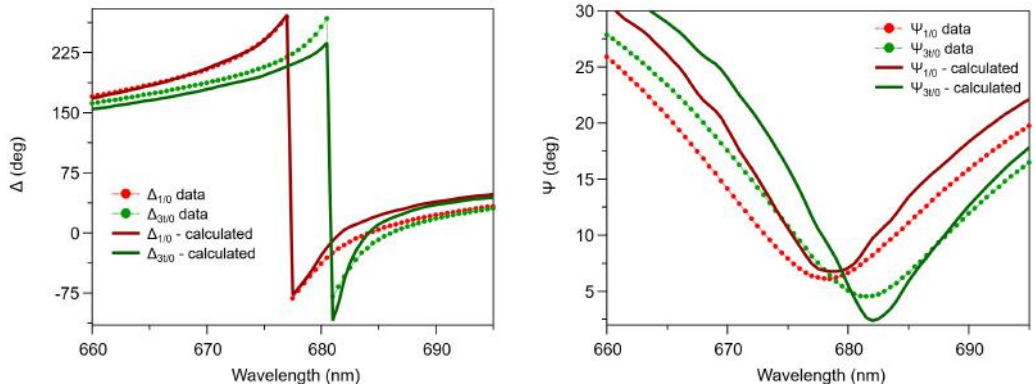

Figure 4.19 – *Comparison between SE experiments and simulations for pDNA and dsDNA/MCH films. (a) $\Delta_{1/0}$ and $\Delta_{3t/0}$ experimental data (circles) vs calculated curves (lines). (b) $\Psi_{1/0}$ and $\Psi_{3t/0}$ experimental data (circles) vs calculated curves (lines).*

4.1.7 Chemical composition and surface coverage: XPS

The evaluation of the chemical species and their chemical environment can be achieved through XPS experiments.
Firstly, a survey spectrum is acquired on the samples to recognize the main chemical elements on the sample surface. In Figure 4.20 we report a typical survey spectrum acquired on a dsDNA/MCH SAM, that shows the presence of the characteristic molecular elements (sulphur signal is not visible due to the low signal/noise ratio).

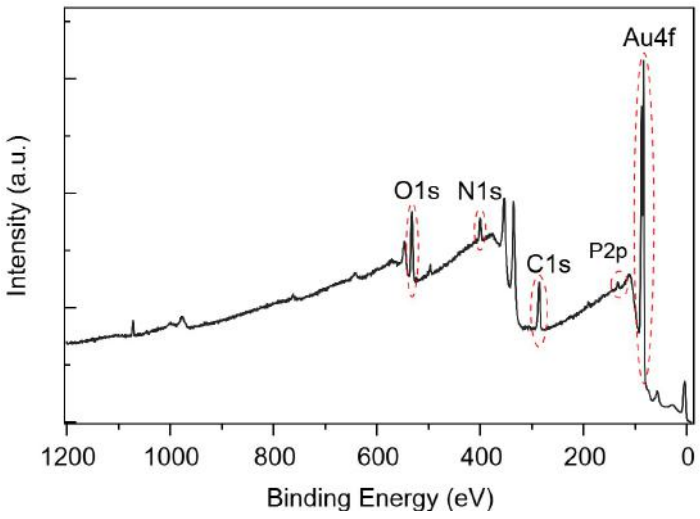

Figure 4.20 – *XPS survey referred to dsDNA/MCH SAMs.*

After the survey spectrum, high resolution spectra are acquired. In Figure 4.21 we report typical O1s, N1s, and P2p core level spectra of pDNA SAMs. These relevant molecular-related core level regions do not present significant differences in peak positions and intensities between pDNA, pDNA/MCH, and dsDNA/MCH films.

The O1s region (Fig. 4.21 (a)) can be deconvoluted with two components with FWHM=1.5 eV: O1, at (531.7 $\pm$ 0.2) eV, can be assigned to PO^{4-} groups in DNA backbones and O2, at (533.3 $\pm$ 0.2) eV, is referred to C=O [172, 174, 202, 203].
The N1s core level region (Fig. 4.21 (b)) presents two components, N1 and N2, at binding energies (399.6 $\pm$ 0.2) eV and (401.1 $\pm$ 0.2) eV with FWHM=1.5 eV. The N1 component can be assigned to amine and aromatic nitrogen (-NH_2) and N2 peak to C(=O)-N and N-C(=O)-N species [173, 174, 203, 204].
The P2p core level region (Fig. 4.21 (d)) presents a doublet, (each component with FWHM=1.4 eV) with the main $2p_{3/2}$ component at (133.8 $\pm$ 0.2) eV typical for phosphate groups in DNA strands [172, 174, 202, 203].

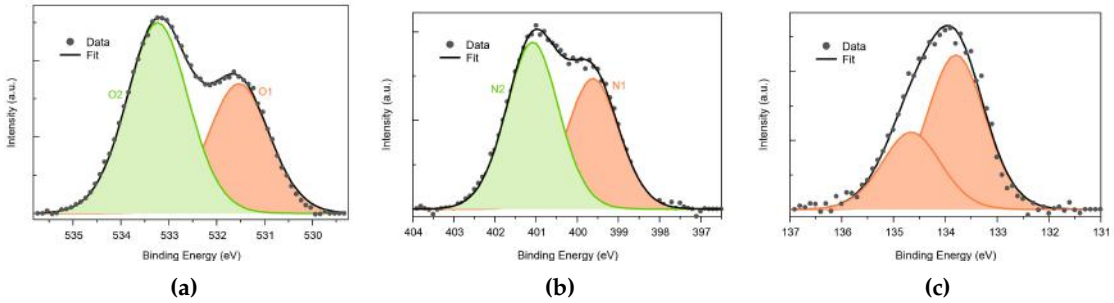

Figure 4.21 – *High resolution XPS spectra referred to pDNA SAMs: (a) O1s, (b) N1s and (c) P2p regions.*

The analysis of the C1s and the S2p core level regions at each deposition step can provide important information about the film evolution (Fig. 4.22).
Figure 4.22 (a) shows the C1s spectrum of a pDNA SAM. The signal can be deconvoluted with four Voigt functions with FWHM=1.4 eV. The C1 component at (285.6$\pm$0.2) eV represents aromatic C-C bonds, alkyl chain C-C bonds and C-S bonds; the latter ones are at the bottom of pDNA, therefore the strands "cover" this contribution that results very low. The C2 component at (287.0$\pm$0.2) eV represents C-N and C-O bonds. The last two components, C3 and C4 (around 288 eV and 289-289.5 eV, respectively), are associated with other interactions between nitrogen, oxygen, and carbon (respectively, N-C=O and N=C-N, O-C-N, N-C(=O)-N).
The C1s signal of pDNA/MCH films (Fig. 4.22 (b)) can be deconvoluted with five Voigt functions (FWHM=1.4 eV). In mixed films, C1 component is "splitted" and a new component, C5, is present at (284.8$\pm$0.2) eV representing alkyl chain C-C bonds, resulting from the chemisorption of the alkyl MCH molecules. The exposure to MCH leads also to an increase of C-S bonds but this contribution, located at the inner substrate/SAM interface, is damped by the presence of the layer. Finally, in the C1s signal of dsDNA/MCH films (Fig. 4.22 (c)) the C5 component is significantly reduced, due to the increase of the aromatic C-C signal following hybridization with tDNA strands.

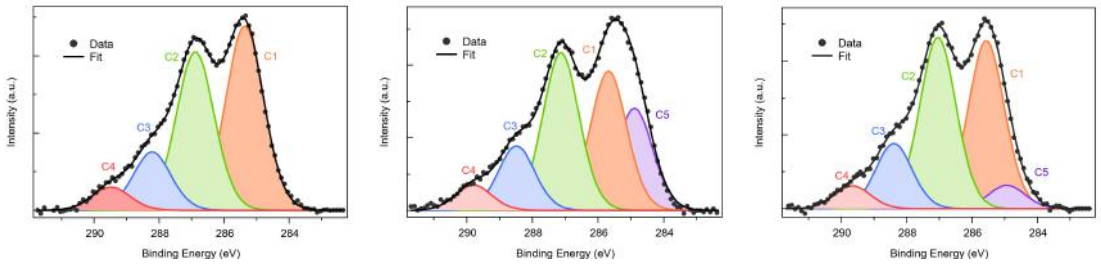

Figure 4.22 – *High resolution XPS spectra of C1s region acquired for samples (a) incubated in pDNA solution, (b) exposed to MCH and (c) hybridized with tDNA.*

The analysis of the S2p region has to be coupled with the interpretation of NIR $\delta\Psi$ behaviour, in terms of the interface effect between the film and the substrate that we presented in section 4.1.4. The comparison between the S2p core level spectra of pDNA, pDNA/MCH, and dsDNA/MCH films is reported in Figure 4.23.

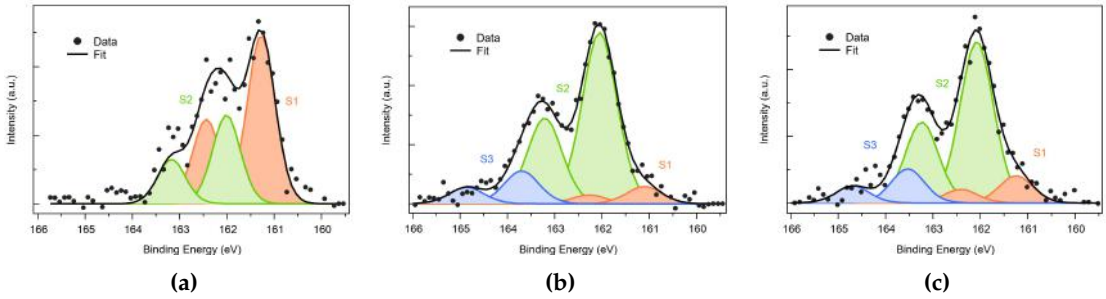

Figure 4.23 – *High resolution XPS spectra of S2p region acquired for samples (a) incubated in pDNA solution, (b) exposed to MCH and (c) hybridized with tDNA.*

Representative measurements on the pDNA S2p core level signal are reported in Figure 4.23(a). The spectrum presents two doublets (FWHM=0.7 eV) S1 and S2, with the main $2p_{3/2}$ components at BEs of (161.3±0.2) eV and (161.8±0.2) eV, respectively. Along the history of photoemission experiments on alkanethiols SAMs [47, 205–208], S2p doublets peaked around 162 eV BE have been usually assigned to so-called strongly bound species [66, 183, 209]. They can be assumed as representative of well-organized layers [210], densely-packed on gold (111) terraces. The interpretation of S2p peaks in the range $(161 \div 161.5)$ eV BE, like S1, is still controversial [211]. States in this energy range have been assigned to thiol molecules binding to gold atoms with a coordination different from the S2 case [212], possibly related to surface active sites such as defects [213] and thus, more specifically, chemisorption on steps or kinks [214, 215]. In some synchrotron experiments S1 has been assigned to the C-S bond cleavage (that would produce atomic sulphur) after irradiation damage [210, 216, 217], thermal annealing [209] or due to a contaminant [213]. Some sample-to-sample variability is observed in the intensity ratio between S1 and S2 components in pDNA SAMs.

After incubation in MCH (Fig. 4.23 (b)), the S2p core level region dramatically changes, and the S2 component dominates, while S1 almost vanishes. This behaviour suggests that the chemisorption of MCH, a short-chain thiol, competes with S1 DNA species, either directly scraping and substituting these molecules (in fact, MCH S2p spectrum is dominated by the S2 component, Fig. 4.24), or affecting gold atoms mobility thus favouring some local reorganization of the interface with changes in the molecule/gold coordination and transition into the S2 state. Both processes could explain the observed data. In addition, a low-intensity S3 component is observed, with the $2p_{3/2}$ component around 163.5 eV, assigned to so-called unbound thiol groups [66, 114, 217, 218]. We did not observe states related to oxidized sulphur at about 167-168 eV BE.
We can find the S2 component dominance also in dsDNA/MCH related spectra where, reasonably, there is no change in the S2p region since the deposition of not-thiolated molecules (tDNA) does not modify the sulphur signal.
Coupling the XPS analysis with SE $\delta\Psi$ data, the MCH-induced change of the S2p spectrum parallels the evident increase of the negative part of $\delta\Psi$ in the NIR. Relatively large, negative NIR $\delta\Psi$ are most likely associated with the S2 S2p states, confirming previous experiments on other, simpler thiols [188]. Therefore, these features are useful to discriminate between single-strand or mixed and double-strand films.

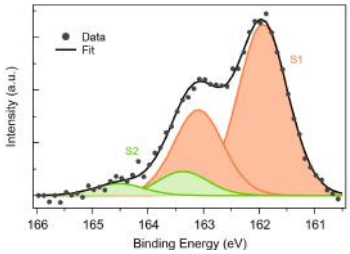

Figure 4.24 – *High resolution XPS spectra of S2p region acquired for a MCH sample incubated in TE 1 M for 1 hour.*

XPS analysis allows to quantitatively follow molecular deposition, monitoring the element/Au intensity ratios at each incubation step. In Table 4.6 it is possible to recognize an increase of the surface coverage after exposure to MCH and tDNA. Reasonably, C/Au and O/Au increase at each step, S/Au increases only after incubation in thiolated molecular spacer MCH, while N/Au and P/Au significantly increase after the incubation in a nucleic acid solution.

	C/Au	O/Au	S/Au	N/Au	P/Au
pDNA SAMs	1.9	1.0	0.03	0.46	0.14
pDNA/MCH SAMs	2.5	1.2	0.06	0.55	0.15
dsDNA/MCH SAMs	3.1	1.5	0.06	0.71	0.20

Table 4.6 – *Ratio of characteristic DNA element regions respect to Au one for pDNA, pDNA/MCH and dsDNA/MCH film.*

4.2 pDNA: ionic strength

This study is mainly based on the paper Pinto et al. 2020 [9].
The optimization of the experimental protocol started with the study of the effect of the ionic strength of the buffer solution. The mechanical properties, the film organization, and the coverage of DNA SAMs have been analyzed in-depth to define the best experimental conditions for the deposition of dense DNA SAMs.
The ionic strength of a solution is related to the intensity of the electric field generated by ion charges and is defined by the total concentration of ions according to the following definition

$$I = \frac{1}{2}\Sigma_i c_i z_i^2 \tag{4.4}$$

where, for the i-th ion, c_i is the concentration while z_i is the electrical charge. In particular, the ionic strength of a solution defines the Debye length, a quantity which describes how far its electrostatic effect persists: within the Debye length, the electric potential is decreased in magnitude by 1/e. The Debye length is defined as:

$$\lambda_D = \sqrt{\frac{\epsilon k_b T}{\Sigma n_i (z_i e)^2}} \xrightarrow{NaCl} \lambda_D = \sqrt{\frac{\epsilon k_b T}{n 2 e^2}} \tag{4.5}$$

where ϵ_0 is the dielectric function, k_b is the Boltzmann constant, z is the charge number, T is the temperature and n is the density of charges.
The behaviour of the screening of an electrically charged surface exposed to a fluid is described by the double-layer theory (Figure 4.25). On an electrically charged surface, counterions will be attracted to the surface due to the Coulomb force, resulting in a Stern layer followed by a diffuse charge layer. This attraction will weaken as you move away from the surface until reaching solution electro-neutrality.

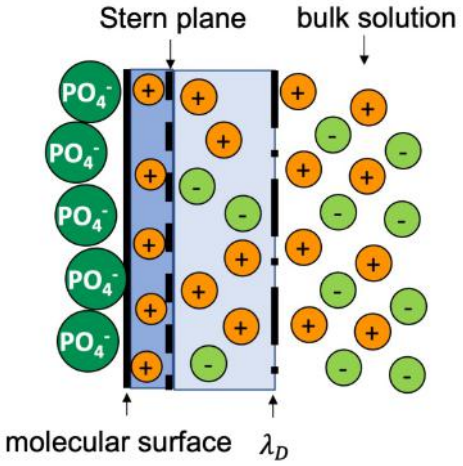

Figure 4.25 – *Scheme of the double layer theory, applied considering DNA strands as charged surface.*

In the case of DNA SAMs, the presence of NaCl influences the film deposition changing the electrical environment: increasing the the NaCl concentration (i.e. increasing the ionic strength) screens the negative charge of PO^{4-} groups of the backbone, thus

reducing the electrostatic repulsion between DNA strands. In Figure 4.26 a sketch compares the electrical environment for DNA strands in low salt conditions (1 mM NaCl) and high salt conditions (1 M NaCl) and the dependence of the potential on the distance from the surface.

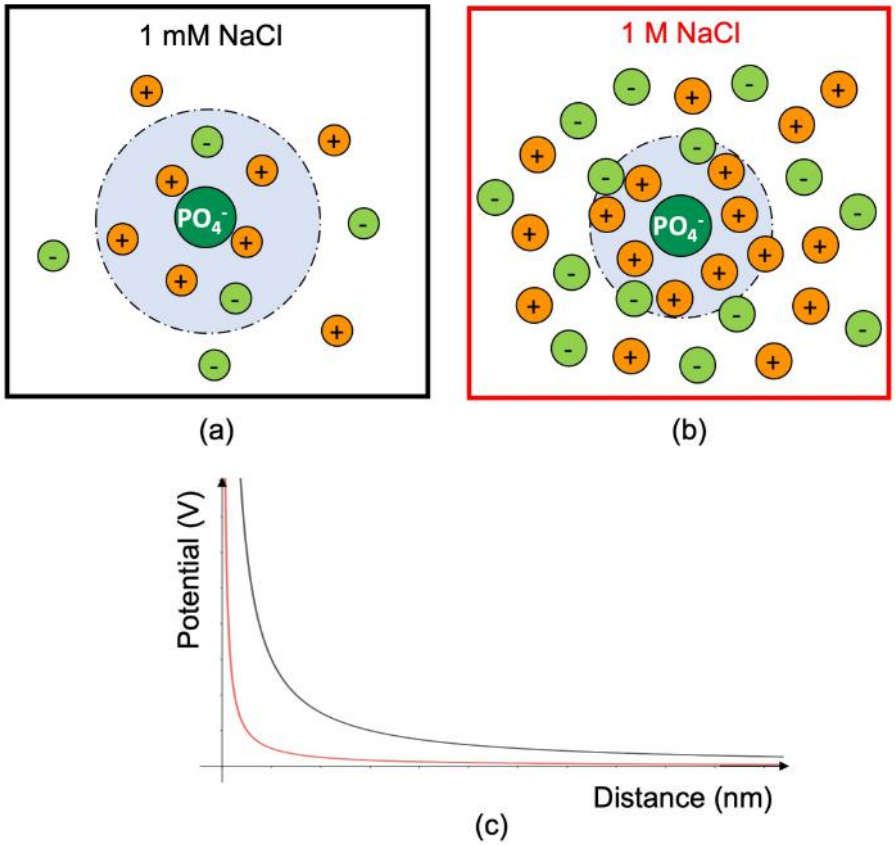

Figure 4.26 – *Effect of the ionic strength on the charge screening: DNA SAMs in (a) 1 mM NaCl and (b) 1 M NaCl buffer. (c) Comparison between the potential behaviour in different salt concentration conditions.*

We investigated pDNA SAMs immobilized for 24-hour using two NaCl concentrations, 1 mM and 1 M, chosen as extreme values to evaluate the effect of salt. Below 1 mM NaCl, since the very low-density of deposited molecules, AFM, XPS, and SE data lose their reliability due to the significant experimental uncertainties. On the other hand, based on previous reports [104–106], 1 M NaCl was chosen as a sufficiently high concentration to guarantee a full coverage molecular layer.

4.2.1 Thickness and mechanical properties: AFM

The evaluation of the mechanical properties of thin and ultrathin organic layers is an important issue for the development and optimization of biosensors since it has been demonstrated that the interaction between substrates and biosamples, in particular cells, is strongly influenced by the sample stiffness [219]. This analysis, for ultrathin films like SAMs, is a challenging task considering the difficult uncoupling between the contribution of the substrate from that of the film. In this work, we analyze

DNA films employing atomic force microscopy, a method that allows to obtain local information both on the thickness and the mechanical properties.
In the following experiments, hard tapping mode was employed to remove pDNA molecules while QI mode, together with the standard soft contact mode, was exploited to image shaved areas. Both shaving and imaging were performed in the same TE buffers used for the pDNA self-assembly.
Figure 4.27 reports the results of two shaving experiments carried out on pDNA SAMs prepared in 1 mM NaCl buffer (a-c) and 1 M NaCl buffer (d-f), respectively. Nanoshaving experiments provide film thickness estimation, thanks to the evaluation of the height difference between the SAM region and the shaved region, i.e. the gold substrate, through z-profiles or height histograms in AFM height images.

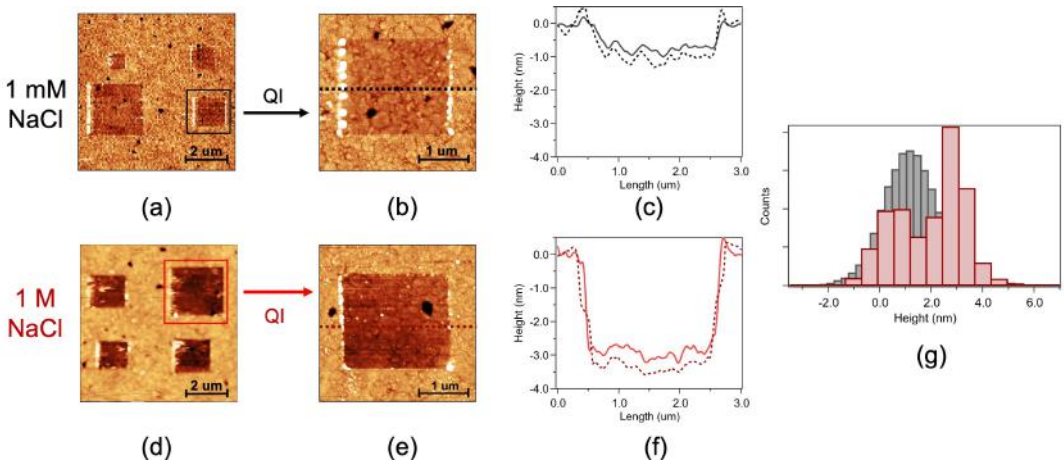

Figure 4.27 – *Shaving experiment on pDNA SAMs prepared in (a-c) 1 mM NaCl and (d-f) 1 M NaCl buffer. Height images acquired after shaving experiments in QI mode: (a,d) four shaved areas; (b,e) focus on one region (data scale: 9 nm). (c,f) z-profiles relative to contact images (light, continuous lines) and QI images (dark, dashed lines). (g) Comparison between height histograms of pDNA SAMs prepared in 1 mM NaCl (grey) and 1 M NaCl (red) buffer. Modified from [9].*

In Figure 4.27 (a) and (d) typical shaving experiments are reported, where at least four regions (darker squared areas) are depleted from DNA molecules through the application of a high load with the AFM tip while Figure 4.27 (b) and (e) shows QI height images of one shaved area (the corresponding height images acquired in soft contact mode are not reported).
In Figure 4.27 (c) and Figure 4.27 (f)) are reported z profiles measured on the soft contact images (light, continuous curves) and on the QI images (dark, dashed curves), acquired on samples prepared in 1 mM (grey curves) and 1 M NaCl buffer (red curves), respectively. The superposition of dashed and continuous curves indicates that the height estimation obtained in contact mode is slightly lower than the height value inferred from QI measurements. In contact mode, the continuous tip-sample interaction can result in drag forces which can perturb the monolayer leading to a height underestimation: minimizing as much as possible the tip load is crucial. Otherwise, in QI mode, the intermittent tip-sample interaction avoids drag effects

and results in a less disruptive operation mode. Therefore, comparative analysis in soft contact and QI modes can increase the reliability of the SAM height estimation measured by AFM. It is worth noting that the agreement between the z-profiles obtained in contact and QI modes is slightly better for films prepared at high ionic strength, indicating that these films are less vulnerable to the AFM tip perturbation thanks to a more compact and denser film organization.
From the statistical analysis of z-profiles obtained analyzing different shaved areas in several samples, we obtained an average pDNA SAM thickness of (1.0 $\pm$ 0.3) nm for samples prepared in 1 mM NaCl buffer, thickness which suggests a low-density molecular packing with almost lying-down molecules, and of (3.3 $\pm$ 0.5) nm for samples prepared in 1 M NaCl buffer.

As mentioned above, from AFM experiments information on the film mechanical properties can be obtained too. In Figure 4.28 are reported lateral deflection, slope, and Young's modulus maps referred to the same shaving experiments analyzed in Figure 4.27.
As seen for the AFM analysis in section 4.1.3, contact mode provides information about the differences in the local friction between tip and sample surface over the sample, for example over the pDNA SAM or the gold substrate. In particular, the lateral deflection images show that the difference is very low in case of 1 mM NaCl pDNA SAMs (Figure 4.28 (a) while it is definitely higher for 1 M NaCl pDNA SAMs (Figure 4.28 (e). Reasonably, for the lying-down pDNA molecules in low ionic strength conditions, it is difficult to decouple the tribological properties of the film and the gold substrate. Differently, a better organized and more compact layer forms at high salt concentration. In this case, a definitely larger difference in lateral deflection is detected when the tip scans over the gold substrate (light square) or the SAM.
QI mode allowed us to detect differences in the mechanical response of the DNA films and the gold substrate. The stiffness of the analyzed region can be inferred from slope maps obtained by calculating, for each acquired force-distance curve, the slope of a linear fit of the contact region close to the sample surface (see Fig. 2.19). When the AFM tip scans over a softer region, the cantilever could deform the sample leading to a smaller deflection and, therefore, to a lower slope in the force-distance curve. In our experiments, the DNA region appears slightly darker (Fig. 4.28 (b)) and definitely darker (Fig. 4.28 (f)) than Au substrate squares for pDNA SAMs prepared at low and high ionic strength, respectively. Lower values of the slope over the film indicate that, as expected, the DNA film is softer than the gold substrate. We can also note that, as observed for lateral deflection images, the effect is faint at low salt concentration, while in the case of high ionic strength, the difference between the stiffness of film and gold is definitely larger.
QI mode also allows for the evaluation of the difference in Young's modulus between the shaved area (gold) and the surrounding SAM (Fig. 2.19). 2D maps of the Young's modulus values are reported in Figure 4.28 (c) (low ionic strength) and Figure 4.28 (g) (high ionic strength). As expected, the gold substrate presents a definitely higher

modulus than pDNA film in the case of SAMs prepared in 1 M NaCl buffer, while at low salt concentration there is no significant difference between substrate and film. The statistical analysis of histograms of Young's modulus maps obtained analyzing different shaved areas in several samples is reported in Figure 4.28 (d) and Figure 4.28 (h). In low ionic strength conditions, the histogram (Figure 4.28 (d)) can be reproduced with a single Gaussian profile centred at 100 MPa, suggesting that no significant difference can be detected between Young's modulus of the bare and SAM covered substrate. Instead, at high ionic strength, two Gaussian profiles must be used to reproduce the histogram envelope (Figure 4.28 (h), red curve): the peak correspondent to the SAM (brown gaussian profile, centred at 57 MPa) result about 40 MPa lower than the peak correspondent to the gold substrate (yellow gaussian profile, centred at 100 MPa). In agreement with the slope analysis results, Young's modulus values of the DNA film result, as expected, lower than those of the gold substrate.

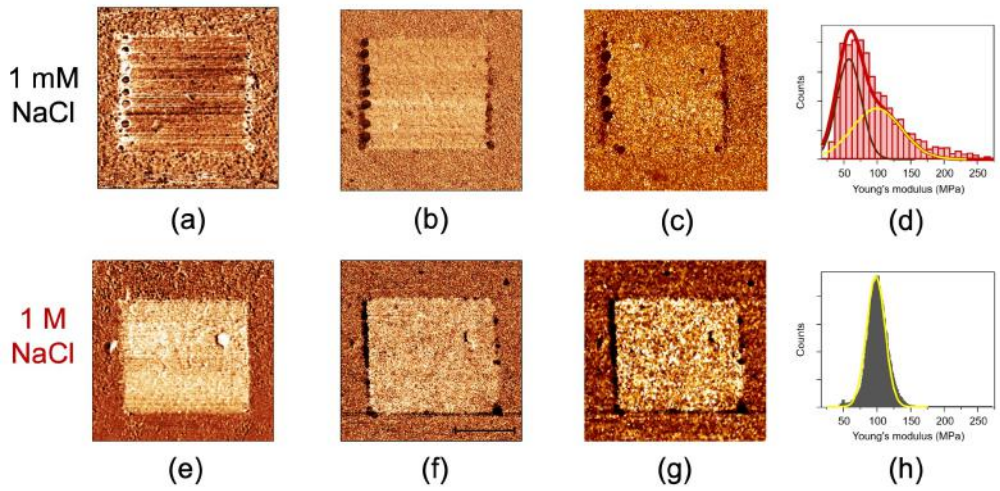

Figure 4.28 – *Shaving experiment on pDNA SAMs prepared in (a-d) 1 mM NaCl and (e-h) 1 M NaCl buffer. (a,e) Lateral deflection images acquired in contact mode (data scale: 20 mV). (b-f) Slope images acquired in QI mode (data scale: 250 N/m). (c,g) Young's modulus images obtained from QI force curves (data scale: 150 MPa) and (d,h) related histograms. Modified from [9].*

AFM nanoshaving experiments have therefore pointed out that the ionic strength of the buffer strongly influences the pDNA deposition (Figure 4.29). At low ionic strength, the highly charged DNA strands assume an elongated conformation and repel each other, forming a thin, low-density SAM of almost lying-down molecules. Conversely, at high ionic strength, the screening of the DNA charges leads to a more coiled strand conformation reducing inter-strand repulsion and forming a thicker, higher coverage SAM formed by almost up-right molecules.
This picture is in agreement with the observation, for a set SAM molecular density, of elongated DNA strands at low ionic strength and mushroom-like strands at high ionic strength [220, 221].

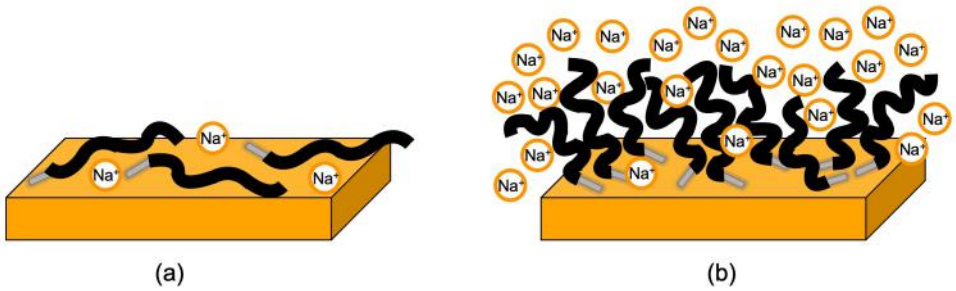

Figure 4.29 – *Sketches of pDNA SAMs immobilized in (a) 1 mM NaCl and (b) 1 M NaCl TE buffer. Modified from [9].*

4.2.2 Optical thickness: SE

A deep SE analysis was performed to characterize the optical response to different ionic strength conditions. Difference SE spectra of pDNA SAMs ($\delta(\Delta, \Psi)_{1/0}$) are reported in Figure 4.30. Spectra exhibit typical properties of difference spectra of thiol SAMs on gold [186], analyzed in-depth in section 4.1.4, like the relative maximum in $\delta\Delta$ around 500 nm, the transition to negative values of $\delta\Psi$ curve in NIR region and the remarkable deep minimum around 270 nm in $\delta\Delta$ (with the corresponding dip around 290 nm in $\delta\Psi$). It is worth remembering that these last two features are related to the strong interaction between the film and the substrate and to the DNA optical absorption, respectively.
SE data confirm that the significant role that ionic strength plays in the SAM formation. As can be observed in Figure 4.30, $|\delta\Delta|$ values in the NIR (far from molecular resonances) and $\delta\Psi$ values in the near UV are definitely larger for pDNA SAMs deposited in 1 M NaCl TE buffer than SAMs deposited in 1 mM NaCl TE buffer, suggesting a higher optical thickness for films immobilized in high salt conditions.

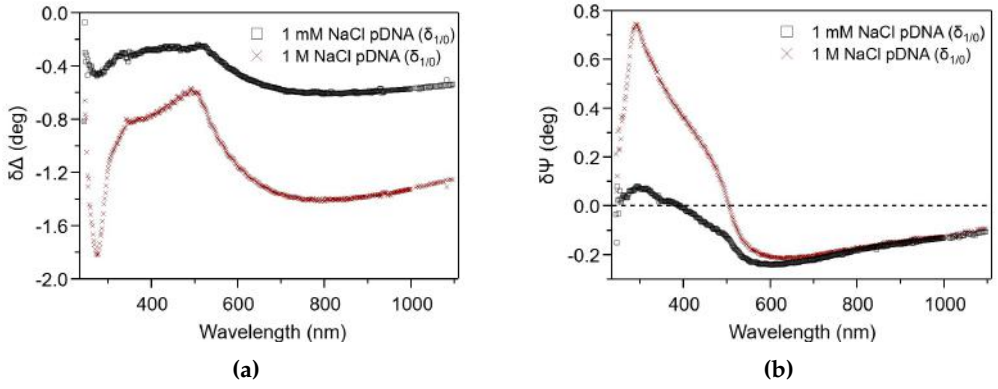

Figure 4.30 – *(a) $\delta\Delta_{1/0}$ and (b) $\delta\Psi_{1/0}$ spectra of 1 mM NaCl pDNA (black squares) and 1 M NaCl pDNA (red crosses). Modified from [9].*

4.2.3 SE model: quantitative analysis

The correlation between film thickness and refractive index, as described above, can be overcome by fixing the SAM thickness values obtained from AFM nanoshaving

experiments. Then, the comparison of SE data with simulated curves allows for the estimation of the refractive index.
We focused the analysis on 1 M NaCl pDNA films because all other experiments have been conducted in high salt conditions. Moreover, we exploit a simple 4-layer model (substrate | interface | layer | ambient) which accounts only for the behaviour in the transparency region (above 650 nm), since the absorbance features have been already analyzed in section 4.1.5 for DNA SAMs immobilized in pDNA solution for 3 hours and 1 M NaCl TE buffer.
DNA film and ambient are modelled as transparent layers using the Cauchy equation 2.14. Interface effects were included via an effective medium (EMA) layer. The Au optical constants, which showed good agreement with literature, were obtained by inversion of the spectra of bare substrates.
In Figure 4.31 (a) and (b) data referring to pDNA SAMs prepared in 1 M NaCl TE buffer are compared with simulated difference spectra calculated by fixing the thickness of the film ($t_{film} = t_{Cauchy} + t_{EMA} * f_{Cauchy}$) and using a EMA layer with a thickness (t_{EMA}) of 0.35 nm and a fraction of the Cauchy layer (f_{Cauchy}) of 75%. Shaded areas represent Cauchy simulations with A-coefficient values comprised between 1.41 (top border) and 1.43 (bottom border) (B = 0.012 μm^2). Guided by the AFM results, the film thickness was set to 3 nm, obtaining the middle curves. For comparison, curves calculated with the same A and B values and thickness equal to 2 nm and 4 nm are shown (upper and lower shaded regions, respectively). Shading helps to obtain a graphical visualization of the thickness/refractive index correlation, which characterizes ultrathin films (Fig. 4.31 (a)). On the other hand, calculated $\delta\Psi$ curves (Fig. 4.31 (b)) result almost superimposed, confirming the very low dependence on the optical thickness of $\delta\Psi$ in NIR region, as observed in Figure 4.10 too.
It can be observed that $\delta\Delta$ and $\delta\Psi$ experimental data results can be superimposed on the calculated curves obtained well, setting the film thickness to the AFM result (3 nm) and using an A coefficient ranging from 1.41 to 1.43. The refractive index used to simulate the Cauchy layer representing the pDNA film is shown in Figure 4.31 (c). The estimation of the refractive index, around 1.45 at λ=650 nm, is in good agreement with previous works based on similar systems [194, 222, 223]; the value is also reasonable comparing with values assumed in experiments on dry DNA thin films [82, 224]. In particular, a refractive index of about 1.45 is generally associated with a high film density [120, 135, 225] confirming the compactness of 1 M pDNA SAMs.

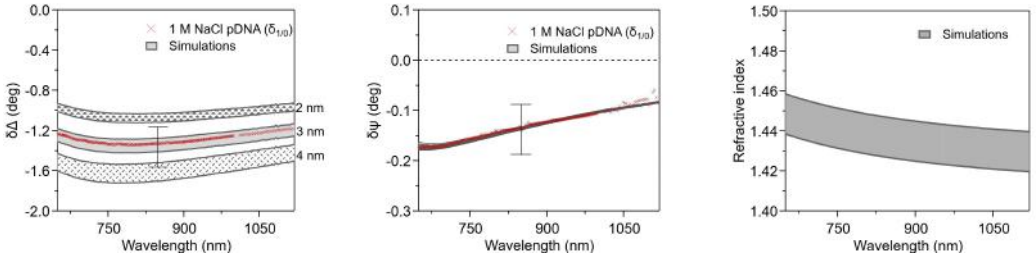

Figure 4.31 – *(a-b) Comparison between NIR SE δ-data for pDNA prepared in 1 M NaCl buffer (red crosses) and simulations (grey lines). Areas decorated with different motifs represent, for d_{film}=2 nm, 3 nm and 4 nm, simulations with Cauchy A-coefficient values comprised between 1.41 (top border) and 1.43 (bottom border), B=0.012 μm^2. Error bars take into account the sample to sample variability. (c) Refractive index referred to simulations with d_{film}=3 nm, B=0.012 μm^2 and A-coefficient values comprised between 1.43 (top border) and 1.41 (bottom border). Modified from [9].*

4.2.4 Chemical composition and surface coverage: XPS

XPS measurements have confirmed the higher film coverage at high salt concentration suggested by AFM and SE experiments.
Probe DNA films immobilized in high and low ionic strength buffers show the presence of the same molecular species but with intensity ratios between molecular and gold signals definitely lower for SAMs prepared using 1 mM NaCl TE buffer (Table 4.7). Reasonably, the higher electrostatic repulsion between negatively charged DNA backbones at low ionic strength leads to lower molecular coverage for pDNA in 1 mM NaCl TE buffer. Similar results were obtained from Herne and Tarlov [104] in 1 M KH_2PO_4 buffer.
We note that the intensity ratio values reported in Table 4.7 for pDNA SAMs deposited in 1 M NaCl TE buffer are slightly higher than the corresponding values reported in Table 4.6. This is reasonably related to the fact that Table 4.6 refers to SAMs prepared with a deposition time of 3 h while Table 4.7 refers 24 h deposition SAMs.

	C/Au	O/Au	S/Au	N/Au	P/Au
pDNA SAMs (1 mM NaCl)	1.1	0.3	0.03	0.11	0.04
pDNA SAMs (1 M NaCl)	2.7	1.3	0.05	0.63	0.18

Table 4.7 – *Ratios of characteristic DNA element regions respect to Au one for pDNA immobilized in 1 mM and 1 M NaCl TE buffer.*

In Figure 4.32 we report core-level regions of N1s and P2p, the more characteristic elements of DNA films. The comparison with 1 M NaCl pDNA SAMs (Fig. 4.21 (b) and (c)) clearly shows the difference in the signal/noise ratios. This result is also detectable for other molecular relevant signals (C1s, O1s, S2p).

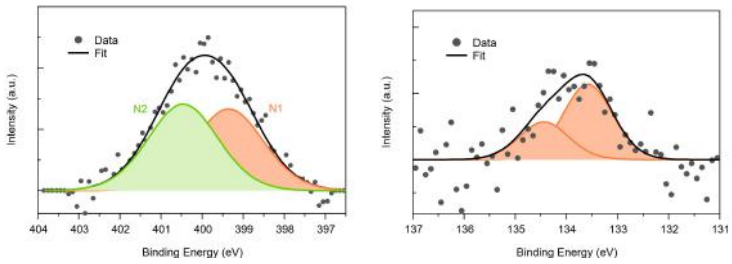

Figure 4.32 – *High resolution XPS spectra referred to pDNA SAMs immobilized in 1 mM NaCl TE buffer: (a) N1s and (b) P2p regions. Modified from [9].*

4.3 pDNA: immobilization time

The study of the effect of pDNA immobilization time has been crucial to find a trade-off between SAM quality (in terms of hybridization efficiency) and time-saving preparation protocols. The following experiments have been performed in 1 M NaCl TE buffer.

4.3.1 Kinetics: QCM-D

The analysis started with a kinetics study: QCM-D allowed to follow in real-time the molecular deposition of pDNA.
Figure 4.33 shows that the injection of pDNA solution produces a rapid increase of the mass/area ratio, which keeps stable after rinsing with TE buffer, indicating that deposited molecules are strongly bound to the surface as expected for thiolated molecules. The molecular deposition process was monitored up to 24 h. Data indicate that a plateau region is reached within a few hours, so we decided to compare the results of films immobilized for 24 hours with films incubated for only 3 hours.

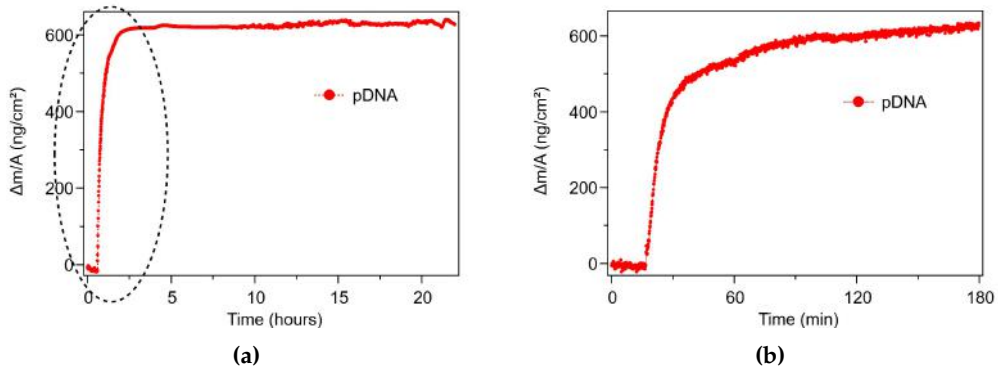

Figure 4.33 – *QCM-D analysis on pDNA film self-assembly: a) 24 h and b) 3 h focus.*

4.3.2 Thickness: AFM

AFM nanoshaving experiments allowed us to compare the film thickness of 3 h pDNA (Table 4.3) and 24 h pDNA SAMs.
Thicker pDNA films are formed for longer incubation time, as we can observe from the comparison reported in Table 4.8. As shown in the Table, comparatively thicker films are observed also after MCH and tDNA deposition in the case of pDNA films incubated for 24 h. Nevertheless, the percentage increase of film thickness from pDNA/MCH to dsDNA/MCH (i.e. the biosensor before and after the target sequence detection) is the same. This result suggests that shorter incubation time of pDNA, that facilitates the implementation of the experiment (experiments are easier to control and conduct), leaves the sensing efficiency unchanged.

	3 h (nm)	24 h (nm)
pDNA	2.4 ± 0.7	3.3 ± 0.5
MCH	3.5 ± 0.5 (+46%)	4.2 ± 0.4 (+27%)
tDNA	5.0 ± 0.5 (+43%)	6.1 ± 0.4 (+45%)

Table 4.8 – *AFM nanoshaving results for films immobilized for 3 hours and 24 hours in pDNA solution.*

4.3.3 Optical thickness: SE

The first method employed to obtain spectroscopic information was spectroscopic ellipsometry. Figure 4.34 reports static difference spectra referred to SAMs incubated for 3 hours and 24 hours in pDNA solution, that show typical features of difference spectra of DNA SAMs on gold alfready presented in the previous sections.

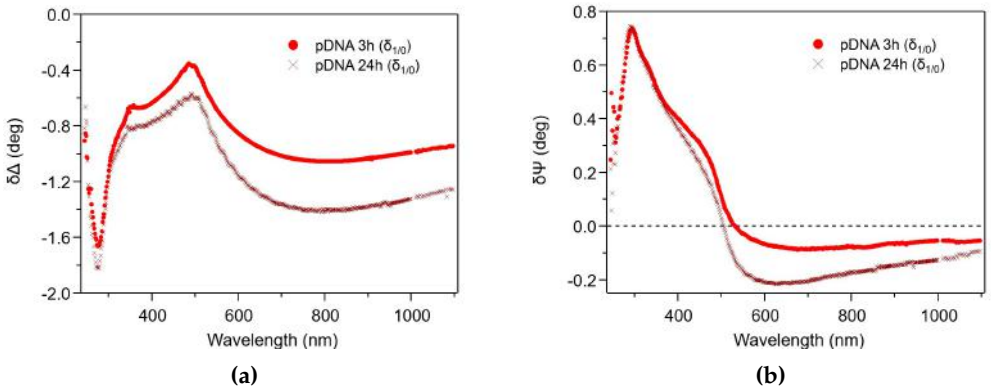

Figure 4.34 – *SE analysis pDNA film self-assembly. a) $\delta\Delta_{1/0}$ and b) $\delta\Psi_{1/0}$ SE spectra referred to 3 h pDNA (red circles) and 24 h pDNA (dark red crosses) films.*

Far from molecular resonances, in the NIR region, $|\delta\Delta_{1/0}|$ values for 24 h pDNA appear larger than 3 h pDNA data (Fig. 4.34 (a)): in particular, 3 h pDNA values are about 30% lower than 24 h DNA ones. In the same energy range, the $\delta\Psi_{1/0}$ curve of 24 h pDNA is characterized by more negative values than 3 h pDNA data (Fig.

4.34 (b)). Therefore, SE measurements show that a longer immobilization time for pDNA molecules leads to an increase of the optical film thickness ($\delta\Delta$ results) and an increased interface effect, likely related to the formation of a denser layer of strongly bound molecules ($\delta\Psi$ results).
Concerning the hybridization efficiency, SE difference spectra between dsDNA/MCH and pDNA/MCH steps ($\delta_{3t/2}(\Delta, \Psi)$) showed that the optical thickness increase is slightly higher for 3-hour samples, results in agreement with AFM result (Table 4.8) where the hybridization efficiency resulted unchanged. This result suggests that too high a density of probe DNA would risk preventing hybridization [111, 226], due to the the steric hindrance of closely packed ssDNA. Therefore, we identified shorter pDNA adsorption time as the condition that forms reproducible mixed SAMs well suited for hybridization experiments.

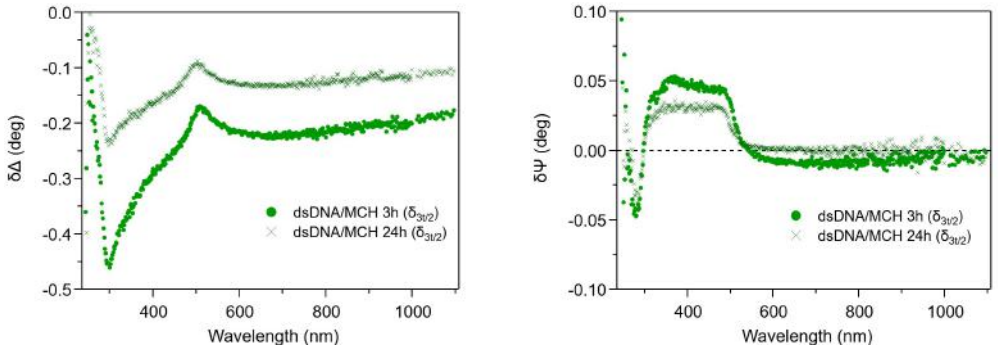

Figure 4.35 – *(a) $\delta\Delta_{3t/2}$ and (b) $\delta\Psi_{3t/2}$ spectra of dsDNA/MCH samples immobilized for 3 h (green circles) and 24 h (dark green crosses) in pDNA solution.*

4.3.4 Chemical composition and surface coverage: XPS

The SAM compositional analysis has been performed through XPS experiments. Similar C1s, N1s, O1s, and P2p signals (with the same spectra deconvolution; see Fig. 4.22 and Fig. 4.21) characterize 3 hour and 24 hour pDNA films. However, the intensity ratios between molecular-related signals (C1s, N1s, O1s, P2p) and gold-related signal (Au4f) are about $(30 \div 40)\%$ higher for 24 hour pDNA films than 3 hour ones, showing a higher molecular surface coverage for longer adsorption times. These results are in agreement with SE observation, where 3 hour film reached values 30% lower than 24 hour films.

	C/Au	O/Au	N/Au	P/Au
3 h pDNA SAMs	1.9	1.0	0.46	0.14
24 h pDNA SAMs	2.7	1.3	0.63	0.18

Table 4.9 – *Comparison between ratios of characteristic DNA element regions respect to Au one for 3-hour and 24-hour immobilization pDNA time.*

Regarding the S2p signal, 3 h and 24 h pDNA films present a similar spectra de-

convolution (as reported in Figure 4.23) with two doublets, S1 and S2 at binding energies of (161.3 $\pm$ 0.2) eV and (161.8 $\pm$ 0.2) eV, respectively. In 24 h films, S1 and S2 doublets have similar intensities, while in 3-hour films, as mentioned in section 4.1.7, the S1/S2 intensity ratio is more variable and sample dependent. This fact suggests a lower organization and a higher sensitivity to the film preparation parameters (contaminants, temperature, slightly different synthesis of strands) that can compete and form films with different molecular packing.
As observed in previous analysis, the behaviour of S2p signal can be associated with $\delta\Psi$ negative values in the NIR region. In particular, a higher interface effect (Fig. 4.34 (b)) is detectable for samples that exhibit a stronger presence of S2p compoment at 162 eV.

In conclusion, the presented multi-technique analysis of pDNA films pointed out that increasing the adsorption time from 3 to 24 hours leads to the formation of more S-Au bonds (SE interface effect and XPS S2 component) and consequently to films with a higher coverage (XPS element/Au region ratios) and higher thickness (AFM and SE optical thickness).

4.4 Molecular spacer

To investigate the role of the molecular spacer on the hybridization process, we compared the three-step experiments discussed so far with two-step experiments performed as reported in the following.

4.4.1 Role of the molecular spacer

Figure 4.36 shows $\delta\Delta$ and $\delta\Psi$ spectra referred to three-step experiments (i.e., ds-DNA/MCH films prepared by substrate incubation in pDNA, MCH and tDNA) and two-step experiments (dsDNA films prepared by substrate incubation in pDNA and, subsequently, in tDNA, without exposure to MCH). For a helpful comparison $\delta\Delta$ and $\delta\Psi$ spectra of one-step experiments (dsDNA films prepared by direct substrate incubation in a dsDNA solution) are reported as well.

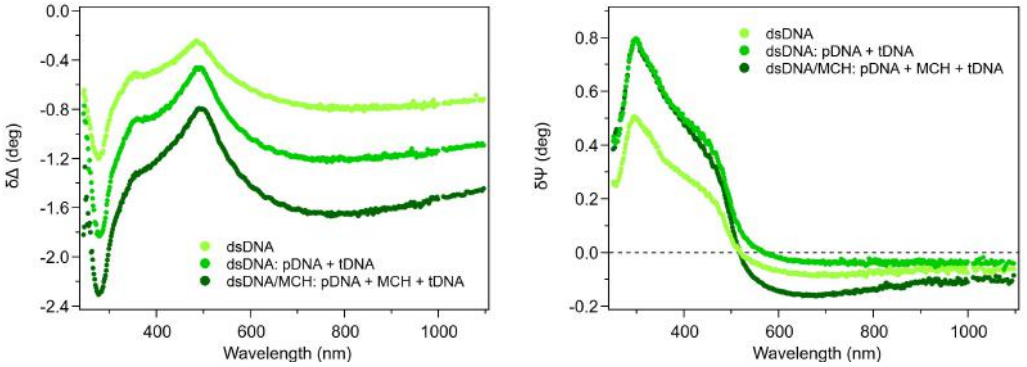

(a) **(b)**

Figure 4.36 – *dsDNA films: comparison between SE spectra of dsDNA/MCH SAMs (pDNA + MCH + tDNA)(dark green) and dsDNA films prepared by incubation in dsDNA solution (light green) or in pDNA and then in tDNA (green). (a) $\delta\Delta$ and (b) $\delta\Psi$ spectra.*

The incubation in MCH of the three-step protocol leads to the formation of dsDNA/MCH films with the largest optical thickness, approximately 1.3 times that of the two-step process and twice that of the one-step process. Since the larger the optical thickness, the easier the ellipsometric analysis, the use the spacer molecule results extremely useful.
In passing, we observe that dsDNA/MCH films show a stronger interface effect than other dsDNA SAMs (more negative $\delta\Psi$ values in the NIR region), reasonably related to the increased number of S-Au bonds following MCH deposition.
For comparison, we note that the direct deposition of the double helix leads to the formation of films with a lower optical thickness, as can be observed from the analysis of $\delta\Delta$ in the NIR region and $\delta\Psi$ in the UV range. The larger steric hindrance of dsDNA molecules compared to ssDNA ones reasonably hampers the molecular binding to the gold substrate, resulting in less dense layers.

4.4.2 MCH: concentration

Previous reports focussed on the incubation in a molecular spacer solution to improve the organization of pDNA films [104, 111, 162–164]. In this thesis, we focused on the concentration of the MCH spacer studying 5 μM and 5 mM solutions.
A higher concentration of thiolated molecules in solution leads to faster kinetics of the self-assembly on a gold substrate, as discussed in previous reports [227] and confirmed by our experiments: Fig. 4.37 reports dynamic SE scans relative to gold incubation in 5 μM and 5 mM MCH solutions. From fitting experimental data with exponential functions, the self-assembly of an MCH film incubated in a 5 μM solution shows a kinetics with $\tau_1 = (0.46 \pm 0.11)$ min and $\tau_2 = (9.5 \pm 0.8)$ min (with $A_1 = (0.31 \pm 0.04)$ and $A_2 = (0.278 \pm 0.016)$ respectively), while a 5 mM MCH film is dominated by one time constant of (0.16 ± 0.02) min (with $A = (0.78 \pm 0.07)$).

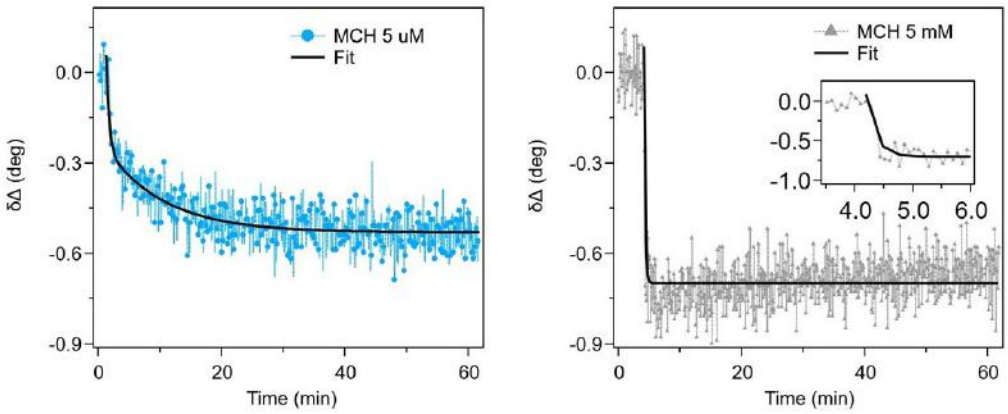

(a) **(b)**

Figure 4.37 – *Self-assembly of MCH films on gold: (a) 5 μM and (b) 5 mM MCH solution. SE experiment: Δ variation versus time, at λ=800 nm.*

Differently, the effect of MCH deposition on a pre-formed pDNA film is not easily predictable. Figure 4.38 reports QCM-D and SE dynamic scans referred to the MCH interaction with a pDNA SAM. Firstly, we can observe a good agreement between the kinetics detected through such different experimental methods.

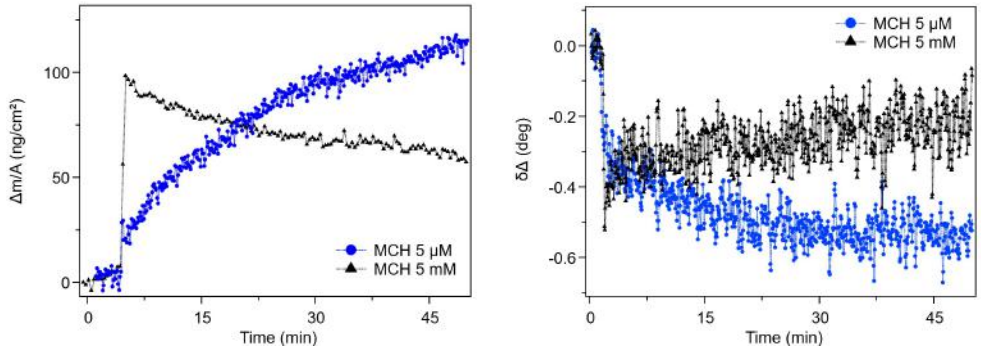

(a) **(b)**

Figure 4.38 – *pDNA SAMs incubated in MCH solution: comparison between 5 μM and 5 mM MCH solutions. (a) QCM-D experiment, (b) SE experiment: Δ variation at λ=800 nm.*

The interaction of a 5 mM MCH solution with a pDNA SAM is characterized by a large and rapid mass/area ratio and optical thickness increase, corresponding to an initial fast filling of empty binding sites among pDNA molecules by MCH molecules. This jump is followed by a slow reduction of mass/area ratio and $|\delta\Delta|$ values, which suggests a replacement, by MCH molecules, of pDNA strands that were weakly bound to the gold surface. In particular, we observe a decrease in the mass/area ratio since MCH molecules (MW: 134.24 g/mol) are smaller than pDNA strands (MW: 6992 g/mol) and can not compensate for the loss of pDNA mass. This behaviour was also confirmed by Georgiadis et al. [110].
The kinetics of 5 μM MCH deposition on pDNA SAMs, already analyzed in section

4.1.2, is slower and leads to a monotonic increase of mass/area ratio and optical thickness. We can note that larger values are reached at the end of the exposure to a 5 μM MCH solution. Since a larger optical thickness helps the molecular detection and the data analysis and since hybridization does not show a dependence on MCH concentration (Fig. 4.39), we decided to employ the lower MCH concentration for our experiments.

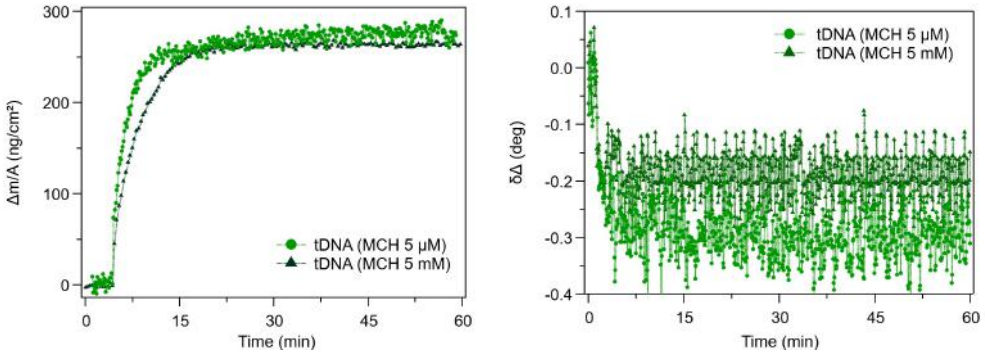

(a) **(b)**

Figure 4.39 – *Comparison between pDNA/MCH SAMs incubated in tDNA solution and prepared with MCH 5 μM (light green circles) or MCH 5 mM (dark green triangles). (a) QCM-D experiment, (b) SE experiment: Δ variation at λ=800 nm.*

4.5 tDNA: biosensor

The highly sensitive, selective and reversible interaction between complementary strands of nucleic acids makes DNA SAMs suitable for the realization of biosensing platforms. For this reason, a real-time analysis was performed in order to test and characterize these peculiar features.
Sensitivity has been tested employing different concentrations of tDNA solution, searching for the minimum concentration of analyte detectable with SE, SPEE and QCM-D. To spectroscopically validate the selectivity of the hybridization, we performed SE experiments using labelled target strands (tDNA*) and not-complementary strands (n-tDNA). Further, we evaluated the reversibility of the surface-confined hybridization by dynamic SE measurement of hybridization/de-hybridization cycles.

4.5.1 Sensitivity

One of the most relevant parameters for biosensors is the limit of detection. Exposure to different concentrations of tDNA allows for the identification of the lowest analyte concentration detectable by SE, QCM-D, and SPEE experiments. Figure 4.40 and Figure 4.41 show the changes in optical thickness (SE, SPEE) and mass/area ratio (QCM-D) induced by hybridization for different concentrations of target DNA.
Figure 4.40 shows typical SE $\delta\Delta$ spectra calculated as the difference between hybridized and mixed DNA films ($\delta\Delta_{3t/2}$). We can recognize typical DNA spectroscopic

features starting from 20 nM solution.

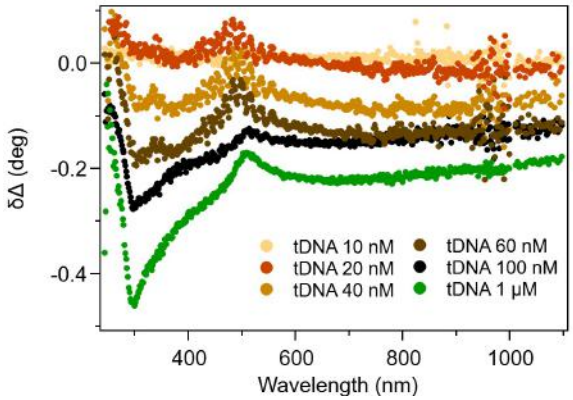

Figure 4.40 – *Test of biosensor sensitivity: exposure of pDNA/MCH SAMs to tDNA solution with different analyte concentrations. $\delta\Delta_{3t/2}$ spectrum (SE experiment).*

This detection limit can be lowered to at least 10 nM (preliminary measurements) in SPEE configuration, as can be seen from the dynamic scan shown in Figure 4.41 (a). From QCM-D experiments, we consider changes as detectable starting from a 15 nM tDNA solution (Fig. 4.41 (b)).

Note that for SE data we show difference spectra because the S/N ratio is so small that changes could not be appreciated in dynamic SE scans. Conversely, SPEE scans clearly allow for the detection of changes even for such low solution concentrations.

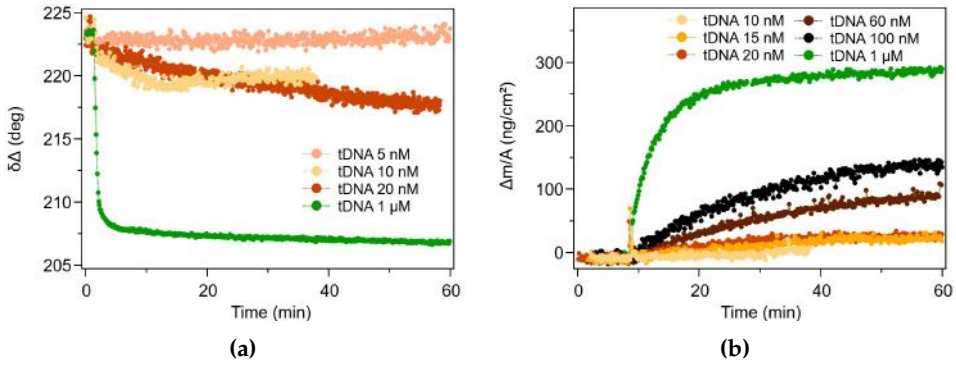

Figure 4.41 – *Test of biosensor sensitivity: exposure of pDNA/MCH SAMs to tDNA solution with different analyte concentrations. (a) Δ variation versus time at 676 nm (SPEE experiment); (b) mass/area ratio variation versus time (QCM-D experiment).*

4.5.2 Selectivity

Up to this point, we have attributed the changes detected by various experimental techniques (SE, QCM-D, AFM, XPS, SPEE) after incubation in tDNA to the successful hybridization between complementary oligonucleotide chains. However, this claim can only be made by associating these changes with a tDNA-specific signature. In

the case of pDNA deposition, we can detect the absorption feature of DNA at 260 nm (which distinguishes it from the adsorption of a transparent organic film, e.g. formed by contaminants). After MCH incubation, an increase in the interface effect related to the increase of S-Au bonds can be observed. As concerns tDNA, no chemical species (such as sulphur for MCH) allows for its identification and, at the same time, since these are ultrathin films, analysis of the evolution of the DNA adsorption feature alone would be insufficient. Therefore, we have performed experiments using fluorescence labelled tDNA strands (using the fluorescent probe Atto590): in this way, we can verify if the SE changes observed so far occur in the presence of a dye feature (and therefore of tDNA) or as a result of some contamination or reorganization of the pDNA/MCH SAMs.

Figure 4.42 compares SE difference spectra obtained after incubation in labelled tDNA (tDNA*) ($\delta_{3t*/0}(\Delta,\Psi)$, black squares) and in not-labelled tDNA ($\delta 3t/0(\Delta,\Psi)$, green circles). Spectra referred to SAMs hybridized with labelled tDNA exhibit a clear spectroscopic signature of the Atto590 dye. In particular, $\delta\Psi$ curve presents strong absorption features around 594 nm, where the Atto590 dye in solution shows absorption in transmission experiments (Fig. 4.42 (c)).

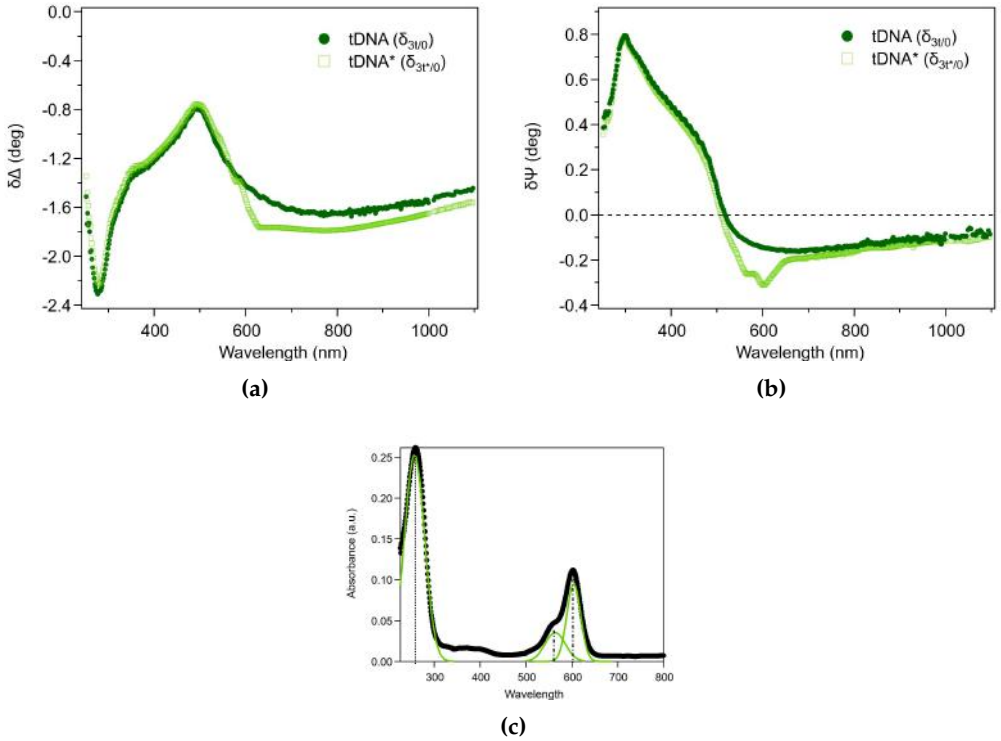

Figure 4.42 – *Test of biosensor selectivity. (a), (b) SE experiment: exposure of pDNA/MCH SAMs to tDNA $\delta_{3t/0}(\Delta,\Psi)$ (green circles) or tDNA* $\delta_{3t*/0}(\Delta,\Psi)$ (light green squares) solution. (c) Absorbance spectrum of tDNA* diluted in TE buffer (black circles) and related fit (light green curve).*

The detection of the dye absorption even after rinsing in TE buffer leads to conclude that tDNA* strands are well bound to the SAM, confirming a successful hybridization.

With the exception of the dye absorption features, the difference spectra related to incubation in tDNA* closely resemble the not-labelled dsDNA/MCH spectra. Therefore, tDNA* hybridization experiments add spectroscopic evidence to the occurrence of hybridization between complementary strands, allowing for the attribution of the increase in SE optical thickness, AFM thickness, and XPS and QCM-D coverage (detected after incubation in tDNA in previous experiments) to the selective hybridization process and thus to the DNA double helix formation (Fig. 4.7).
A closer comparison between $\delta_{3t*/0}(\Delta, \Psi)$ and $\delta_{3t/0}(\Delta, \Psi)$, shows that dsDNA*/MCH films present a slightly higher optical thickness than dsDNA/MCH SAMs, compatible with a slightly higher film thickness due to the presence of the dye.
As we have already observed, hybridization occurs between complementary nucleic acid strands. The selective recognition of target strands allows to distinguish, for example, a pathological sequence from a healthy one. In this work, we analyze the behaviour of mixed films exposed to target and non-target (15 mismatches) sequence. Future studies will focus on lowering the number of mismatches to quantitatively estimate the risk of false-positive test results.
We report difference spectra of tDNA ($\delta_{3t/2}(\Delta, \Psi)$) and n-tDNA $\delta_{3n/2}(\Delta, \Psi)$) steps referred to pDNA/MCH films in Figure 4.43. It is evident that the incubation in n-tDNA does not lead to any change in the mixed SAMs, while the exposure to complementary strand solution leads to an increase in film optical thickness ($|\delta\Delta|$ increase on the NIR) and to tiny changes in the the DNA absorption fingerprint (features around 260 nm in $\delta\Delta$ and $\delta\Psi$).

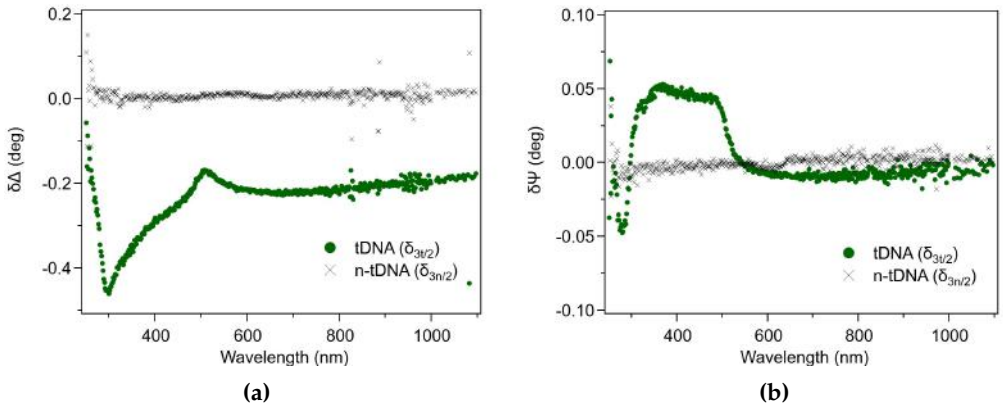

Figure 4.43 – *Test of biosensor selectivity: exposure of pDNA/MCH SAMs to n-tDNA or tDNA solution. SE experiment: (a) $\delta\Delta_{3/2}$ and (b) $\delta\Psi_{3/2}$ spectra.*

It is possible to monitor the selectivity of the hybridization also in real-time through SE, SPEE, and QCM-D dynamic scans. In Figure 4.44 we report the effect of incubation of mixed films in n-tDNA and then in tDNA solution.

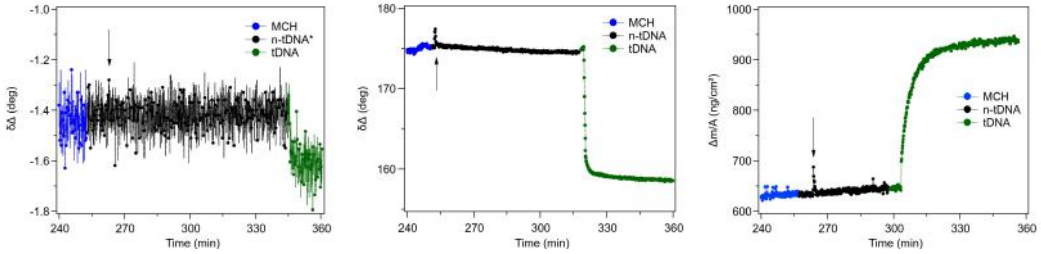

(a) **(b)** **(c)**

Figure 4.44 – *Test of biosensor selectivity: exposure of pDNA/MCH SAMs to n-tDNA or tDNA solution. Dynamic scans: (a) Δ variation versus time at 800 nm (SE experiment); (c)) Δ variation versus time at 676 nm (SPEE experiment); (c) mass/area ratio variation versus time (QCM-D experiment). Arrows indicate injection of n-tDNA solution.*

The three methods clearly detect no changes after the exposure to non-complementary strand solution (black curves), showing that a 15-mismatch sequence does not lead to any optical or mass change. Differently, tDNA leads to a fast variation of spectra, immediately detectable after solution injection (green curves).

4.5.3 Re-usability

Aiming at the development of re-usable DNA-based biosensors, the reversibility of the hybridization process is paramount. Therefore, we tested the denaturation process by exposing dsDNA/MCH films to 1 M NaOH solution to regenerate the pDNA/MCH surface. Sodium hydroxide solution is a commonly used reagent to denature the DNA: in fact, at alkaline pH, the high concentration of OH- groups interferes with the hydrogen bonds between complementary bases, resulting in double helix dehybridization [80].
Exposure to NaOH solution results in a rapid increase in Δ (indicating a decrease in optical thickness), which regains its pre-hybridization value by the time the TE buffer solution is reintroduced into the liquid cell (Fig. 4.45). The hybridization/denaturation cycles were repeated up to 5 times showing unchanged efficiency.
It can be noted that, after denaturation, the Δ values returned to the pDNA/MCH SAM values only after rinsing in TE buffer: this data highlights how the environmental media used, i.e. TE buffer and 1 M NaOH, have different optical behaviour.

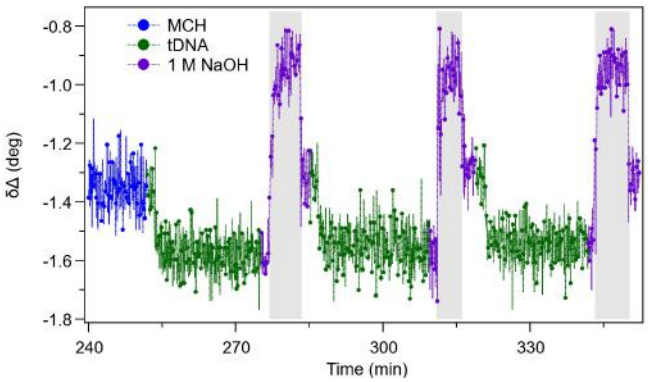

Figure 4.45 – *Test of biosensor reversibility: exposure of pDNA/MCH SAMs to tDNA, followed by denaturation through 1 M NaOH solution (3 cycles). Measurements acquired in TE buffer medium (white regions) and 1 M NaOH medium (grey regions).*

Another important issue concerning biosensor development is the preservation of the selective recognition properties of the sensing platform upon storage in dry conditions. To this end, we checked and successfully verified the occurrence of hybridization and denaturation cycles on pDNA/MCH SAMs upon at least one-week storage in dry conditions.

4.6 Application: SARS-CoV-2 detection

Detection of the viral target sequence RdRp-Helicase (28-mer), which belongs to a region of the SARS-CoV-2 gene [161], is highly attractive given possible applications related to pandemic COVID19. Employing this DNA sequence is essential to demonstrate the efficacy of our methodological approach to detect nucleic acid strands for biosensing applications.
Hybridization was performed with both target RNA (tRNA, dsRNA/MCH film) and target DNA (tDNA, dsDNA/MCH film) strands: the two chains showed no difference in double helix formation. Importantly, RNA strands require more stringent cleaning and handling protocols but, in the methods employed in this thesis work, tRNA did not lead to any particular criticality.

4.6.1 Kinetics: QCM-D and SE

The real-time analysis of RdRp-Helicase films is reported in Figure 4.46, where QCM-D and SE experiments are shown. Similar to the behaviour of FZ24 SAMs (Fig. 4.2 and Fig. 4.4 (a)), mass coverage increase and Δ decrease are detected after the exposure to pDNA, MCH, and tRNA.

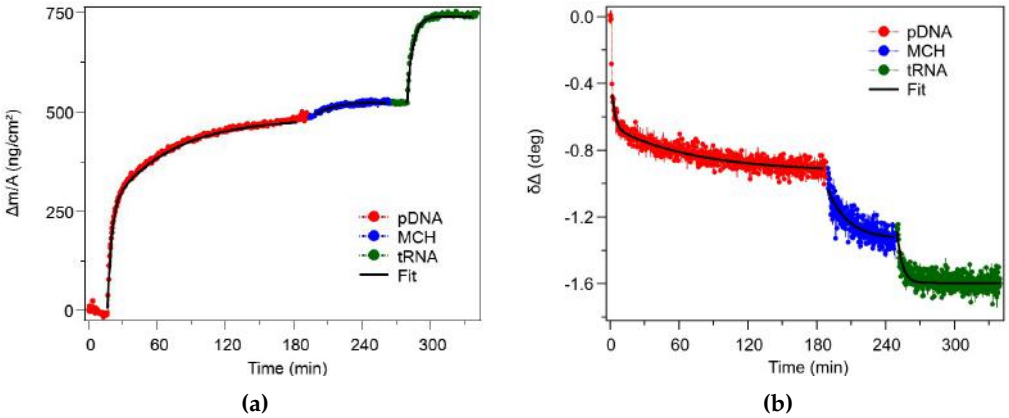

Figure 4.46 – *dsRNA/MCH film self-assembly: pDNA + MCH + tRNA. (a) QCM-D experiment: (a) mass/area ratio variation versus time; (b) SE experiment: Δ variation versus time at λ=800 nm.*

The evaluation of the DNA self-assembly and hybridization kinetics requires a fit of the QCM-D dynamic data (Table 4.10). A fit of SE data was also performed for comparison, but it is necessary to remember that the values considered as reference for kinetics analysis are the QCM-D ones, since they derive from the extensive mass/area quantity while SE data rely on the more complex optical thickness. However, a very good agreement was found for time constants obtained by the two methods.
Self-assembled thiolated pDNA data were fitted according to a double exponential function, while the fit of MCH and tRNA adsorption was performed with single exponential functions (Langmuir isotherm). A satisfactory agreement between results referred to FZ24 and RdRp-Helicase data was found. For pDNA (RdRp-Helicase) deposition, a rapid initial adsorption through the thiolated linker (τ_1 ∼3 min) and a successive reorganization of the pDNA strands (τ_2 ∼54 min) were observed, while the MCH kinetics is dominated by a relatively large time constant (∼ 19 min). Finally, the formation of the double-helix DNA/RNA provides time constants of ∼5 min for RdRp-Helicase strands, slightly longer than the ∼3 min observed for FZ24 strands, perhaps suggesting that the interaction between longer oligonucleotide chains (28-mers versus 22-mers) could require a longer hybridization time.

	QCM-D (*min*)		SE (*min*)	
pDNA	(3.41 ± 0.04)	(54.4 ± 0.4)	(2.9 ± 0.3)	(72 ± 4)
MCH	(19.0 ± 1.1)	/	(17.6 ± 1.8)	/
tDNA	(5.23 ± 0.05)	/	(4.6 ± 0.3)	/

Table 4.10 – *Time constants resulting from the fitting procedure of QCM-D and SE dynamic data of RdRp-Helicase SAMs deposition. Reported errors result from the fitting procedures and not consider the sample-to-sample variability.*

4.6.2 Coverage: QCM-D and XPS

From QCM-D, we could evaluate the mass coverage increase for each deposition step (Fig. 4.46 (a)).
Concerning the self-assembly of RdRp-Helicase pDNA, an average mass increase of 480 ng/cm^2 is detected. The resulting molecular density of $3.3 \cdot 10^{13}$ molec/cm^2 and the average nearest-neighbour distance of 1.9 nm are slightly lower than values obtained from FZ24 pDNA deposition and previous studies (Table 4.1).
The incubation in MCH causes an adsorbed mass increase around 30 ng/cm^2 (molecular density: $1.4 \cdot 10^{14}$ molec/cm^2). Such a low increase suggests the formation of a layer less packed than in the case of FZ24 SAMs; in fact, the average nearest-neighbour distance between MCH molecules is 0.9 nm for RdRp-Helicase mixed films and 0.5 nm for FZ24 mixed films. The filling process of empty binding sites between pDNA strands by MCH molecules seems to be less efficient than for FZ24 films.
Finally, tRNA strand deposition corresponds to an increase of mass/area ratio around 240 ng/cm^2, in excellent agreement with the increase detected for FZ24 films and previous reports (Table 4.1). The molecular density of tRNA ($1.7 \cdot 10^{13}$ molec/cm^2) is half of the molecular density of pDNA, indicating that for RdRp-Helicase films about 50% of pDNA chains are hybridized by the target nucleic acid. The nearest-neighbour distance between target strands results to be around 2.7 nm, in agreement with the 2.5 nm value suggested by Li et al. [228].

XPS experiments confirmed slight differences between FZ24 and RdRp-Helicase double-strand SAMs coverage without detecting any difference in the chemical species. In Table 4.11 we report the comparison between ratios of peculiar DNA element regions (C, O, S, N, P) respect to Au referred to RdRp-Helicase and FZ24 strands.
We can observe that RdRp-Helicase dsRNA/MCH SAMs exhibit lower surface coverage than FZ24 SAMs, as detected by QCM-D experiments, confirming that longer filaments slightly hinder the process of self-assembly and hybridization, resulting in a slightly lower film density.

dsDNA/MCH SAMs	C/Au	O/Au	S/Au	N/Au	P/Au
RdRp-Helicase	2.4	1.2	0.03	0.58	0.15
FZ24	3.1	1.5	0.06	0.71	0.20

Table 4.11 – *Comparison between ratios of characteristic DNA element regions respect to Au one for double strand films of RdRp-Helicase and FZ24.*

4.6.3 Thickness: AFM

AFM nanoshaving experiments conducted on RdRp-Helicase SAMs helped monitoring the effect of the exposure of pDNA films to MCH and tDNA. We report an example of a nanoshaving experiment in Figure 4.47.

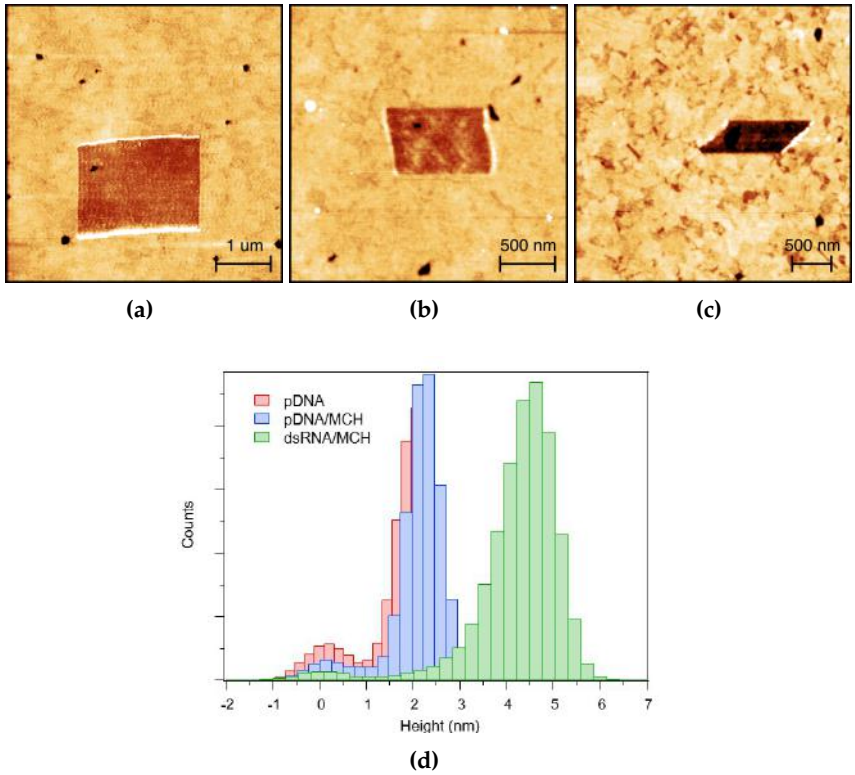

Figure 4.47 – *Example of AFM nanoshaving experiment on RdRp-Helicase SAMs. Height AFM image of shaved patches acquired in contact mode (data scale: 7 nm) on (a) pDNA, (b) pDNA/MCH and (c) dsRNA/MCH films. (d) Height histogram of (a), (b) and (c). The reference distribution corresponds to the SAM surface (brighter areas in AFM images) whereas the other peak corresponds to shaved regions (darker areas in AFM images).*

The single-strand and the double-strand films present comparable heights with FZ24 pDNA SAMs (Table 4.3) within the experimental error, with values around 2 nm and 4.5 nm. Instead, the exposure to the MCH molecular spacer only slightly affects the height of the RdRp-Helicase pDNA films. This result supports QCM-D mass coverage data, that indicate a mass increase of only 30 ng/cm^2 after the incubation in MCH for RdRp-Helicase while an increase of 80 ng/cm^2 was found for FZ24, .
In Table 4.12 we report AFM results referred to RdRp-Helicase SAMs. These results are important to guide quantitative SE analysis, which can provide spectroscopic evidence to discriminate between ssDNA and dsDNA films.

	Thickness (nm)
pDNA	2.0 ± 0.6
MCH	2.3 ± 0.5
tRNA	4.5 ± 0.3

Table 4.12 – *AFM nanoshaving results for RdRp-Helicase films.*

4.6.4 Optical thickness: SE

SE experiments have been performed to optically characterize RdRp-Helicase SAMs, aiming at exploiting the DNA absorption feature as fingerprint of successful recognition of the target strands. In Figure 4.48 we report SE difference spectra referred to RdRp-Helicase films. Ellipsometric measurements confirmed QCM-D and AFM findings.
Starting from the analysis of pDNA SAMs, we can observe that RdRp-Helicase strands form films with a slightly lower optical thickness but with the same shapes and features, like the DNA absorption, as FZ24 layers (Fig. 4.7).
Incubation of RdRp-Helicase pDNA films in MCH solutions leads to mixed films exhibiting some differences compared to FZ24 mixed films. In particular, FZ24 mixed films show more interface effect due to S-Au bonds ($\delta\Psi$ negative in the NIR) and a greater optical thickness ($|\delta\Delta|$ larger in the NIR), confirming QCM-D and AFM findings.
Finally, double-strand SAMs of RdRp-Helicase and FZ24 are similar, as confirmed by AFM height estimations and QCM-D mass coverage results. The slightly lower-density pDNA SAM does not affect the dsDNA/MCH state significantly.

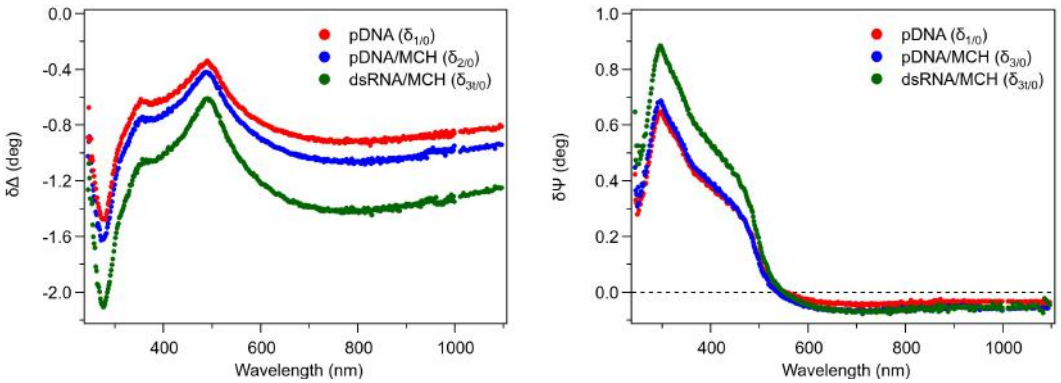

Figure 4.48 – *RdRp-Helicase dsDNA/MCH film formation: SE experiment. (a) $\delta\Delta$ and (b) $\delta\Psi$ spectra of pDNA (red), pDNA/MCH (blue) and dsRNA/MCH (green) SAMs.*

4.6.5 SE model: quantitative analysis

The quantification of ellipsometric data required the construction of an appropriate optical model, as in the case of FZ24 films (section 4.1.5). Simulations were built ignoring the optical anisotropy normal to the surface (small film thickness estimated by AFM) - and considering the film as an in-plane optically uniform film (the probed area largely exceeds the molecular scale).
Simulated curves were obtained by modelling the molecular film as an absorbing film through the 5-layer model (substrate | interface | linker/spacer | layer | ambient) (Fig. 4.11), parametrising the layers in the same way as done in section

4.1.5. The thickness of the whole film (t_{tot}=t_{Cauchy}+t_{EMA}*f_{Cauchy}) was fixed to 2.3 nm for pDNA/MCH SAMs and to 4.5 nm for dsRNA/MCH SAMs, values obtained from AFM nanoshaving measurements (Table 4.12). Table 4.13 shows the list of parameters used to build the RdRp-Helicase 5-layer model.

	pDNA/MCH	dsRNA/MCH
EMA	t_{EMA}=0.16 nm	t_{EMA}=0.16 nm
	f_{Cauchy}=70%	f_{Cauchy}=70%
Cauchy layer	t_{Cauchy}=0.49 nm	t_{Cauchy}=0.49 nm
	A_{Cauchy}=1.45	A_{Cauchy}=1.45
	B_{Cauchy}=0 μm^2	B_{Cauchy}=0 μm^2
	C_{Cauchy}=0 μm^4	C_{Cauchy}=0 μm^4
GenOsc layer	t_{GenOsc}=1.7 nm	t_{GenOsc}=3.9 nm
	$\epsilon_{1\infty}$=1.88	$\epsilon_{1\infty}$=1.75
	E_{pole}=6.29 eV (197 nm)	E_{pole}=6.29 eV (197 nm)
	A_{pole}=9.5	A_{pole}=9.5
	E_{G1}=4.79 eV (259 nm)	E_{G1}=4.79 eV (259 nm)
	A_{G1}=0.28	A_{G1}=0.18
	B_{G1}=0.48 eV	B_{G1}=0.42 eV
	E_{G2}=4.54 eV (273 nm)	E_{G2}=4.44 eV (279 nm)
	A_{G2}=0.22	A_{G2}=0.13
	B_{G2}=0.42 eV	B_{G2}=0.44 eV
t_{tot}=t_{EMA}*f_{Cauchy}+t_{Cauchy}+t_{GenOsc}	2.3 nm	4.5 nm

Table 4.13 – *SE analysis on RdRp-Helicase DNA SAMs: list of parameters employed in the 5-layer models (values referred to reference simulations with, respectively, n(1300 nm)∼ 1.47 and n(1300 nm)∼ 1.42 for pDNA/MCH and dsRNA/MCH films).*

Figure 4.49 (a-b) shows the comparison between calculated curves and experimental data referred to the mixed films. The dashed curves have been selected by looking at reproducing data above 500 nm, enabling a reliable estimate for the refractive index of the absorbing layer in the NIR (in Fig. 4.49 (c) the corresponding real and imaginary part of refractive index are reported). Two more simulations (continuous curves), that differ from the dashed curve only in the value of $\varepsilon_{1\infty}$ (parameter which essentially determines the real value of refractive index in the NIR limit), graphically identify a region (shading) that "bounds" the experimental curves below 500 nm (n between 1.44 and 1.50). Since we deal with ultrathin and relatively low-index films, $\varepsilon_{1\infty}$ exhibited a marked degree of correlation with film thickness. For this reason, the employment of AFM-nanolithography measurements to get independent film thickness data is essential to mitigate index-thickness correlation issues.

We can observe that the 5-layer model simulations reproduced the shape of the difference spectra very well in the whole probed spectral range, reproducing all the

experimental features like the position and the shape of the narrow features around 260 nm (DNA absorption), the location of $\delta\Delta$ maximum at about 500 nm, and the $\delta\Psi$ negative values in NIR region, providing important quantitative information.

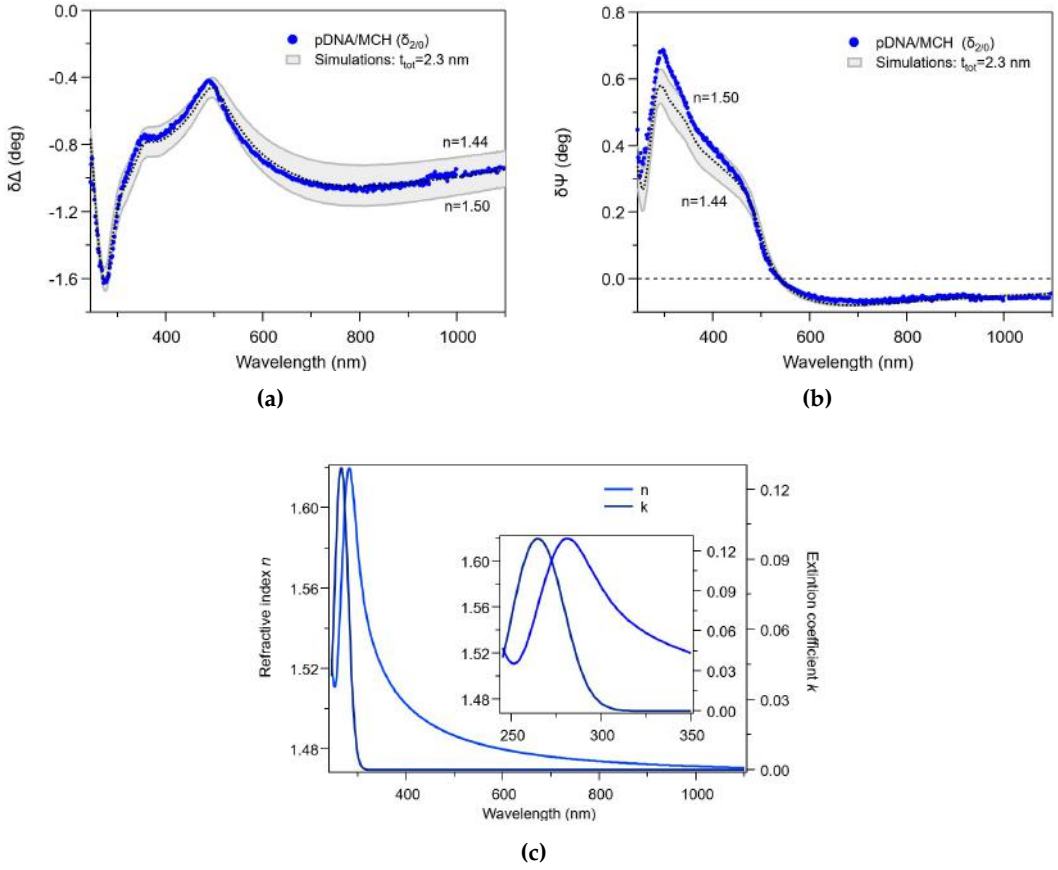

Figure 4.49 – *Comparison between SE experiments and simulations for RdRp-Helicase pDNA films. (a) $\delta\Delta_{2/0}$ experimental data (circles) vs calculated curves (grey region). (b) $\delta\Psi_{2/0}$ experimental data (circles) vs calculated curves (grey region). For reference, calculated curves for n(1300 nm)=1.47 are reported too (black dashed lines). (c) Refractive index and extinction coefficient related to the GenOsc layer representing RdRp pDNA/MCH SAMs (n(1300 nm)=1.47).*

Given the good agreement between experimental data and simulations referred to pDNA/MCH films, we applied the 5-layer model also to RdRp-Helicase dsRNA/MCH films (Fig. 4.50). As for pDNA/MCH SAMs, the dashed curves have been selected to reproduce data above 500 nm, in order to obtain a reliable estimate for the refractive index the dsDNA layer in the NIR. Moreover, two simulations (continuous curves) have been added, that differ from the dashed curve only in the value of $\varepsilon_{1\infty}$ and allow to graphically identify a region (shading) that "bounds" the experimental curves below 500 nm. The NIR refractive index corresponding to these curves is shown directly in Figure 4.50 (c).

As already discussed in section 4.1.5 for the FZ24 sequence, despite the limitations of the model in describing the behaviour of a complex system such as RNA/DNA

SAMs, a good agreement between simulation and experiment was obtained. Thus, the overlap between the simulations and the experimental data provided us information on DNA absorption (UV region) and film organization with respect to both the SAM/gold interface ($\delta\Psi$) and the film refractive index ($\delta\Delta$) (Vis-NIR region).

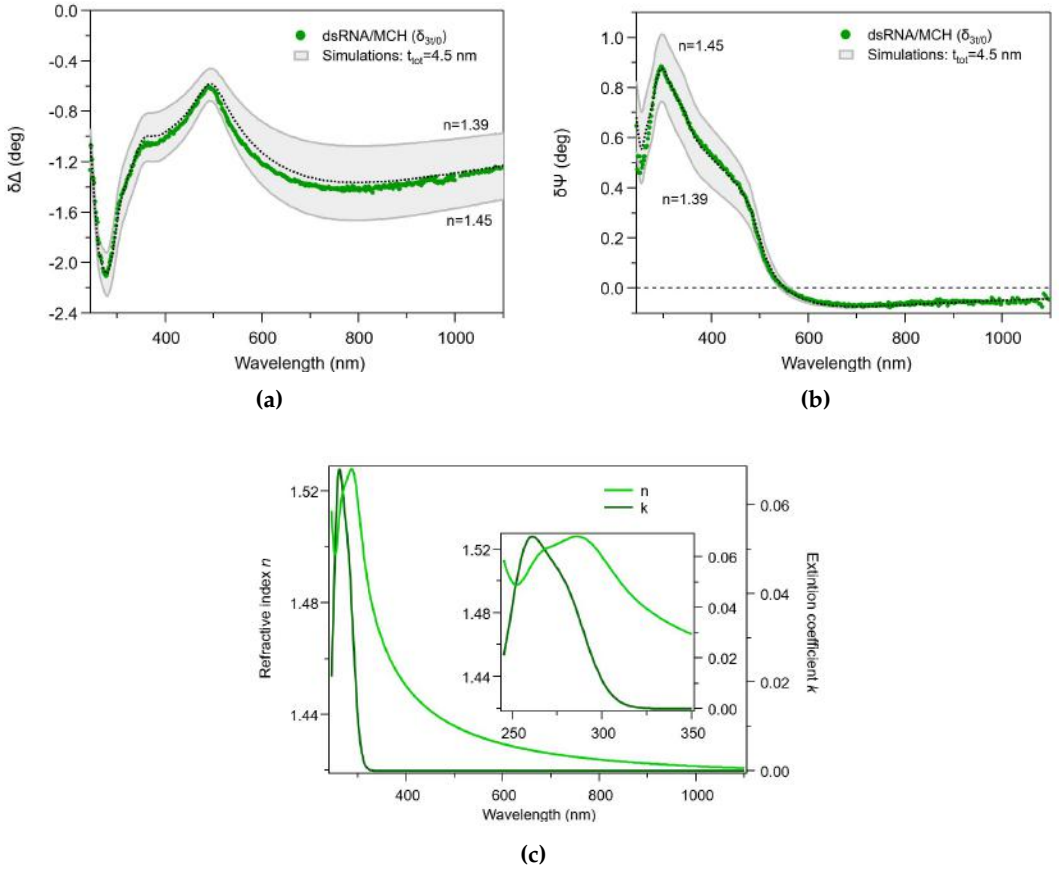

Figure 4.50 – *Comparison between SE experiments and simulations for RdRp-Helicase dsRNA/MCH films. (a) $\delta\Delta_{3t/0}$ experimental data (circles) vs calculated curves (grey region). (b) $\delta\Psi_{3t/0}$ experimental data (circles) vs calculated curves (grey region). For reference, calculated curves for n(1300 nm)=1.42 are reported too (black dashed lines). (c) Refractive index and extinction coefficient related to the GenOsc layer representing dsRNA/MCH SAMs (n(1300 nm)=1.42).*

Focussing on the DNA absorption, for both pDNA/MCH and dsDNA/MCH SAMs, two Gaussian oscillators account for the narrow UV dips with position in general agreement with the literature and previous simulations on FZ24 SAMs. The SE features of the DNA absorption slightly changes after hybridization (Fig. 4.48), showing a small red-shift or even a small broadening/intensity increase. In our simulations, small shifts of the Gaussian peak positions were applied to reproduce the red-shift of the absorption feature upon hybridization.

We can observe that the slight increase in intensity of the SE features upon hybridization does not account for the increased number of adsorbing molecules following deposition of tDNA/RNA. This finding, together with the fact that the increase in optical thickness (detected by SE in NIR region) is definitely lower than the increase

in mass/area detected by QCM-D measurements after hybridization, suggests the occurrence of hypochromism for RdRp DNA films on surfaces as already observed for FZ24 films.

Conclusions

In this thesis, we have studied ultrathin films of DNA chemisorbed on gold and their hybridization with complementary strands through a multi-technique approach.
This research was motivated by a strong interest towards the search for new biological detection methods, paramount for example for SARS-CoV-2 mass tests. In particular, our goal is the development of an efficient, rapid, and inexpensive device able to detect, through the same platform, both viral or toxin-producing nucleic acids and pathological analytes. We focused on the fabrication and the analysis of the sensing performance of a DNA-based oligonucleotide biosensor, leaving for the future the study of immunological detection.
We studied the DNA films through optical spectroscopy (spectroscopic ellipsometry, surface plasmon enhanced ellipsometry), X-rays photoelectron spectroscopy and mechanical methods (atomic force microscopy, quartz crystal microbalance) in order to obtain a complete characterization of the biological system. With regard to the experimental methods, the activity allowed for the design of a home-built set-up for SPEE experiments, technique not present so far at the Department of Physics. Moreover, concerning the SE and AFM measurements, the optimization of the set-ups and, for SE, of the flow cell system, has been performed.

The first part of the activity focussed on the optimization of the experimental protocols and set-up, studying a model synthetic DNA sequence, FZ24. We optimized the preparation protocols of the sensing platform, studying the effect of parameters like the ionic strength of the buffer solution and the pDNA incubation time.
Firstly, the deposition of pDNA SAMs has been studied in-depth, finding that a high ionic strength (1 M NaCl TE buffer) and a long immobilization time (24 h) help to obtain compact, dense, and "thick" films. However, particular attention has to be paid to the compactness of the films: a too compact layer could prevent an efficient hybridization due to the low inter-strand free space. For this reason, the immobilization time has been limited to 3 hours.
Subsequently, the effect of using a molecular spacer (MCH) on the resulting SAM organization was studied. The comparison between a two-step (pDNA + tDNA) and a three-step (pDNA + MCH + tDNA) process indicated that mixed pDNA/MCH films allow for an easier detection of the hybridization process.
The second part of the activity exploited the previous results to study the hybridization process on optimized DNA films.

Real-time experiments performed with QCM-D, SE and SPEE allowed monitoring film variations at each deposition step; a kinetic analysis of molecular deposition was performed through fitting of QCM-D results. Mass coverage results obtained from QCM-D analysis indicated an average nearest-neighbour distance of 15 $\dot{A}$ for pDNA films, 5.3 $\dot{A}$ for mixed films and 22 $\dot{A}$ for tDNA molecules. This finding suggests that one over two adsorbed single-strand DNA are hybridized by target DNA and hybridization forms a dense layer of double helix DNA, oriented almost perpendicular to the surface.
By AFM nanolithography we could monitor the evolution of film thickness at each stage of deposition. The thickness of pDNA was found to be much lower than the length of the extended molecule, suggesting a quite disordered arrangement on the gold surface. The increase of the SAM thickness upon exposure to MCH suggests a reorganization of pDNA SAMs due to the introduction of the spacer molecule, while the further thickness increase upon incubation in tDNA indicates the success of the hybridization process. These results were supported and also confirmed by XPS measurements, that showed an increase of surface coverage at each deposition step. SE measurements confirmed previous results and allowed for the detection of differences in the optical behaviour between the single-strand and double-strand DNA films, providing an extremely fast (differently from AFM and XPS), spectroscopic (differently from QCM-D and AFM) and not-invasive (differently from XPS) method to detect hybridization.
Analysis of UV absorptions and optical thickness, before and after hybridization, corroborated by comparison with QCM data, allowed to identify, in label-free mode, the induced hypochromism of the DNA absorbers. While hypochromism (or the reverse phenomenon of hyperchromism) has been commonly observed in many types of experiments dealing with molecular solutions, to our knowledge our results represent the first characterization of this phenomenon for DNA monolayers immobilized on a surface.
The third part of the activity focused on the limit of detection, the selectivity and the re-usability of this sensing platform developed for the recognition of a target oligonucleotide sequence. We investigated the limit of detection through different methods, finding that the SPEE configuration allowed for detection down to a 10 nM tDNA solution. Selectivity is also critical for a diagnostic device: incubation in a solution of non-complementary sequences resulted in no changes in the film, whereas labelled target strands allowed us to effectively correlate the detected changes to the hybridization process. Then, the re-usability of the device was tested: the efficiency resulted unchanged up to 5 cycles of hybridization/denaturation and upon at least one-week storage in dry conditions.

The experience gained was finally exploited to study a COVID-19-related sequence, the RdRp-Helicase. In fact, the key feature of our sensing approach is that the receptor/analyte interaction (i.e., the hybridization between probe DNA and target DNA strands) can be detected unequivocally through a spectroscopic fingerprint by

in-situ and real-time spectroscopic ellipsometry measurements. All results obtained for the FZ24 sequence were confirmed from the experiments with the RdRp-Helicase sequence, reinforcing the robustness of our results.

In conclusion, spectroscopic ellipsometry has proven to be a suitable method to effectively monitor the sequence recognition process, through non-destructive measurements also in lack of labelling. The difference spectra method can be applied independently of the substrate and is also practicable in micro-spectrometry experiments applied to sensor arrays. Combining SE measurements with QCM-D data obtained under comparable conditions also allows calibration of $\delta\Delta$ data and paves the way for quantification of the assay. Pathogen detection, DNA computation, and DNA memory storage devices are just a few of the areas that could benefit from a device that can very quickly detect label-free DNA hybridization.

List of Figures

Acronyms

AFM: Atomic Force Microscope
BE: Binding Energy
COVID: Corona-Virus Disease
DDI: Direct DNA immobilization
DNA: Deoxyribonucleic Acid
dsDNA: double strand DNA
EMA: Effective Medium Approximation
ESCA: Electron Spectroscopy for Chemical Analysis
GenOsc: General Oscillator Layer
GL: Gaussian/Lorentzian
KE: Kinetic Energy
HDA: Hemispherical Analyzer
IR: Infra-Red
LSPR: Localized Surface Plasmon Resonance
miRNA: microRNA
NIR: Near Infra-Red
PE: Pass Energy
pDNA: probe DNA
PSD: Polarization State Detector
PSG: Polarization State Generator
QCM-D: Quartz Crystal Microbalance with Dissipation
QI: Quantitative Imaging
RAE: Rotating Analyzer Ellipsometer
RCE: Rotating Compensator Ellipsometer
RNA: Ribonucleic Acid
RSF: Relative Sensitivity Factor
RT-PCR: Reverse Transcriptase-Polymerase Chain Reaction
SAM: Self-Assembled Monolayer
SARS-CoV-2: Severe Acute Respiratory Syndrome CoronaVirus 2
SE: Spectroscopic Ellipsometry
SERS: Surface-Enhanced Raman Scattering
SPEE: Surface Plasmon Enhanced Ellipsometry
SPR: Surface Plasmon Resonance
ssDNA: single strand DNA

tDNA: target DNA
TIRE: Total Internal Reflection Ellipsometry
UHV: Ultra High Vacuum
UV: Ultra Violet
Vis: Visible
XPS: X-Rays Photoelectron Spectroscopy

Bibliography

[1] Y. Orooji, H. Sohrabi, N. Hemmat, F. Oroojalian, B. Baradaran, A. Mokhtarzadeh, M. Mohaghegh, H. Karimi-Maleh, *Nano-Micro Letters* **2020**, *13*, 18.

[2] D. Campos-Ferreira, V. Visani, C. Córdula, G. Nascimento, L. Montenegro, H. Schindler, I. Cavalcanti, *Biochemical Engineering Journal* **2021**, *176*, 108200.

[3] M. Drobysh, A. Ramanaviciene, R. Viter, A. Ramanavicius, *Micromachines* **2021**, *12*, DOI 10.3390/mi12040390.

[4] B. D. Kevadiya, J. Machhi, J. Herskovitz, M. D. Oleynikov, W. R. Blomberg, N. Bajwa, D. Soni, S. Das, M. Hasan, M. Patel, A. M. Senan, S. Gorantla, J. McMillan, B. Edagwa, R. Eisenberg, C. B. Gurumurthy, S. P. M. Reid, C. Punyadeera, L. Chang, H. E. Gendelman, *Nature Materials* **2021**, *20*, 593–605.

[5] C. Hwang, N. Park, E. S. Kim, M. Kim, S. D. Kim, S. Park, N. Y. Kim, J. H. Kim, *Biosensors and Bioelectronics* **2021**, *185*, 113177.

[6] E. D. Wold, R. McBride, J. Y. Axup, S. A. Kazane, V. V. Smider, *Bioconjugate Chemistry* **2015**, *26*, 807–811.

[7] E. Cesewski, B. N. Johnson, *Biosensors and Bioelectronics* **2020**, *159*, 112214.

[8] G. Pinto, P. Parisse, I. Solano, P. Canepa, M. Canepa, L. Casalis, O. Cavalleri, *Soft Matter* **2019**, *15*, 2463–2468.

[9] G. Pinto, P. Canepa, C. Canale, O. Cavalleri, *Materials* **2020**, *13*, 2888.

[10] H. Karimi-Maleh, Y. Orooji, F. Karimi, M. Alizadeh, M. Baghayeri, J. Rouhi, S. Tajik, H. Beitollahi, S. Agarwal, V. K. Gupta, S. Rajendran, A. Ayati, L. Fu, A. L. Sanati, B. Tanhaei, F. Sen, M. Shabani-Nooshabadi, P. N. Asrami, A. Al-Othman, *Biosensors and Bioelectronics* **2021**, *184*, 113252.

[11] J. Miao, K. Du, X. Li, X. Xu, X. Dong, J. Fang, W. Cao, Q. Wei, *Biosensors and Bioelectronics* **2021**, *171*, 112713.

[12] B. G. Andryukov, N. N. Besednova, R. V. Romashko, T. S. Zaporozhets, T. A. Efimov, *Biosensors* **2020**, *10*, DOI 10.3390/bios10020011.

[13] M. Birkholz, P. Glogener, F. Glös, T. Basmer, L. Theuer, *Micromachines* **2016**, *7*, DOI 10.3390/mi7100183.

[14] Z. Xu, L.-l. Long, Y.-q. Chen, M.-L. Chen, Y.-H. Cheng, *Food Chemistry* **2021**, *338*, 128039.

[15] N. Chu, Q. Liang, W. Hao, Y. Jiang, P. Liang, R. J. Zeng, *Chemical Engineering Journal* **2021**, *404*, 127053.

[16] R. W. Peeling, K. K. Holmes, D. Mabey, A. Ronald, *Sexually Transmitted Infections* **2006**, *82*, v1–v6.

[17] S. Lamping, C. Buten, B. J. Ravoo, *Accounts of Chemical Research* **2019**, *52*, 1336–1346.

[18] I. Solano, P. Parisse, F. Gramazio, O. Cavalleri, G. Bracco, M. Castronovo, L. Casalis, M. Canepa, *Physical Chemistry Chemical Physics* **2015**, *17*, 28774–28781.

[19] M. Negrito, M. B. Elinski, N. Hawthorne, M. P. Pedley, M. Han, M. Sheldon, R. M. Espinosa-Marzal, J. D. Batteas, *Langmuir* **2021**, *37*, PMID: 34375532, 9996–10005.

[20] C. Chen, J. Wang, *Analyst* **2020**, *145*, 1605–1628.

[21] M. M. Hassan, F. S. Sium, F. Islam, S. M. Choudhury, *Sensing and Bio-Sensing Research* **2021**, *33*, 100429.

[22] S. Joshi, P. Pellacani, T. A. van Beek, H. Zuilhof, M. W. Nielen, *Sensors and Actuators B: Chemical* **2015**, *209*, 505–514.

[23] C. Novara, A. Chiadò, N. Paccotti, S. Catuogno, C. L. Esposito, G. Condorelli, V. De Franciscis, F. Geobaldo, P. Rivolo, F. Giorgis, *Faraday Discussions* **2017**, *205*, 271–289.

[24] D. M. Kim, J. S. Park, S.-W. Jung, J. Yeom, S. M. Yoo, *Sensors* **2021**, *21*, DOI 10.3390/s21093191.

[25] H.-M. Kim, J.-H. Park, S.-K. Lee, *Sensors and Actuators A: Physical* **2021**, *331*, 112982.

[26] D. Rho, C. Breaux, S. Kim, *Sensors* **2020**, *20*, DOI 10.3390/s20205901.

[27] N. C. H. Le, V. Gubala, R. P. Gandhiraman, C. Coyle, S. Daniels, D. E. Williams, *Analytical and Bioanalytical Chemistry* **2010**, *398*, 1927–1936.

[28] A. Abbas, M. J. Linman, Q. Cheng, *Biosensors and Bioelectronics* **2011**, *26*, 1815–1824.

[29] I. Plikusiene, V. Maciulis, A. Ramanaviciene, Z. Balevicius, E. Buzavaite-Verteliene, E. Ciplys, R. Slibinskas, M. Simanavicius, A. Zvirbliene, A. Ramanavicius, *Journal of Colloid and Interface Science* **2021**, *594*, 195–203.

[30] C. Knoglinger, A. Zich, L. Traxler, K. Poslednì, G. Friedl, B. Ruttmann, A. Schorpp, K. Müller, M. Zimmermann, H. J. Gruber, *Biosensors and Bioelectronics* **2018**, *99*, 684–690.

[31] I. Solano, P. Parisse, O. Cavalleri, F. Gramazio, L. Casalis, M. Canepa, *Beilstein Journal of Nanotechnology* **2016**, *7*, 544–553.

[32] H. Eto, N. Soga, H. G. Franquelim, P. Glock, A. Khmelinskaia, L. Kai, M. Heymann, H. Noji, P. Schwille, *ACS Applied Materials & Interfaces* **2019**, *11*, PMID: 31136146, 21372–21380.

[33] H. Haraguchi, N. Frese, A. Gölzhäuser, H. Takei, *RSC Adv.* **2019**, *9*, 9565–9576.

[34] J. Telegdi, *Materials* **2020**, *13*, DOI 10.3390/ma13225089.

[35] P. Canepa, G. Gonella, G. Pinto, V. Grachev, M. Canepa, O. Cavalleri, *The Journal of Physical Chemistry C* **2019**, *123*, 16843–16850.

[36] M. Timpel, M. V. Nardi, B. Wegner, G. Ligorio, L. Pasquali, J. Hildebrandt, M. Pätzel, S. Hecht, H. Ohta, N. Koch, *Advanced Materials Interfaces* **2020**, *7*, 1902114.

[37] N. Faucheux, R. Schweiss, K. Lützow, C. Werner, T. Groth, *Biomaterials* **2004**, *25*, 2721–2730.

[38] X. Jiang, D. A. Bruzewicz, A. P. Wong, M. Piel, G. M. Whitesides, *Proceedings of the National Academy of Sciences* **2005**, *102*, 975–978.

[39] A. Ulman, *Chemical Reviews* **1996**, *96*, PMID: 11848802, 1533–1554.

[40] N. Kohler, G. E. Fryxell, M. Zhang, *Journal of the American Chemical Society* **2004**, *126*, PMID: 15186157, 7206–7211.

[41] C. Haensch, S. Hoeppener, U. S. Schubert, *Chem. Soc. Rev.* **2010**, *39*, 2323–2334.

[42] L. Liu, A. Mei, T. Liu, P. Jiang, Y. Sheng, L. Zhang, H. Han, *Journal of the American Chemical Society* **2015**, *137*, PMID: 25594109, 1790–1793.

[43] L. H. Dubois, R. G. Nuzzo, *Annual Review of Physical Chemistry* **1992**, *43*, 437–463.

[44] G. E. Poirier, *Chemical Reviews* **1997**, *97*, 1117–1128.

[45] J. C. Love, L. A. Estroff, J. K. Kriebel, R. G. Nuzzo, G. M. Whitesides, *Chemical Reviews* **2005**, *105*, 1103–1170.

[46] R. G. Nuzzo, D. L. Allara, *Journal of the American Chemical Society* **1983**, *105*, 4481–4483.

[47] P. E. Laibinis, G. M. Whitesides, D. L. Allara, Y. T. Tao, A. N. Parikh, R. G. Nuzzo, *Journal of the American Chemical Society* **1991**, *113*, 7152–7167.

[48] F. Schreiber, **2004**, *16*, R881–R900.

[49] C. D. Bain, E. B. Troughton, Y. T. Tao, J. Evall, G. M. Whitesides, R. G. Nuzzo, *Journal of the American Chemical Society* **1989**, *111*, 321–335.

[50] D. S. Karpovich, G. J. Blanchard, *Langmuir* **1994**, *10*, 3315–3322.

[51] W. Pan, C. J. Durning, N. J. Turro, *Langmuir* **1996**, *12*, 4469–4473.

[52] R. Subramanian, V. Lakshminarayanan, *Electrochimica Acta* **2000**, *45*, 4501–4509.

[53] F. Schreiber, *Progress in Surface Science* **2000**, *65*, 151–257.

[54] W. J. Brittain, T. Brandsetter, O. Prucker, J. Rühe, *ACS Applied Materials & Interfaces* **2019**, *11*, 39397–39409.

[55] Q. Xiao, J. Wu, P. Dang, H. Ju, *Analytica Chimica Acta* **2018**, *1032*, 130–137.

[56] S. Yu, T. Chen, Q. Zhang, M. Zhou, X. Zhu, *The Analyst* **2020**, *145*, 3481–3489.

[57] L.-P. Jia, R.-J. Zhao, Z. Feng, M.-Y. Wang, R.-N. Ma, W.-L. Jia, L. Shang, W. Zhang, Q.-W. Xue, H.-S. Wang, *Sensors and Actuators B: Chemical* **2021**, 130849.

[58] A. F. Adedeji Olulana, M. A. Soler, M. Lotteri, H. Vondracek, L. Casalis, D. Marasco, M. Castronovo, S. Fortuna, *International Journal of Molecular Sciences* **2021**, *22*, DOI 10.3390/ijms22020812.

[59] P. Miao, Y. Tang, *Analytical Chemistry* **2019**, *91*, PMID: 31674765, 15187–15192.

[60] A. Sassolas, B. D. Leca-Bouvier, L. J. Blum, **2008**, 31.

[61] A. Rabti, R. Zayani, M. Meftah, I. Salhi, N. Raouafi, *Microchimica Acta* **2020**, *187*, 635.

[62] S. Qian, M. Lin, W. Ji, H. Yuan, Y. Zhang, Z. Jing, J. Zhao, *ACS Sensors* **2018**, 7.

[63] Q. Jiang, Y. Wang, Y. Hao, L. Juan, M. Teng, X. Zhang, M. Li, G. Wang, Y. Liu, *Nucleic Acids Research* **2008**, *37*, D98–D104.

[64] G. Qiu, Z. Gai, Y. Tao, J. Schmitt, G. A. Kullak-Ublick, J. Wang, *ACS Nano* **2020**, *14*, 5268–5277.

[65] Y. Yang, S. Wang, Z. Zhou, R. Zhang, H. Shen, J. Song, P. Su, Y. Yang, *Biochemical Engineering Journal* **2018**, *137*, 108–115.

[66] H. Wang, M. Liu, W. Bai, H. Sun, Y. Li, H. Deng, *Sensors and Actuators B: Chemical* **2019**, *284*, 236–242.

[67] S. Cagnin, M. Caraballo, C. Guiducci, P. Martini, M. Ross, M. SantaAna, D. Danley, T. West, G. Lanfranchi, *Sensors* **2009**, *9*, 3122–3148.

[68] M. Trotter, N. Borst, R. Thewes, F. von Stetten, *Biosensors and Bioelectronics* **2020**, *154*, 112069.

[69] A. Kowalczyk, *Current Opinion in Electrochemistry* **2020**, *23*, 36–41.

[70] E. Seymour, G. G. Daaboul, X. Zhang, S. M. Scherr, N. L. Ünlü, J. H. Connor, M. S. Ünlü, *Analytical Chemistry* **2015**, *87*, 10505–10512.

[71] X. Zhang, P. Du, X. Cui, G. Chen, Y. Wang, Y. Zhang, A. M. A. El-Aty, A. Hac, *Science of the Total Environment* **2020**, 9.

[72] H. H. Nguyen, J. Park, S. Kang, M. Kim, *Sensors* **2015**, *15*, 10481–10510.

[73] H. Liu, J. Shen, W. Liu, Y. Niu, G. Jin, *Journal of Vacuum Science & Technology B* **2020**, *38*, 024002.

[74] B. D. Ventura, M. Cennamo, A. Minopoli, R. Campanile, S. B. Censi, D. Terracciano, G. Portella, R. Velotta, *ACS Sensors* **2020**, *5*, 3043–3048.

[75] I. Mannelli, M. Minunni, S. Tombelli, M. Mascini, *Biosensors and Bioelectronics* **2003**, *18*, 129–140.

[76] X. Mao, L. Yang, X.-L. Su, Y. Li, *Biosensors and Bioelectronics* **2006**, *21*, 1178–1185.

[77] Y. Tian, P. Zhu, Y. Chen, X. Bai, L. Du, W. Chen, C. Wu, P. Wang, *Sensors and Actuators B: Chemical* **2021**, *346*, 130446.

[78] P. Mignon, S. Loverix, J. Steyaert, P. Geerlings, *Nucleic Acids Research* **2005**, *33*, 1779–1789.

[79] H. Clausen-Schaumann, M. Rief, C. Tolksdorf, H. E. Gaub, *Biophysical Journal* **2000**, *78*, 1997–2007.

[80] X. Wang, H. J. Lim, A. Son, *Environmental Health and Toxicology* **2014**, *29*, 8.

[81] T. Yamada, H. Fukutome, *Biopolymers* **1968**, *6*, 43–54.

[82] T. Inagaki, R. N. Hamm, E. T. Arakawa, L. R. Painter, *The Journal of Chemical Physics* **1974**, *61*, 4246–4250.

[83] V. A. Bloomfield, D. M. Crothers, I. J. Tinoco, *Nucleic acids: structures, properties and functions*, 1st ed., University Science Books, Herndon, VA., **2000**, p. 672.

[84] A. Lopiccolo, B. Shirt-Ediss, E. Torelli, A. F. A. Olulana, M. Castronovo, H. Fellermann, N. Krasnogor, *Nature Communications* **2021**, *12*, 4861.

[85] A. Anžel, D. Heider, G. Hattab, *Computational and Structural Biotechnology Journal* **2021**, *19*, 4904–4918.

[86] B. R. Aryal, D. R. Ranasinghe, C. Pang, A. E. F. Ehlert, T. R. Westover, J. N. Harb, R. C. Davis, A. T. Woolley, *ACS Applied Nano Materials* **2021**, *4*, 9094–9103.

[87] S. N. Sarangi, B. C. Behera, N. K. Sahoo, S. K. Tripathy, *Biosensors and Bioelectronics* **2021**, *190*, 113402.

[88] M. A. F. Al-Husainy, B. Al-Shargabi, S. Aljawarneh, *Computers and Electrical Engineering* **2021**, *95*, 107418.

[89] M. Kuscu, H. Ramezani, E. Dinc, S. Akhavan, O. B. Akan, *Scientific Reports* **2021**, *11*, 19600.

[90] C. Zong, X. Jin, J. Liu, *Trends in Environmental Analytical Chemistry* **2021**, *32*, e00143.

[91] A. Gangrade, N. Stephanopoulos, D. Bhatia, *Nanoscale* **2021**, *13*, 16834–16846.

[92] P. H. Guedes, J. G. Brussasco, A. C. Moço, D. D. Moraes, J. M. Flauzino, L. F. Luz, M. T. Almeida, M. M. Soares, R. J. Oliveira, J. M. Madurro, A. G. Brito-Madurro, *Talanta* **2021**, *235*, 122694.

[93] B. Tinland, A. Pluen, J. Sturm, G. Weill, **1997**, 3.

[94] C. G. Baumann, S. B. Smith, V. A. Bloomfield, C. Bustamante, *Proceedings of the National Academy of Sciences* **1997**, *94*, 6185–6190.

[95] I. Tinoco, C. Bustamante, *Journal of Molecular Biology* **1999**, *293*, 271–281.

[96] A. Rich, *Journal of Biological Chemistry* **2006**, *281*, 7693–7696.

[97] E. A. Lesnik, S. M. Freier, *Biochemistry* **1995**, *34*, PMID: 7662660, 10807–10815.

[98] N. N. Shaw, D. P. Arya, *Biochimie* **2008**, *90*, Targeting DNA Part 1, 1026–1039.

[99] J.-H. Liu, K. Xi, X. Zhang, L. Bao, X. Zhang, Z.-J. Tan, *Biophysical Journal* **2019**, *117*, 74–86.

[100] C. Zhang, H. Fu, Y. Yang, E. Zhou, Z. Tan, H. You, X. Zhang, *Biophysical Journal* **2019**, *116*, 196–204.

[101] H. Kimura-Suda, D. Y. Petrovykh, M. J. Tarlov, L. J. Whitman, *Journal of the American Chemical Society* **2003**, *125*, 9014–9015.

[102] H. Chen, S. P. Meisburger, S. A. Pabit, J. L. Sutton, W. W. Webb, L. Pollack, *Proceedings of the National Academy of Sciences* **2012**, *109*, 799–804.

[103] S. Guilbaud, L. Salomé, N. Destainville, M. Manghi, C. Tardin, *Physical Review Letters* **2019**, *122*, 028102.

[104] T. Herne, M. Tarlov, *J. Am. Chem. Soc.* **1997**, *119*, 8916–8920.

[105] K. Castelino, B. Kannan, A. Majumdar, *Langmuir* **2005**, *21*, 1956–1961.

[106] Z. Li, T. Niu, Z. Zhang, G. Feng, S. Bi, *The Analyst* **2012**, *137*, 1680–1691.

[107] S. Moses, S. H. Brewer, L. B. Lowe, S. E. Lappi, L. B. G. Gilvey, M. Sauthier, R. C. Tenent, D. L. Feldheim, S. Franzen, *Langmuir* **2004**, *20*, 11134–11140.

[108] A. B. Steel, T. M. Herne, M. J. Tarlov, *Analytical Chemistry* **1998**, *70*, 4670–4677.

[109] S. D. Keighley, P. Li, P. Estrela, P. Migliorato, *Biosensors and Bioelectronics* **2008**, *23*, 1291–1297.

[110] R. Georgiadis, K. P. Peterlinz, A. W. Peterson, *Journal of the American Chemical Society* **2000**, *122*, 3166–3173.

[111] A. W. Peterson, R. J. Heaton, R. M. Georgiadis, *Nucleic Acids Research* **2001**, *29*, 5163–5168.

[112] L. K. Wolf, Y. Gao, R. M. Georgiadis, *Langmuir* **2004**, *20*, 3357–3361.

[113] K. S. Kumar, R. Naaman, *Langmuir* **2012**, *28*, 14514–14517.

[114] D. Y. Petrovykh, H. Kimura-Suda, L. J. Whitman, M. J. Tarlov, *Journal of the American Chemical Society* **2003**, *125*, 5219–5226.

[115] C. Howell, H. Hamoudi, M. Zharnikov, *Biointerphases* **2013**, *8*, 6.

[116] K. Spaeth, A. Brecht, G. Gauglitz, *Journal of Colloid and Interface Science* **1997**, *196*, 128–135.

[117] J. N. Hilfiker, G. K. Pribil, R. Synowicki, A. C. Martin, J. S. Hale, *Surface and Coatings Technology* **2019**, *357*, 114–121.

[118] D. Rosu, P. Petrik, G. Rattmann, M. Schellenberger, U. Beck, A. Hertwig, *Thin Solid Films* **2014**, *571*, 6th International Conference on Spectroscopic Ellipsometry (ICSE-VI), 601–604.

[119] M. Canepa in *Surface Science Techniques*, *Vol. 51*, (Eds.: G. Bracco, B. Holst), Series Title: Springer Series in Surface Sciences, Springer Berlin Heidelberg, Berlin, Heidelberg, **2013**, pp. 99–135.

[120] M. Prato, R. Moroni, F. Bisio, R. Rolandi, L. Mattera, O. Cavalleri, M. Canepa, *The Journal of Physical Chemistry C* **2008**, *112*, 3899–3906.

[121] C. Toccafondi, M. Prato, G. Maidecchi, A. Penco, F. Bisio, O. Cavalleri, M. Canepa, *Journal of Colloid and Interface Science* **2011**, *364*, 125–132.

[122] H. Fujiwara, *Spectroscopic ellipsometry: Principles and applications.* 1st ed., John Wiley & Sons, Chichester, England, **2007**.

[123] M. Born, E. Wolf, A. B. Bhatia, P. C. Clemmow, D. Gabor, A. R. Stokes, A. M. Taylor, P. A. Wayman, W. L. Wilcock, *Principles of Optics: Electromagnetic Theory of Propagation, Interference and Diffraction of Light*, 7th ed., Cambridge University Press, **1999**.

[124] H. G. Tompkins, W. A. McGahan, *Spectroscopic ellipsometry and reflectometry : a user's guide*, New York (N.Y.) : Wiley, **1999**.

[125] R. M. A. Azzam, N. M. Bashara, *Ellipsometry and polarized light.* North-Holland, Amsterdam-New York, **1987**.

[126] J. R. Krivacic, D. W. Urry, *Analytical Chemistry* **1970**, *42*, 596–599.

[127] T. Berlind, G. K. Pribil, D. Thompson, J. A. Woollam, H. Arwin, *physica status solidi (c)* **2008**, *5*, 1249–1252.

[128] D. A. G. Bruggeman, *Annalen der Physik* **1935**, *416*, 636–664.

[129] I. Plikusiene, V. Maciulis, O. Graniel, M. Bechelany, S. Balevicius, V. Vertelis, Z. Balevicius, A. Popov, A. Ramanavicius, A. Ramanaviciene, *J. Mater. Chem. C* **2021**, *9*, 1345–1352.

[130] P. Westphal, A. Bornmann, *Sensors and Actuators B: Chemical* **2002**, *84*, 278–282.

[131] H. Arwin, M. Poksinski, K. Johansen, *Applied Optics* **2004**, *43*, 3028.

[132] A. G. Al-Rubaye, A. Nabok, A. Tsargorodska, *Sensing and Bio-Sensing Research* **2017**, *12*, 30–35.

[133] D. Hemzal, Y. R. Kang, J. Dvořák, T. Kabzinski, K. Kubiček, Y. D. Kim, J. Humliček, *Applied Spectroscopy* **2019**, *73*, 261–270.

[134] V. H. Pérez-Luna in *Surfaces and Interfaces for Biomaterials*, (Ed.: P. Vadgama), Woodhead Publishing Series in Biomaterials, Woodhead Publishing, **2005**, pp. 248–270.

[135] K. Peterlinz, R. Georgiadis, *Optics Communications* **1996**, *130*, 260–266.

[136] H. Arwin, M. Poksinski, K. Johansen, *physica status solidi (a)* **2008**, *205*, 817–820.

[137] W. Chegal, H. M. Cho, Y. J. Cho, Y. P. Kim, H. S. Kim in, Optics East 2005, (Eds.: M. S. Islam, A. K. Dutta), Boston, MA, **2005**, 60081G.

[138] N. F. Murat, W. M. Mukhtar, A. R. A. Rashid, K. A. Dasuki, A. A. R. A. Yussuf, **2016**, 244–247.

[139] G. Binnig, C. F. Quate, C. Gerber, *Physical Review Letters* **1986**, *56*, 930–933.

[140] J. E. Sader, J. W. M. Chon, P. Mulvaney, *Review of Scientific Instruments* **1999**, *70*, 3967–3969.

[141] J. E. Sader, J. A. Sanelli, B. D. Adamson, J. P. Monty, X. Wei, S. A. Crawford, J. R. Friend, I. Marusic, P. Mulvaney, E. J. Bieske, *Review of Scientific Instruments* **2012**, *83*, 103705.

[142] I. M. Malovichko, *Bulletin of the Russian Academy of Sciences: Physics* **2013**, *77*, 972–974.

[143] J. E. Sader, J. Lu, P. Mulvaney, *Review of Scientific Instruments* **2014**, *85*, 113702.

[144] Hertz, H., *ournal für die angewandte Mathematik* **1881**, *92*, 156–171.

[145] K. Johnson, *Contact Mechanics*, Cambridge, UK, **1985**, 452 pp.

[146] F. Rico, P. Roca-Cusachs, N. Gavara, R. Farré, M. Rotger, D. Navajas, *Physical Review E* **2005**, *72*, 021914.

[147] S. Xu, G.-Y. Liu, *Langmuir* **1997**, *13*, 127–129.

[148] G.-Y. Liu, S. Xu, Y. Qian, *Accounts of Chemical Research* **2000**, *33*, 457–466.

[149] J. Liang, G. Scoles, *Langmuir* **2007**, *23*, 6142–6147.

[150] M. Castronovo, A. Lucesoli, P. Parisse, A. Kurnikova, A. Malhotra, M. Grassi, G. Grassi, B. Scaggiante, L. Casalis, G. Scoles, *Nature Communications* **2011**, *2*, DOI 10.1038/ncomms1296.

[151] A. Adedeji, E. Ambrosetti, L. Casalis, C. M., **2018**, *1811*, (Ed.: G. Zuccheri), 151–162.

[152] J. Yeh, I. Lindau, *Atomic Data and Nuclear Data Tables* **1985**, *32*, 1–155.

[153] J. Yeh, *Atomic Calculation of Photoionization Cross-sections and Asymmetry Parameters*, Gordon & Breach Science, Publishers, **1993**.

[154] S. Evans, *Surface and Interface Analysis* **1991**, *17*, 85–93.

[155] S. Doniach, M. Sunjic, *Journal of Physics C: Solid State Physics* **1970**, *3*, 285–291.

[156] J. P J, K. Prabakaran, J. Luo, D. H. M G, *Sensors and Actuators A: Physical* **2021**, *331*, 113020.

[157] G. Sauerbrey, *Zeitschrift für Physik* **1959**, *155*, 206–222.

[158] K. K. Kanazawa, J. G. Gordon, *Analytical Chemistry* **1985**, *57*, 1770–1771.

[159] P. Gupta, K. Loos, A. Korniakov, C. Spagnoli, M. Cowman, A. Ulman, *Angewandte Chemie International Edition* **2004**, *43*, 520–523.

[160] V. M. Corman, O. Landt, M. Kaiser, R. Molenkamp, A. Meijer, D. K. Chu, T. Bleicker, S. Brünink, J. Schneider, M. L. Schmidt, D. G. Mulders, B. L. Haagmans, B. van der Veer, S. van den Brink, L. Wijsman, G. Goderski, J.-L. Romette, J. Ellis, M. Zambon, M. Peiris, H. Goossens, C. Reusken, M. P. Koopmans, C. Drosten, *Eurosurveillance* **2020**, *25*, DOI 10.2807/1560-7917.ES.2020.25.3.2000045.

[161] J. F.-W. Chan, C. C.-Y. Yip, K. K.-W. To, T. H.-C. Tang, S. C.-Y. Wong, K.-H. Leung, A. Y.-F. Fung, A. C.-K. Ng, Z. Zou, H.-W. Tsoi, G. K.-Y. Choi, A. R. Tam, V. C.-C. Cheng, K.-H. Chan, O. T.-Y. Tsang, K.-Y. Yuen, *Journal of Clinical Microbiology* **2020**, *58*, (Ed.: A. J. McAdam), DOI 10.1128/JCM.00310-20.

[162] R. Levicky, T. M. Herne, M. J. Tarlov, S. K. Satija, *Journal of the American Chemical Society* **1998**, *120*, 9787–9792.

[163] Y. Song, Y. Liu, M. Yang, B. Zhang, Z. Li, *Applied Surface Science* **2006**, *252*, 5693–5699.

[164] A. Bosco, F. Bano, P. Parisse, L. Casalis, A. DeSimone, C. Micheletti, *Nanoscale* **2012**, *4*, 1734.

[165] P. Gong, C.-Y. Lee, L. J. Gamble, D. G. Castner, D. W. Grainger, *Analytical Chemistry* **2006**, *78*, 3326–3334.

[166] M. Prato, *PhD Thesis - PhD School in Chemistry and Materials Science and Technology* **2005**.

[167] X. Su, Y.-J. Wu, W. Knoll, *Biosensors and Bioelectronics* **2005**, *21*, 719–726.

[168] L. Zhu, Y. Gao, H. Shen, Y. Yang, L. Yuan, *Journal of Analytical Chemistry* **2005**, *60*, 780–783.

[169] R.-Z. Hao, H.-B. Song, G.-M. Zuo, R.-F. Yang, H.-P. Wei, D.-B. Wang, Z.-Q. Cui, Z. Zhang, Z.-X. Cheng, X.-E. Zhang, *Biosensors and Bioelectronics* **2011**, *26*, 3398–3404.

[170] N. N. Maslakci, F. D. Danas, A. U. Oksuz, *Journal of Macromolecular Science Part A* **2016**, *53*, 311–316.

[171] K. E. Dunn, M. A. Trefzer, S. Johnson, A. M. Tyrrell in *DNA Nanotechnology: Methods and Protocols*, (Ed.: G. Zuccheri), Springer New York, New York, NY, **2018**, pp. 101–114.

[172] D. Y. Petrovykh, H. Kimura-Suda, M. J. Tarlov, L. J. Whitman, *Langmuir* **2004**, *20*, 429–440.

[173] A. Opdahl, D. Y. Petrovykh, H. Kimura-Suda, M. J. Tarlov, L. J. Whitman, *Proceedings of the National Academy of Sciences* **2007**, *104*, 9–14.

[174] M. R. Vilar, A. M. Botelho do Rego, A. M. Ferraria, Y. Jugnet, C. Noguès, D. Peled, R. Naaman, *The Journal of Physical Chemistry B* **2008**, *112*, 6957–6964.

[175] S. A. J. van der Meulen, G. V. Dubacheva, M. Dogterom, R. P. Richter, M. E. Leunissen, *Langmuir* **2014**, *30*, 6525–6533.

[176] A. Steel, R. Levicky, T. Herne, M. Tarlov, *Biophysical Journal* **2000**, *79*, 975–981.

[177] Z. Li, L. Zhang, S. Zeng, M. Zhang, E. Du, B. Li, *Journal of Electroanalytical Chemistry* **2014**, *722-723*, 131–140.

[178] M. N. Khan, M. Zharnikov, *The Journal of Physical Chemistry C* **2014**, *118*, 3093–3101.

[179] Z. Li, T. Niu, Z. Zhang, R. Chen, G. Feng, S. Bi, *Biosensors and Bioelectronics* **2011**, *26*, 4564–4570.

[180] D. Rekesh, Y. Lyubchenko, L. Shlyakhtenko, S. Lindsay, *Biophysical Journal* **1996**, *71*, 1079–1086.

[181] L. Martínez, L. G. Carrascosa, Y. Huttel, L. M. Lechuga, E. Román, *Physical Chemistry Chemical Physics* **2010**, *12*, 3301.

[182] K. B. Rodenhausen, T. Kasputis, A. K. Pannier, J. Y. Gerasimov, R. Y. Lai, M. Solinsky, T. E. Tiwald, H. Wang, A. Sarkar, T. Hofmann, N. Ianno, M. Schubert, *Review of Scientific Instruments* **2011**, *82*, 103111.

[183] L. G. Carrascosa, L. Martínez, Y. Huttel, E. Román, L. M. Lechuga, *European Biophysics Journal* **2010**, *39*, 1433–1444.

[184] E. L. S. Wong, E. Chow, J. J. Gooding, *Langmuir* **2005**, *21*, 6957–6965.

[185] P. Capaldo, S. R. Alfarano, L. Ianeselli, S. D. Zilio, A. Bosco, P. Parisse, L. Casalis, *ACS Sensors* **2016**, *1*, 1003–1010.

[186] P. Parisse, I. Solano, M. Magnozzi, F. Bisio, L. Casalis, O. Cavalleri, M. Canepa in *Ellipsometry of Functional Organic Surfaces and Films*, *Vol. 52*, (Eds.: K. Hinrichs, K.-J. Eichhorn), Springer International Publishing, Cham, **2018**, pp. 63–93.

[187] M. Canepa, G. Maidecchi, C. Toccafondi, O. Cavalleri, M. Prato, V. Chaudhari, V. A. Esaulov, *Physical Chemistry Chemical Physics* **2013**, *15*, 11559–11565.

[188] H. Hamoudi, M. Prato, C. Dablemont, O. Cavalleri, M. Canepa, V. A. Esaulov, *Langmuir* **2010**, *26*, 7242–7247.

[189] D. R. T. Zahn, S. D. Silaghi in *Advances in Solid State Physics*, *Vol. 45*, (Ed.: B. Kramer), Springer-Verlag, Berlin/Heidelberg, **2005**, pp. 45–57.

[190] J. Nizioł, K. Makyła-Juzak, M. M. Marzec, R. Ekiert, M. Marzec, E. Gondek, *Optical Materials* **2017**, *66*, 344–350.

[191] B. Paulson, I. Shin, H. Jeong, B. Kong, R. Khazaeinezhad, S. R. Dugasani, W. Jung, B. Joo, H.-Y. Lee, S. Park, K. Oh, *Scientific Reports* **2018**, *8*, 9358.

[192] A. Ito, T. Ito, *Photochemistry and Photobiology* **1986**, *44*, 355–358.

[193] P.-J. Chou, W. C. Johnson, *Journal of the American Chemical Society* **1993**, *115*, 1205–1214.

[194] S. Elhadj, G. Singh, R. F. Saraf, *Langmuir* **2004**, *20*, 5539–5543.

[195] S. Wenmackers, S. D. Pop, K. Roodenko, V. Vermeeren, O. A. Williams, M. Daenen, O. Douhéret, J. D'Haen, A. Hardy, M. K. Van Bael, K. Hinrichs, C. Cobet, M. vandeVen, M. Ameloot, K. Haenen, L. Michiels, N. Esser, P. Wagner, *Langmuir* **2008**, *24*, 7269–7277.

[196] G. Felsenfeld, S. Z. Hirschman, *Journal of Molecular Biology* **1965**, *13*, 407–427.

[197] S. N. Volkov, *International Journal of Quantum Chemistry* **1979**, *16*, 119–132.

[198] R. Thomas, *Gene* **1993**, *135*, 77–79.

[199] J. J. Nogueira, F. Plasser, L. González, *Chem. Sci.* **2017**, *8*, 5682–5691.

[200] H. Sun, S. Zhang, C. Zhong, Z. Sun, *Journal of Computational Chemistry* **2016**, *37*, 684–693.

[201] M. D'Abramo, C. L. Castellazzi, M. Orozco, A. Amadei, *The Journal of Physical Chemistry B* **2013**, *117*, 8697–8704.

[202] C.-Y. Lee, P. Gong, G. M. Harbers, D. W. Grainger, D. G. Castner, L. J. Gamble, *Analytical Chemistry* **2006**, *78*, 3316–3325.

[203] C. Howell, J. Zhao, P. Koelsch, M. Zharnikov, *Physical Chemistry Chemical Physics* **2011**, *13*, 15512–15522.

[204] A. V. Saprigin, C. W. Thomas, C. S. Dulcey, C. H. Patterson, M. S. Spector, *Surface and Interface Analysis* **2005**, *37*, 24–32.

[205] R. G. Nuzzo, B. R. Zegarski, L. H. Dubois, *Journal of the American Chemical Society* **1987**, *109*, 733–740.

[206] D. G. Castner, K. Hinds, D. W. Grainger, *Langmuir* **1996**, *12*, 5083–5086.

[207] C. Vericat, M. E. Vela, G. Andreasen, R. C. Salvarezza, L. Vázquez, J. A. Martín-Gago, *Langmuir* **2001**, *17*, 4919–4924.

[208] M. Zharnikov, M. Grunze, *Journal of Physics: Condensed Matter* **2001**, *13*, 11333–11365.

[209] O. Cavalleri, M. Vignolo, G. Strano, C. Natale, R. Rolandi, S. Thea, M. Prato, G. Gonella, M. Canepa, A. Gliozzi, *Bioelectrochemistry* **2004**, *63*, 3–7.

[210] G. Gonella, S. Terreni, D. Cvetko, A. Cossaro, L. Mattera, O. Cavalleri, R. Rolandi, A. Morgante, L. Floreano, M. Canepa, *The Journal of Physical Chemistry B* **2005**, *109*, 18003–18009.

[211] L. Pasquali, F. Terzi, R. Seeber, S. Nannarone, D. Datta, C. Dablemont, H. Hamoudi, M. Canepa, V. A. Esaulov, *Langmuir* **2011**, *27*, 4713–4720.

[212] J. Jia, A. Kara, L. Pasquali, A. Bendounan, F. Sirotti, V. A. Esaulov, *The Journal of Chemical Physics* **2015**, *143*, 104702.

[213] Y. W. Yang, L. J. Fan, *Langmuir* **2002**, *18*, 1157–1164.

[214] A. Kick, M. Bönsch, K. Kummer, D. V. Vyalikh, S. L. Molodtsov, M. Mertig, *Journal of Electron Spectroscopy and Related Phenomena* **2009**, *172*, 36–41.

[215] D. Grumelli, L. J. Cristina, F. L. Maza, P. Carro, J. Ferrón, K. Kern, R. C. Salvarezza, *The Journal of Physical Chemistry C* **2015**, *119*, 14248–14254.

[216] C. Vericat, M. E. Vela, G. Benitez, P. Carro, S. Salvarezza, R. C., *Chemical Society Reviews* **2010**, *39*, 1805.

[217] C. Vericat, M. E. Vela, G. Corthey, E. Pensa, E. Cortés, M. H. Fonticelli, F. Ibañez, G. E. Benitez, P. Carro, R. C. Salvarezza, *RSC Adv.* **2014**, *4*, 27730–27754.

[218] M. Zharnikov, *Journal of Electron Spectroscopy and Related Phenomena* **2010**, *178-179*, 380–393.

[219] E. E. Charrier, K. Pogoda, R. G. Wells, P. A. Janmey, *Nature Communications* **2018**, *9*, 449.

[220] W. Kaiser, U. Rant, *Journal of the American Chemical Society* **2010**, *132*, 7935–7945.

[221] P. S. Gil, D. J. Lacks, P. Parisse, L. Casalis, M. D. Nkoua Ngavouka, *Soft Matter* **2018**, *14*, 9675–9680.

[222] D. E. Gray, S. C. Case-Green, T. S. Fell, P. J. Dobson, E. M. Southern, *Langmuir* **1997**, *13*, 2833–2842.

[223] G. Legay, L. Markey, R. Meunier-Prest, E. Finot, *Ultramicroscopy* **2007**, *107*, 1111–1117.

[224] A. Samoc, A. Miniewicz, M. Samoc, J. G. Grote, *Journal of Applied Polymer Science* **2007**, *105*, 236–245.

[225] J. Shi, B. Hong, A. Parikh, R. Collins, D. Allara, *Chemical Physics Letters* **1995**, *246*, 90–94.

[226] E. Mirmomtaz, M. Castronovo, C. Grunwald, F. Bano, D. Scaini, A. A. Ensafi, G. Scoles, L. Casalis, *Nano Letters* **2008**, *8*, 4134–4139.

[227] D. H. Kim, J. Noh, M. Hara, H. Lee, **2001**, 5.

[228] Z. Li, T. Niu, Z. Zhang, R. Chen, G. Feng, S. Bi, *Analyst* **2011**, 10.

Acknowledgements

My warmest thanks to Prof. Ornella Cavalleri, who assisted and guided me through every stage of my research project. I am deeply grateful for her unwavering support, her essential tips, and her trust in me.
My profound gratitude goes to Prof. Maurizio Canepa for supporting me and offering a deep insight into the research, and whose valuable advice was never lacking during my path.
I would like to offer my special thanks to Dr. Silvia Dante for the helpfulness and kindness with which she supported me during the QCM-D experiments carried out at the Morego site of the Italian Institute of Technology. I wish to extend my thanks to Dr. Mirko Prato for giving me this great opportunity.
I would like to express my sincere gratitude to Dr. Francesco Bisio and Dr. Paolo Canepa for their crucial support on the experimental work and their insightful comments and suggestions.
I would like to express my gratitude to Dr. Pietro Parisse (IOM-CNR Trieste) and Dr. Loredana Casalis (Elettra Sincrotrone S.p.a., Trieste) for the interesting discussions and the support on the nanoshaving and nanografting techniques.
I wish to show my appreciation to Prof. Flavio Gatti for allowing me to use the UHV evaporation chamber for gold to fabricate Ulman-type substrates.
Finally, I would like to thank the Biophysics group for the stimulating and collaborative environment.